Summer 2019

Liquid Phase Modeling in Heterogeneous Catalysis

Mohammad Shamsus Saleheen

LIQUID PHASE MODELING IN HETEROGENEOUS CATALYSIS

by

Mohammad Shamsus Saleheen

Bachelor of Science
Bangladesh University of Engineering and Technology, 2012

Submitted in Partial Fulfillment of the Requirements

For the Degree of Doctor of Philosophy in

Chemical Engineering

College of Engineering and Computing

University of South Carolina

2019

Accepted by:

Andreas Heyden, Major Professor

Donna A. Chen, Committee Member

John R. Regalbuto, Committee Member

John W. Weidner, Committee Member

Mark J. Uline, Committee Member

Salai C. Ammal, Committee Member

Cheryl L. Addy, Vice Provost and Dean of the Graduate School

DEDICATION

To my wife, Nijhum.

“In the vastness of space and the immensity of time, it is my joy to share a planet and an epoch with you.”

ACKNOWLEDGEMENTS

There are no appropriate words to convey my deep appreciation and respect for my advisor Dr. Andreas Heyden. The joy and enthusiasm he has for research was contagious, stimulating, and inspirational for me, even during the tough times of my PhD. If I can become half the thinker and half the researcher that Dr. Heyden is, I will be proud of my life.

I would like to thank my committee members, Dr. Ammal, Dr. Chen, Dr. Regalbuto, Dr. Uline, and Dr. Weidner for their guidance, time, and help. I must give special recognition to Dr. Salai Ammal, Dr. Osman Mamun, and Mehdi Zare, who contributed to my thesis with their knowledge, work, and constructive criticism. I am thankful to all the Heyden Lab group members, Dr. Sina Behtash, Dr. Jianmin Lu, Dr. Eric Walker, Dr. Yongjie Xi, Dr. Biplab Rajbanshi, Charles Fricke, Kyung-Eun You, Subrata Kundu, Wenqiang Yang, Dia Sahsah, and Nicholas Szaro for being great coworkers and friends.

I am grateful to the Chemical Engineering Department staffs, Marcia Rowen, Loretta Hardcastle, Vernon Dorrell, Brian Loggans, and Shawn Hagan for assisting me with administrative and technical issues.

Finally, I would like to thank my family for their unconditional love and encouragement. This is for my parents who raised me with a love of science and supported me in all my endeavors.

ABSTRACT

Conversion of lignocellulosic biomass into transportation fuels or commodity and specialty chemicals will be an important and fast-growing industry within the United States over the coming decades. Its growth will be driven by a variety of factors, including increased energy demands, environmental considerations, national security, and government mandates. To achieve the desired energy efficiency and economic impact, the emerging biorefining industries need novel heterogeneous catalysts with exceptional activity, selectivity, and stability. Catalytic materials developed in the petrochemical industries are generally not suitable for processing highly functionalized feedstocks typical of the biorefinery landscape. Due to the characteristics of this biomass feedstock (aqueous, highly water soluble, very reactive, and thermally unstable), liquid-phase processing technologies are exceedingly sought after to reduce the process cost as well as to increase the targeted product selectivity. Despite making considerable progress in our understanding of the stability and the surface properties of metal-supported nanoparticles in vapor phase environments, the effect of condensed phase is less investigated and not well-understood due to the added complexity of the reaction system containing both a complex heterogeneous catalyst and a condensed phase.

In order to gain fundamental understanding of the solvation phenomena occurring at solid-liquid interfaces, our research is primarily focused on the development, validation, and application of solvation methods for the rational design of novel

heterogeneous transition metal catalysts for biomass conversion processes. As prototypical reactions with relevance to biomass catalysis, we investigated the hydrodeoxygenation (HDO) of various model biomolecules such as ethanol, ethylene glycol, and guaiacol under vapor and aqueous phase processing conditions to elucidate the reaction mechanism and the effect of condensed phase on the reaction kinetics. Using first principles calculations, continuum solvation models, and mean-field microkinetic modeling, we characterized the solvent effects on the kinetics of reactions and product distributions. An important outcome of our study is the identification of uncertainty in computed solvent effects due to the uncertainty of the cavity radius of transition metal atoms in implicit solvation schemes. To further elucidate the role of water on the reaction mechanism, we performed solvation calculations with our explicit solvation scheme for metal surfaces (eSMS). We found that implicit solvation models are most appropriate whenever directional hydrogen bonding is not present or does not change significantly along the reaction coordinate. Explicit solvation calculations agree with the implicit solvation models for C-H and C-OH bond cleavages of polyols where they both predict a small (<0.10 eV) solvent effect. In contrast and unlike the implicit solvation models, our explicit solvation model predicts a larger solvent stabilization (>0.35 eV) for the O-H bond cleavage due to its ability to approximately describe hydrogen bonding. Consequently, O-H bond dissociations are significantly favored over C-H and C-OH bond dissociations of polyols under aqueous processing conditions of biomass.

TABLE OF CONTENTS

Dedication iii

Acknowledgements iv

Abstract v

List of Tables ix

List of Figures xi

Chapter 1: Introduction……..……1

Chapter 2: Liquid Phase Modeling in Heterogeneous Catalysis 6

2.1 Acknowledgements 22

2.2 Tables and Figures 23

2.3 Bibliography 28

Chapter 3: Computational Investigation of Aqueous-Phase Effects on The Dehydrogenation and Dehydroxylation of Polyols Over Pt(111) 32

3.1 Abstract 33

3.2 Introduction 34

3.3 Computational Details 39

3.4 Results and Discussion 44

3.5 Conclusion 56

3.6 Acknowledgements 57

3.7 Tables and Figures 58

3.8 Bibliography 68

Chapter 4: Investigation of Solvent Effects on the Hydrodeoxygenation of Guaiacol Over Ru Catalyst 77

4.1 Abstract 78

4.2 Introduction 79

4.3 Computational Approach 83

4.4 Model Development 87

4.5 Results and Discussion 91

4.6 Conclusion 112

4.7 Acknowledgements 113

4.8 Tables and Figures 114

4.9 Bibliography 128

Appendix A: Supporting Information for Liquid Phase Modeling in Heterogeneous Catalysis 135

Appendix B: Supporting Information for Computational Investigation of Aqueous-Phase Effects on The Dehydrogenation and Dehydroxylation of Polyols Over Pt(111) 143

Appendix C: Supporting Information for Investigation of Solvent Effects on the Hydrodeoxygenation of Guaiacol Over Ru Catalyst 154

Appendix D: Copyright Permissions 159

LIST OF TABLES

Table 2.1 Aqueous phase effects on the free energy of reaction, free energy of activation, heat of reaction, and entropic contributions for O-H and C-H model reactions at 500 K on Pt(111) using implicit and explicit solvation models. Vapor phase PBE calculations predicted at 500 K for C-H bond cleavage: $\Delta H_{rxn} = -0.48\ eV$, $\Delta G_{rxn} = -0.40\ eV$, $\Delta G^{\dagger} = +0.73\ eV$ and for O-H bond cleavage: $\Delta H_{rxn} = +0.38\ eV$, $\Delta G_{rxn} = +0.45\ eV$, $\Delta G^{\dagger} = +0.70\ eV$. 23

Table 3.1 Aqueous phase effects on the free energy of reaction and the free energy of activation of model reactions of ethylene glycol over Pt(111) at 500 K. QM/MM-FEP calculations describe the solvent effect on the critical points identified by gas-phase calculations while using the gas-phase vibrational partition function for the adsorbed species and transition states. The superscript SH and LJ (SH = Spohr-Heinzinger, LJ = Metal Lennard-Jones) denotes the potential used to describe the metal-water interaction. QM/MM-FEP(OPT) represents the solvent effects for the model reactions (using SH potential) where the respective reactant, transition, and product states have all been optimized in an aqueous-phase environment and the vibrational frequencies are computed in the liquid phase assuming the timescale for re-orientation of solvent molecules is much larger than the timescale for molecular vibrations. Implicit solvation calculations have been performed using both non-periodic (iSMS) and periodic (VASPsol) approaches.....58

Table 4.1 Solvent effects on the adsorption strength of various surface intermediates in the HDO of Guaiacol over Ru(0001) model surface at 473 K temperature.....114

Table 4.2 Energetics of adsorption-desorption reactions (in eV) for HDO of guaiacol in the limit of zero coverage at 473 K temperature under different reaction environments. 115

Table 4.3 Energetics of all elementary surface reaction steps (in eV) for HDO of guaiacol to unsaturated aromatics in the limit of zero coverage at 473 K temperature in the presence of liquid water, 1-butanol, diethyl ether, and n-hexane solvents…….....116

Table 4.4 Computed overall turnover frequencies at various reaction temperatures and 15 bar partial pressure of hydrogen for HDO of guaiacol over Ru(0001) surface. Microkinetic models have been simulated for 1% conversion of guaiacol using 0.5 g guaiacol in 10 g of different solvent medium. 118

Table 4.5 Coverages (%) of most abundant surface intermediates in various reaction environments for HDO of guaiacol at 473K temperature. 119

Table 4.6 Kinetic parameters computed at 473 K for HDO of guaiacol over Ru(0001) model surface at low conversion conditions under various reaction environments. 119

Table 4.7 Thermodynamic and kinetic sensitivity analysis at 473 K for HDO of guaiacol over Ru(0001) model surface 120

Table 4.8 Energetics of important elementary surface reaction steps (in eV) in the limit of zero coverage at 473 K temperature in the presence of liquid water, 1-butanol, diethyl ether, and n-hexane solvents for phenol hydrogenation to cyclohexanol.....121

LIST OF FIGURES

Figure 2.1 Effect of cavity radius of Ru (±10% of the Turbomole value of 2.223 Å) on the water solvation free energy of an adsorbed OH group (HCP) on Ru(0001) at 298 and 423 K. Plotted is the difference in the adsorption free energy of OH in the presence of liquid water (OH(g) + ∗(l) ↔ OH∗(l)) and absence of any aqueous solvent (OH(g) + ∗(g) ↔ OH∗(g)) 24

Figure 2.2 Free energy profile for O-H bond cleavage of ethylene glycol in vapor and aqueous phases over a Pt(111) model surface at 500 K (without considering vibrational contributions of the adsorbed ethylene glycol species to the partition function). The aqueous phase profile has been plotted for a single QM/MM calculation using Bennett Acceptance Ratio (BAR) as the free energy estimator among the 10 QM/MM calculations performed. The transition state appears to have a lower energy compared to adjacent images because the intermediate images introduced along the approximate reaction coordinate were not optimized to the minimum free energy path 25

Figure 2.3 Temperature dependence of aqueous solvation effect on the free energy reaction for the primary O-H bond scission of ethylene glycol over a Pt(111) model surface. The error bars indicate 95% confidence interval for the aqueous phase effect on the free energy of the specified reaction 26

Figure 2.4 Free energy profile for C-H bond cleavage of ethylene glycol in vapor and aqueous phases over a Pt(111) model surface at 500 K (without considering vibrational contributions to the partition function). The aqueous phase profile has been drawn for a single QM/MM calculation using Bennett Acceptance Ratio (BAR) as the free energy estimator among the 10 QM/MM calculations performed 27

Figure 3.1 95% confidence interval estimates of (a) free energy of reaction and the (b) free energy of activation of the O-H bond cleavage of ethylene glycol over a Pt(111) surface at 500 K. Total QM/MM energies have been computed by employing three distinct equilibration times of 50 ps, 100 ps, and 250 ps 60

Figure 3.2 Effect of phase space sampling time on the estimation of (a) free energy of reaction and (b) free energy of activation of the model O-H bond scission reaction of ethylene glycol on a Pt(111) surface at 500 K. The error bars represent the 95% confidence interval estimate of the free energy of the specified reaction 61

Figure 3.3 System size effect on (a) free energy of reaction and (b) free energy of activation of the prototypical O-H bond cleavage reaction of ethylene glycol on a Pt(111) model surface at 500K. The error bars represent the 95% confidence interval estimate of the free energy of the specified reaction.....62

Figure 3.4 Free energy profile for the O-H bond cleavage of ethylene glycol in vapor and aqueous phases on a Pt(111) model surface at 500 K without considering vibrational contributions to the partition function. See Table 1 for corresponding data that include vibrational contributions. The points lying on the vertical dashed lines represent the geometries optimized in vapor phase while the magenta dots on the QM/MM-FEP(Optimized) profile represent the aqueous phase optimized structures of the reactant state, transition state, and product state for the O-H bond cleavage. The aqueous phase profiles portray the average of 3 QM/MM-FEP calculations that possess 95% confidence intervals smaller than ±0.1 eV.....63

Figure 3.5 Free energy profile for the C-H bond cleavage of ethylene glycol in vapor and aqueous phases on a Pt(111) model surface at 500 K without considering vibrational contributions to the partition function. See Table 1 for corresponding data that include vibrational contributions. The points lying on the vertical dashed lines represent the geometries optimized in vapor phase while the magenta dots on the QM/MM-FEP(Optimized) profile represent the aqueous phase optimized structures of the reactant state, transition state, and product state for the C-H bond cleavage. The aqueous phase profiles are the average of 3 QM/MM-FEP calculations that possess 95% confidence intervals smaller than ±0.1 eV.....64

Figure 3.6 Free energy profile for the C-OH bond cleavage of ethylene glycol in vapor and aqueous phases on a Pt(111) model surface at 500 K without considering vibrational contributions to the partition function. See Table 1 for corresponding data that include vibrational contributions. The points lying on the vertical dashed lines represent the geometries optimized in vapor phase while the magenta dots on the QM/MM-FEP(Optimized) profile represent the aqueous phase optimized structures of the reactant state, transition state, and product state for the C-OH bond cleavage. The aqueous phase profiles are the average of 3 QM/MM-FEP calculations that possess 95% confidence intervals smaller than ±0.1 eV.....65

Figure 3.7 Effect of aqueous phase on the free energy of reaction and activation of a) O-H, b) C-H, and c) C-OH bond cleavages of ethylene glycol over Pt(111) using different implicit and explicit solvation models. Error bars for the explicit solvation models are 95% confidence intervals.....67

Figure 4.1 Reaction network investigated for the hydrodeoxygenation of guaiacol over Ru(0001) model surface. Duplicate structures are highlighted by identical background colors 122

Figure 4.2 Turnover frequencies (1/s) along the dominant reaction pathway for HDO of guaiacol to unsaturated aromatic products over Ru(0001) surface computed in different reaction environments 123

Figure 4.3 Turnover frequencies (1/s) along the dominant reaction pathway for HDO of guaiacol to unsaturated aromatic products over Ru(0001) surface in vapor and aqueous phases. Aqueous phase calculations have been performed using three different cavity radius of Ru atoms 124

Figure 4.4 Reaction network investigated along the C_1 and C_2 hydrogenation pathway of phenol over Ru(0001) model surface. Duplicate structures have been highlighted by identical border colors 125

Figure 4.5 Reaction network investigated along the C_3 and C_4 hydrogenation pathway of phenol over Ru(0001) model surface. Duplicate structures have been highlighted by identical border colors 126

Figure 4.6 Reaction network investigated along the keto-enol tautomerization pathway of phenol over Ru(0001) model surface. Duplicate structures have been highlighted by identical border colors. Proposed reaction mechanism and the reaction steps involved for cycloalkane production from phenol have also been highlighted 127

CHAPTER 1

INTRODUCTION

The ability to include the effect of a liquid phase environment on chemical reactions occurring at solid-liquid interfaces is a distinctive challenge in computational catalysis. Liquid molecules can affect the stability of an adsorbed moiety and can provide low energy pathways for reactions, which affects the activity and selectivity of a catalyst. Reaction free energies and free energy barriers of elementary reactions occurring at solid-liquid interfaces can be very different for the same processes occurring at solid-gas interfaces. Describing such a system quantum mechanically from first principles is computationally very expensive due to limited computational resources, where the system size is limited to hundreds of atoms, while simulating an aqueous phase often requires thousands of molecules to be included in the system. The objective of my research is to gain a better understanding of the chemistry at solid-liquid interfaces using both continuum solvation and hybrid QM/MM solvation approaches.

This dissertation has been written following the manuscript style formatting, meaning each chapter of this dissertation is an independent scientific publication. In chapter 2, we examined some of the prevailing approaches for modeling condensed phases in heterogeneous catalysis and applied our own hybrid QM/MM model, called eSMS, to the C-H and O-H bond cleavage of ethylene glycol over Pt(111) model surface under aqueous phase processing conditions. This article has recently (January 2018) been

published in ACS Catalysis as a full-length viewpoint scientific article. All atom quantum chemical (DFT) methods and classical force field simulations are currently not the most practical approaches for describing solvent effects in heterogeneous catalysis due to the large computational expense and limited/unknown accuracy, respectively. Microsolvation and bilayer adsorption/ice models are most appropriate whenever the system temperature is low enough or the solvent-solute interaction strong enough that entropic effects along the reaction coordinate can be described accurately by the harmonic approximation. There is a risk that due to a lack of extensive configuration space sampling, these models significantly overestimate solvent effects whenever the harmonic approximation breaks down. Likely, these models are more appropriate for predicting enthalpies of solvation than free energies of solvation. In agreement with prior reports, we found that enthalpies of solvation are generally larger than free energies of solvation (roughly twice as large although the overestimation is temperature and system dependent). Next, the implicit or continuum solvation models are the easiest models to apply that can convey qualitative results for the computation of solvent effects. They are most appropriate whenever directional hydrogen bonding is not present or does not change significantly along a reaction coordinate. We found these models to underestimate strong hydrogen bonding effects. Also, the parameterization for transition metal element dependent parameters needs a more thorough validation. Finally, we deem QM/MM models to be currently the most appropriate models for predicting solvation effects in heterogeneous catalysis with an adequate balance between computational expense and chemical accuracy in regard to potential energy surface description and configuration space sampling. In this manuscript, we reviewed such a hybrid QM/MM model, called eSMS, and applied it to C-H and O-H

bond cleavage of ethylene glycol on Pt(111) under aqueous phase reforming conditions to explain the counter-intuitive (and likely wrong) result of implicit solvation models that predict hardly any aqueous solvent effect in O-H bond cleavage.

In my second publication (chapter 3, recently submitted to Journal of Physical Chemistry C), using the O-H splitting reaction of ethylene glycol over Pt(111) as a case study and characteristic reaction for various biomass platform molecule conversion reactions over noble metal catalysts, we studied the required timescale to reach thermal equilibrium, the sampling time scale necessary to explore the configuration space, and the size of the simulation system for obtaining reliable and converged free energies of activation and reaction with our eSMS methodology for studying solvation effects in heterogeneous catalysis. Due to the difficulty in determining the correlation time in free energy calculations, we recommend that all explicit solvation calculations be repeated multiple times just as it is common for experiments. Only by repeating simulations at least three times can confidence intervals (resulting from insufficient configuration space sampling and intricacies from our QM/MM-FEP methodology) be estimated. Assuming our test reactions are characteristic for various reactions on metal surfaces, our heuristic recommendations lead to free energies with 95% confidence intervals of < 0.1 eV. After establishing protocols for calculating solvent effects using multiscale models, we calculated solvent effects on the free energy of reaction and free energy of activation for primary dehydrogenation and dehydroxylation reactions of ethylene glycol at the hydroxyl group and α-C. Our explicit solvation model predicts that aqueous phase effects are small (< 0.1 eV) for the C-H bond cleavage and the activation barrier of the C-OH bond cleavage. In contrast, solvation effects are large (> 0.35 eV) for the O-H bond

cleavage and the reaction free energy of the C-OH bond scission. While the choice of a different Pt-water force field can lead to differences in predicted solvation effects of up to 0.2 eV, the differences are usually much smaller (< 0.1 eV) and the trends are always the same. In contrast, implicit solvation models only qualitatively agree with the explicit solvation results for the C-H bond cleavage and they are unable to anticipate the hydrogen bonding stabilization for the O-H and even the C-OH cleavage reactions.

In chapter 4 (third publication), we extended our previously reported in-depth vapor phase modeling of HDO of guaiacol over Ru(0001) model surface to the liquid phase and examined the solvent influence on the reaction mechanism and possible activity descriptors for HDO of guaiacol over Ru(0001) model surface. Several studies conducted at relatively mild reaction conditions have reported the presence of aromatic ring saturated products which was not considered in our previous study. In this study, we extended our calculations to investigate the formation of phenyl ring saturated products in vapor phase and condensed phases. While electrostatic interactions and hydrogen bonding contributions are instrumental for the interaction between a polar adsorbate and a polar solvent, london dispersion forces play a crucial part for non-polar adsorbate-solvent systems. To consider both of these scenarios, four different solvents of varying degree of polarity (depending on Kamlet and Taft's solvatochromic parameters) have been employed for this study. Specifically, we focused on the effects of liquid water which is a polar, protic solvent, 1-butanol, a polar aprotic solvent, diethyl ether, a 'borderline' polar aprotic solvent, and a non-polar solvent, n-hexane. Using first principles calculations and a novel implicit solvation scheme for solid surfaces (iSMS), we characterized the solvent effects on the thermodynamics and kinetics of elementary reactions. A mean field

microkinetic reactor model was then developed to reexamine the most abundant surface intermediates, dominant reaction pathways, and general kinetic trends in condensed phases. Our model predicted that for HDO of guaiacol to aromatics production, less protic solvents have a positive effect on the reaction kinetics compared to vapor and aqueous phases. We also observed that aqueous phase has a more favorable effect for cycloalkane production from phenol compared to that of vapor phase and other less protic solvents.

CHAPTER 2

LIQUID PHASE MODELING IN HETEROGENEOUS CATALYSIS

Saleheen, M.; Heyden, A. *ACS Catalysis,*

2018, 8 (3), 2188-2194.

The notion that solvents can affect the chemical reactivity has been prevalent in the homogeneous catalysis community, going back as far as 1863.[1] Remarkable changes in reaction rate have been reported in the seminal work of Menschutkin, who demonstrated a change in reaction rate constant up to a factor of 700 as a function of the solvents employed for the reaction of triethylamine with ethyl iodide at 373 K.[2] It is well known nowadays that solvents can affect the reaction rate, reaction mechanism, and selectivity of chemical reactions occurring in condensed phase. While solvent effects usually lead to changes in reaction rates of up to three orders of magnitude, rate increases of nine orders of magnitude have been reported.[3-4] In homogeneous metal catalysis such as hydroformylation, hydrogenation, and cross-coupling reactions, solvent effects have been studied systematically and exploited for industrial applications.[5] Substantial solvent effects have also been reported in heterogeneous catalysis for several hydrogenation,[6-9] oxidation,[10-12] and electro-chemical reactions (where electric field effects lead in addition to an electric double layer[13-16]). However, in heterogeneous catalysis, systematic studies of solvation effects are rare and solvent effects are generally not well understood. In this context, we note that liquid phase processing is highly desirable for process cost reduction and high product selectivity for the heterogeneously catalyzed conversion of highly functionalized lignocellulosic biomass, since the feedstocks contain significant amounts of water, are produced in aqueous phase environments, and reactant molecules are highly water soluble, reactive, and thermally unstable.[17-19] Processing at relatively low temperatures in condensed phase has therefore the potential to (1) minimize undesirable thermal degradation reactions, (2) increase the targeted product selectivity,

and (3) facilitate the product separation from excess water since reaction products often contain less oxygen and are therefore less hydrophilic than the feed streams.

Computational catalysis has in the last 20 years become an increasingly important tool for understanding catalytic reactions and designing new catalytic materials of industrial relevance.[20-22] However, progress has been limited to vapor-phase catalysis and theoretical studies[8,11,23-24] of solvent effects in heterogeneous catalysis are still in their infancies. The relative lack of progress in computational catalysis at solid-liquid interfaces can be explained by the added complexity of a reaction system containing both a complex heterogeneous catalyst and a condensed phase and by fundamental modeling challenges of systems for which the harmonic approximation[25] for estimating partition functions and free energies is no longer valid. The later challenge is a long-standing issue in the molecular simulations community for systems that require extensive configuration space sampling on a high dimensional potential energy surface that cannot be described by simple, empirical potentials but requires a quantum chemical description as it is generally the case for transition metal catalysis. It should be highlighted that due to the typical correlation lengths (on the order of nanometers[26]) and correlation times in most liquids (on the order of picoseconds for water reorientation[27]), all-atomistic free energy computations of processes at solid-liquid interfaces require a simulation system containing a few hundred if not a few thousand liquid molecules sampled for at least a few hundred (or thousand) picoseconds. Accordingly, on the order of 10^6 times more energy evaluations are needed for estimating free energy changes in liquid phase for a system containing at least one order of magnitude more atoms than what is typical for heterogeneous vapor phase catalysis. Thus, brute force *ab initio* molecular dynamics

(AIMD) simulations[28-30] are prohibitively expensive and most likely not practical for the foreseeable future (although some very interesting results have been reported[11-12,31]).

This brings us to the key issue: Can we come up with an alternative, computationally affordable and reliable method for computing free energy changes (and rates within transition state theory) for chemically activated processes occurring at solid-liquid interfaces? In this contribution, we aim to (1) examine some of the prevailing approaches to model condensed phases and discuss the potential advantages and pitfalls associated with these. Then, (2) we describe our hybrid quantum mechanical and molecular mechanical (QM/MM) approach to resolve the well-established challenge of reducing the computational expense all the while keeping a robust chemical accuracy of the reaction system. Finally, (3) we employ our computational approach for the initial O-H and C-H bond cleavages of ethylene glycol (EG) over Pt(111) under aqueous phase processing conditions and contrast our explicit solvation model with implicit solvation in regards to their ability to describe hydrogen bonding and entropic contributions for free energy computations.

Conceptually, there are five different approaches to accelerate the computation of solvation effects on reaction and activation free energies at solid-liquid interfaces.

Bilayer adsorption/ice model. A buckled hexagonally closed-packed network of water molecules resembling the (001) basal plane of ice was proposed by Doering and Madey[32] and was primarily developed based on low temperature ($T \ll 273\ K$) experiments on interfacial water over metal (Ru) surfaces. Considering the solid-like behavior of the ice-film, classical (gas phase) partition functions can be used for free

energy estimations requiring a very limited configuration space sampling. However, little is known on how an adsorbed species like a sugar molecule perturbs the ice structure.[33] Different types of ice-structures can form[34] on non-extended surfaces (e.g., a nanoparticle) or stepped surfaces that stabilize or destabilize an adsorbed species differently. Thus, we consider it unlikely that under practical biomass conversion conditions in a three-phase reactor, ice-like structures can form on a catalyst surface considering that Natarajan and Behler[27] did not observe such structures on solid-liquid interfaces of Cu surfaces at 300 K.

Implicit solvation model. Another approach that circumvents the difficulties associated with phase space sampling is to use isotropic continuum solvation models (CSM), where the solvent is represented as a homogenous constant dielectric continuum surrounding the solute. In this way, implicit solvent models consider thermally averaged solvent molecules which leads to a model with only a small number of parameters used to represent the solvent with reasonable accuracy in most situations. CSM based models are first principle methods which have the advantage of having a computational expense similar to gas-phase models with a wide range of applicability.[35-39] A key limitation of this approach is the inability or approximate approach for describing the site-specific interactions between the solute and the solvents, e.g., hydrogen bonding. Also, the parameterization of transition metal element specific parameters in the solvent models remains a challenge due to a lack of reliable experimental data (for main group elements implicit solvation models are highly accurate and predictive results can be obtained), e.g., there is a large uncertainty for the cavity radius of implicit solvation models to be used for transition metal atoms. To give an example, the default cavity radius for Pt used in

the PCM (Gaussian),[40] COSMO-RS (Turbomole/COSMOtherm),[41-44] SM8 (universal solvation model),[45] and PBF (Jaguar)[46] solvation models are 2.332, 2.223, 1.740, and 1.377 Å, respectively. It seems that even if program codes report solvation model parameters for transition metal elements, these parameters have not been verified extensively since standard databases used for solvation model parameterization do not contain transition metal elements.[47] Fortunately, the cavity radius parameter of the transition metal is only of importance in implicit solvent models if the surface segments of the metal atom are exposed to the solvent, i.e., the metal is not fully surrounded by ligands. This is indeed the case for most catalysis studies of supported nanoparticles in solution; however, it is usually not the case for fully coordinated transition metal complexes of importance in homogeneous catalysis studies, explaining why the reliability of these parameters has been of less concern in the past. Figure 2.1 illustrates an extreme example of the importance of the cavity radius on the predicted water solvent effect on an adsorbed OH species on Ru(0001) computed with our implicit solvation method for metal surfaces (iSMS).[24] While increasing the Turbomole default cavity radius for Ru by 10% (which leads approximately to the PCM default radius in Gaussian) changes the solvation energy by only ~0.5 kcal/mol; reducing the cavity radius by 10% (which leads approximately to the SM8 default radius) changes the solvation energy by more than 6 kcal/mol. We stress that the application of the isodensity approach, that avoids specifying cavity radii in implicit solvation models as done in VASPsol,[48] has also its challenges considering that a single isodensity value has to be specified (i.e., there is less flexibility in optimizing the solvation model) and we have observed for metal systems that the solvation energy varies significantly in the typical range of isodensity values of

0.001-0.003 a.u. (VASPsol uses an isodensity value of 0.0025 e/Å^3 which has been optimized together with other parameters by comparing a number of molecular solvation energies in water[48]).

Microsolvation. To address the challenge of site-specific interactions in continuum solvation models, mixed continuum models are often adopted, in which in addition to the implicit solvent a few (usually one or two) solvent molecules are explicitly included to the *ab initio* description of the reaction system to better characterize, e.g., hydrogen bonding.[49] This approach, dubbed as *microsolvation,*[49-51] has been successfully applied for the accurate prediction of the pK_a values of mono and polyprotic acids in aqueous solution and should be very accurate whenever the solute-(explicit) solvent interaction is strong enough that it can be well described within the harmonic approximation along the whole reaction coordinate.[52-53] However, for most applications the solute-solvent interaction is sufficiently weak or changes significantly along the reaction coordinate that it is likely very challenging to obtain reliable results with the microsolvation approach. Practical challenges are related to (1) the solvation model correctly reproducing the boundary condition between the solute and the bulk,[54-56] (2) difficulties associated with the correct placement and orientation of the individual solvent molecules, and (3) the inability to evaluate entropic effects beyond the harmonic approximation associated with the explicit solvent molecules.[23]

Explicit solvation models using empirical/fitted force fields. A classical force field or empirical potential description of a solid-liquid interface system is computationally very efficient and has been used to simulate thousands of atoms for nanoseconds as performed for example with the ReaxFF force field in the study of hydrogen hopping at

the silica-water interface[57] and with neural network potentials for the study of the water-Cu(111) interface.[27] We consider these approaches to be very interesting, although the potential parameterization and transferability of potential parameters[58] remains a formidable task such that we consider this approach to be less attractive for biomass catalysis applications, where distinct, chemically different bonds are broken and formed. Getman and coworkers[33,59] have recently adopted a combination of classical MD simulations and DFT calculations for computing adsorption and reaction energies at solid-liquid interfaces. Their approach is based on classical (force field) MD simulations for generating characteristic structures that are subsequently refined by quantum chemical DFT calculations. Unfortunately, they stated that the proposed method is unable to describe the water-adsorbate interactions for larger adsorbates (e.g., $C_3H_7O_3*$).[33]

Explicit hybrid (QM/MM) models. A rational improvement would be the use of a well calibrated multilevel quantum mechanical (QM) and molecular mechanical (MM) method[60-63] with a proper free energy estimator. In this class of methods, all atoms involved in the reaction coordinate of an elementary process are treated quantum mechanically while the rest of the system is described classically. Due to the first principles treatment of the bond breaking/forming region, parameterization of MM atoms is significantly facilitated and the success of these models in the enzyme and homogeneous catalysis communities have been highlighted with the 2013 Nobel prize for chemistry to Karplus, Levitt, and Warshel.

In the following, we describe our explicit solvation model for metal surface[64] (eSMS) method which is such an explicit, hybrid (QM/MM) approach for metal surfaces that is conceptionally similar to the ONIOM method used in the homogeneous and

enzyme catalysis community.[65-66] Our fundamental idea has been that while the electrostatic interaction between solvent molecules and adsorbed moieties is long ranged requiring large simulation systems, the indirect effect of solvent molecules on the free energy of elementary processes on a transition metal surface by changing the electron density of surface metal atoms is short ranged (a consequence of the mobile charge carriers in metals screening electric fields). As a result, the energy of an adsorbed moiety on a metal surface in a liquid (aqueous) reaction environment can be described as a perturbation (small or large) from the system in vacuum (best described through periodic slab models), where the perturbation is described by cluster models embedded in a point-charge field of the solvent. In other words, for liquid water:

$$E^{water}_{surface+adsorbate} = E^{vacuum}_{surface+adsorbate} + (E^{water}_{cluster+adsorbate} - E^{vacuum}_{cluster+adsorbate}) \quad (2.1)$$

where, $E^{vacuum}_{surface+adsorbate}$ is the plane wave DFT energy of the periodic metal slab in absence of water (computed using VASP 5.3[67-68]), $E^{water}_{cluster+adsorbate}$ is the QM/MM energy of the system with water molecules and metal atoms away from the reaction zone being replaced by MM models, and $E^{vacuum}_{cluster+adsorbate}$ is the QM/MM energy of the system with the same treatment of metal atoms in absence of water. The last two energy terms are computed in our workflow using the non-periodic gaussian-orbital based electronic structure program package TURBOMOLE 6.5[41,69-70] (one QM calculation in the electrostatic mean field of water molecules[71-73] and one calculation in the absence of water) and the force field based molecular dynamics code DL_POLY 4.03.[74] To afford sampling of the water/solvent configuration space, only one electronic structure calculation can be performed for a given configuration of QM atoms in the evaluation of

$E^{water}_{cluster+adsorbate}$ and we use the fixed charge approximation[73] as commonly done in the enzyme community (also validated by us[64]) when calculating the system energy for different water conformations. Having determined an efficient yet accurate interaction potential for our reaction system at a metal-water interface that is based on a hybrid QM/MM approach, we can use various tools developed in the enzyme community for computing free energy differences and barriers and we have implemented the QM/MM minimum free energy path (QM/MM-MFEP) method for optimizing the intrinsic reaction coordinate on a quantum chemical potential of mean force (PMF) surface in our program codes.[75-78]

Finally, we briefly note that alternative hybrid (QM/MM) solvent models such as 3D-RISM-KH that have their roots in the integral equation theory of liquids and that describe the solvent by probabilistic radial distributions functions (RDF) have recently been developed.[79-81] These methods promise to significantly reduce the computational sampling effort of hybrid QM/MM models. However, these novel theories also require an interaction potential between the solvent and the metal (a limitation of all QM/MM methods) and current implementations are limited to 2-body interactions,[82] i.e., they can likely not be used for metallic systems. Finally, these integral equation theories cannot be more accurate than our explicit hybrid (QM/MM) model since they involve an additional approximation in regard to the closure relation, and Fujita and Yamamoto observed a substantial size-dependent error in solvation free energies for hydrophobic solutes computed by 3D-RISM.[83]

In the following, we employ our computational eSMS approach for the initial O-H and C-H bond cleavages of ethylene glycol (EG) over Pt(111) under aqueous phase

processing conditions and contrast our explicit solvation (eSMS) results with implicit (iSMS) solvation data (see computational details in the supporting info). We have chosen EG as the probe reactant since EG is the smallest, i.e., computationally most accessible, oxygenated hydrocarbon with a C-C bond and a C:O stoichiometric ratio of 1:1 that has been used as a representative reactant molecule for carbohydrates in various experimental studies.[84-86] A detailed first principles (PBE[87-88]) microkinetic modeling study of EG reforming on a Pt(111) model surface suggested that in condensed water (implicit solvation with iSMS[24]) the initial O-H splitting and the subsequent α-H abstraction to glycoaldehyde are the most kinetically relevant elementary steps over a wide range of temperatures (373-673K), with Campbell degree of rate control values, X_{RC}, at 500 K of 0.69 and 0.26, respectively (deviations from zero indicate rate control).[89] Calculations further indicated that the aqueous phase significantly facilitates the primary C-H bond scission relative to the O-H bond scission at all temperatures (see free energy barriers in Table 2.1). Along these lines, Gu et al.[90] have recently pointed out that O-H bond cleavage for aqueous phase reforming of ethanol over Pt(111) is thermodynamically unfavorable compared to C-H cleavage. They used the periodic continuum solation model, VASPsol, to derive this conclusion.[48] However, it has long been argued that the inclusion of explicit water in the reaction system significantly facilitates the O-H bond scission on hydrophobic interfaces through hydrogen bonding or $H_{(2n+1)}O_n^+$complex formation[91-97] – an effect not directly examined in previous computational studies utilizing implicit solvation models. Hydrogen bonding and a strong electrostatic interaction between an adsorbed species and the water solvent should lead to a considerable enthalpic stabilization. Following the classic example of the "Iceberg"

model,[32,98] such an enthalpic stabilization leads to an increased ordering of water molecules around the solute which again comes with an entropy penalty and hence, it is critical to accurately describe the anticipating entropy-enthalpy compensation that cannot be described by microsolvation or the bilayer adsorption/ice model. A promotional effect of water acting as a co-catalyst for H-abstraction during the dissociative chemisorption of alcohols has also been suggested in some experimental studies.[99-100] Overall, it seems that computational models that do not sample configuration space (e.g., implicit solvent models) are challenged with accurately describing the aqueous solvent effect in O-H bond cleavage originating from directional hydrogen bonding. Here, we test if our explicit solvation model, eSMS, might be able to predict a solvation effect for O-H cleavage in EG more in agreement with intuition and experimental studies.

$$CH_2OHCH_2OH ** + * \leftrightarrow CH_2OCH_2OH ** + H * \quad (2.2)$$

Accurate estimation of free energy differences between any two states requires significant phase space overlap which can be accomplished by initiating a sufficient number of transitional images between them. Figure 2.2 illustrates a free energy profile (potential of mean force - PMF) by introducing 39 intermediate states between the reactant and the transition state and 15 intermediate images between the transition state and the product state. In all cases, it has been ensured that the difference in energy between two adjacent images is always lower than the thermal energy ($k_BT = 0.043\ eV\ at\ 500K$). Our eSMS calculations indicate that an aqueous reaction environment has a significant impact on both the free energy of reaction ($\Delta\Delta G_{rxn} = -0.37 \pm 0.08\ eV$) and the free energy of activation ($\Delta\Delta G^{\dagger} = -0.46 \pm 0.05\ eV$) for the primary O-H scission of ethylene glycol. This contrast with our implicit (iSMS)

computations, where we found at 500 K $\Delta\Delta G_{rxn} = -0.09\ eV$ and $\Delta\Delta G^{\dagger} = -0.02\ eV$. Due to the ambiguity associated with the definition of the Pt cavity radius in implicit solvation models,[40,43,45-46] we repeated all calculations with a 10% smaller and larger Pt cavity. No noteworthy effect on free energies (smaller 0.03 eV) was detected because of a change in Pt cavity radius.

To better understand the underlying reason of the solvent stabilization of the transition state and dissociated product state (all approximated to be identical in all reaction environments), we repeated our explicit solvation calculations (eSMS) at five different temperatures, ranging from 460 to 540 K, and computed the solvent effect on the heat of reaction. The results shown in Figure 2.3 indicate that due to the strong hydrogen bonding between adsorbed species and water, there is a strong enthalpic stabilization ($\Delta\Delta H_{rxn} = -0.85\ eV$) that is partially compensated by a strong entropic contribution ($-T\Delta\Delta S_{rxn} = +0.55\ eV\ at\ 500K$) in the computation of the free energy. Again, our implicit (iSMS) method predicts a much smaller enthalpic and entropic solvent effect of $\Delta\Delta H_{rxn} = -0.13\ eV$ and $-T\Delta\Delta S_{rxn} = +0.05\ eV\ at\ 500K$. Interestingly, both solvation models agree qualitatively with the concept derived for two interacting dipoles[101-102] that the free energy of solvation is approximately half the solvation enthalpy due to the free energy cost associated with the loss of configurational freedom.

Next, we turn our focus on the α-H bond scission of ethylene glycol to glycoaldehyde.

$$CH_2OHCH_2OH** + * \leftrightarrow CHOHCH_2OH** + H* \tag{2.3}$$

Figure 2.4 illustrates a free energy profile for the C-H bond cleavage comprised of 23 intermediate states between the reactant and the transition state, and 25 intermediary images between the transition state and the product state. Our eSMS calculations indicate that the aqueous reaction environment has only a minor impact on both the free energy of reaction ($\Delta\Delta G_{rxn} = -0.02 \pm 0.06\ eV$) and free energy of activation ($\Delta\Delta G^{\dagger} = -0.16 \pm 0.05\ eV$) at 500 K. The difference between the effect of water for the C-H and O-H bond cleavage reactions can be traced back to the presence of a well-exposed (to the aqueous phase) oxygen atom in the reacting hydroxyl group that can accept hydrogen bonds and can particularly be stabilized by the surrounding water molecules in the transition and product state. In contrast, in the C-H bond cleavage the carbon atom cannot accept hydrogen bonds and interacts similarly with the surrounding water in the reactant and product state. Only in the transition state, the elongated C-H bond is stabilized by surrounding electrostatic and possibly hydrogen-bond interactions between the dissociating hydrogen atom and the surrounding water molecules.

Considering that hydrogen bonding is of lesser importance in the C-H bond cleavage, our explicit (eSMS) solvation model calculations are in good agreement with our implicit (iSMS) solvation data (see Table 2.1). Our implicit solvation model predicts that the presence of water has virtually no impact on the free energy of reaction ($\Delta\Delta G_{rxn} = +0.005\ eV$) and only a small favorable effect on the kinetics ($\Delta\Delta G^{\dagger} = -0.08\ eV$) at 500 K.

Since any stabilization of adsorbed moieties in our continuum solvation model, that is based on COSMO-RS,[43,103] has to originate from the polarization surface charge densities (SCD) (even hydrogen bonding is empirically parameterized based on SCD[104-

[105]), we examined the charge densities of the surface segments along the C-H reaction coordinate to understand the implicit solvent effect on free energies for this reaction in more detail. We note that the hydroxyl groups are equally exposed to the aqueous phase in the reactant (RS), transition (TS), and product states (PS) such that they do not significantly contribute to a change in solvation free energy. In both the reactant and product state the most polarized SCD segments in the proximity of the reacting moiety are somewhat similar ($\sigma_{\alpha C-H}^{RS}$= -0.70 $\frac{e}{Nm^2}$ versus $\sigma_{\alpha C-H}^{PS}$= -0.90 $\frac{e}{Nm^2}$) (see Supporting Information, Figure A.1.4 (a) and (c)). This contrasts with the generally higher surface charge densities around the reacting moiety in the transition state with a maximum value of $\sigma_{\alpha C-H}^{TS}$= -1.35 $\frac{e}{Nm^2}$ (see Figure A.1.4 (b)). The larger SCDs in the transition state lead to a stronger interaction with the surrounding aqueous phase and a stabilization of the transition state relative to the reactant state for C-H bond cleavage on Pt(111).

To conclude, we examined some of the prevailing approaches for modeling condensed phases in heterogeneous catalysis. All atomistic quantum chemical (DFT) methods and classical force field simulations are currently not the most practical approaches for describing solvent effects in heterogeneous catalysis due to the large computational expense and limited/unknown accuracy, respectively. Microsolvation and bilayer adsorption/ice models are most appropriate whenever the system temperature is low enough or the solvent-solute interaction strong enough that entropic effects along the reaction coordinate can be described accurately by the harmonic approximation. There is a risk that due to a lack of extensive configuration space sampling, these models significantly overestimate solvent effects whenever the harmonic approximation breaks down. Likely, these models are more appropriate for predicting enthalpies of solvation

than free energies of solvation. In agreement with prior reports, we found that enthalpies of solvation are generally larger than free energies of solvation (roughly twice as large although the overestimation is temperature and system dependent). Next, the implicit or continuum solvation models are the easiest models to apply that can convey qualitative results for the computation of solvent effects. They are most appropriate whenever directional hydrogen bonding is not present or does not change significantly along a reaction coordinate. We found these models to underestimate strong hydrogen bonding effects. Also, the parameterization for transition metal element dependent parameters needs a more thorough validation. Finally, we deem QM/MM models to be currently the most appropriate models for predicting solvation effects in heterogeneous catalysis with an adequate balance between computational expense and chemical accuracy in regard to potential energy surface description and configuration space sampling. In this contribution, we reviewed such a hybrid QM/MM model, called eSMS, and applied it to C-H and O-H bond cleavage of ethylene glycol on Pt(111) under aqueous phase reforming conditions to explain the counter-intuitive (and likely wrong) result of implicit solvation models that predict hardly any aqueous solvent effect in O-H bond cleavage. Explicit solvation (eSMS) effect calculations agree with the implicit solvation models for C-H bond cleavage where they both predict a small solvation effect. In contrast and unlike the implicit solvation models, our explicit solvation model predicts a larger solvent stabilization of both the transition state and product state in O-H bond cleavage due to its ability to approximately describe hydrogen bonding. As a result, O-H bond dissociations are significantly favored over C-H bond dissociations under aqueous processing conditions of biomass.

It should be noted here that our eSMS model is currently limited to the computation of free energy differences of processes at solid-liquid interfaces and the successful application of the model hinges on the availability of metal-water interaction potentials (we generally assume that the adsorbed hydrocarbon-water interaction can be described approximately with current force fields developed in the homogeneous and enzyme catalysis communities). As a result, it can currently not be applied to, e.g., high index metal surfaces, supported nanoparticle models, hydroxylated oxides, zeolites etc.[106-108] However, we are currently in the process of developing artificial neural network potentials for the description of metal-water interactions for various transition metal elements and surface structures.[27,109-110] Also, we aim to introduce required modifications to our eSMS model to compute free energies of the adsorption/desorption processes in the near future.

2.1 Acknowledgements

The authors recognize the support of the United States Department of Energy, Office of Basic Energy Services (DE-SC0007167). Computing resources provided by the National Energy Research Scientific Computing Cluster (NERSC), Texas Advanced Computing Center (TACC), and Pacific Northwest National Laboratory (PNNL) are gratefully acknowledged. Dr. Michael R. Shirts from the University of Colorado, Boulder, is acknowledged for helping with the implementation of the Bennett Acceptance Ratio (BAR) as the free energy estimator. Dr. Rachel B. Getman from the Clemson University and Dr. Ayman M. Karim from Virginia Tech are thanked for helpful discussions.

2.2 Tables and Figures

Table 2.1: Aqueous phase effects on the free energy of reaction, free energy of activation, heat of reaction, and entropic contributions for O-H and C-H model reactions at 500 K on Pt(111) using implicit and explicit solvation models. Vapor phase PBE calculations predicted at 500 K for C-H bond cleavage: $\Delta H_{rxn} = -0.48\ eV$, $\Delta G_{rxn} = -0.40\ eV$, $\Delta G^{\dagger} = +0.73\ eV$ and for O-H bond cleavage: $\Delta H_{rxn} = +0.38\ eV$, $\Delta G_{rxn} = +0.45\ eV$, $\Delta G^{\dagger} = +0.70\ eV$.

Reaction	Solvation model	$\Delta\Delta G_{rxn}$ (eV)	$\Delta\Delta G^{\dagger}$ (eV)	$\Delta\Delta H_{rxn}$ (eV)	$-T\Delta\Delta S_{rxn}$ (eV)
$CH_2OHCH_2OH * * + * \leftrightarrow CH_2OCH_2OH * * + H *$	iSMS	-0.09	-0.02	-0.13	0.05
	eSMS	-0.37±0.08	-0.46±0.05	-0.85	0.55
$CH_2OHCH_2OH * * + * \leftrightarrow CHOHCH_2OH * * + H *$	iSMS	0.01	-0.08	5.68×10^{-3}	-1.21×10^{-4}
	eSMS	-0.02±0.06	-0.16±0.05	-	-

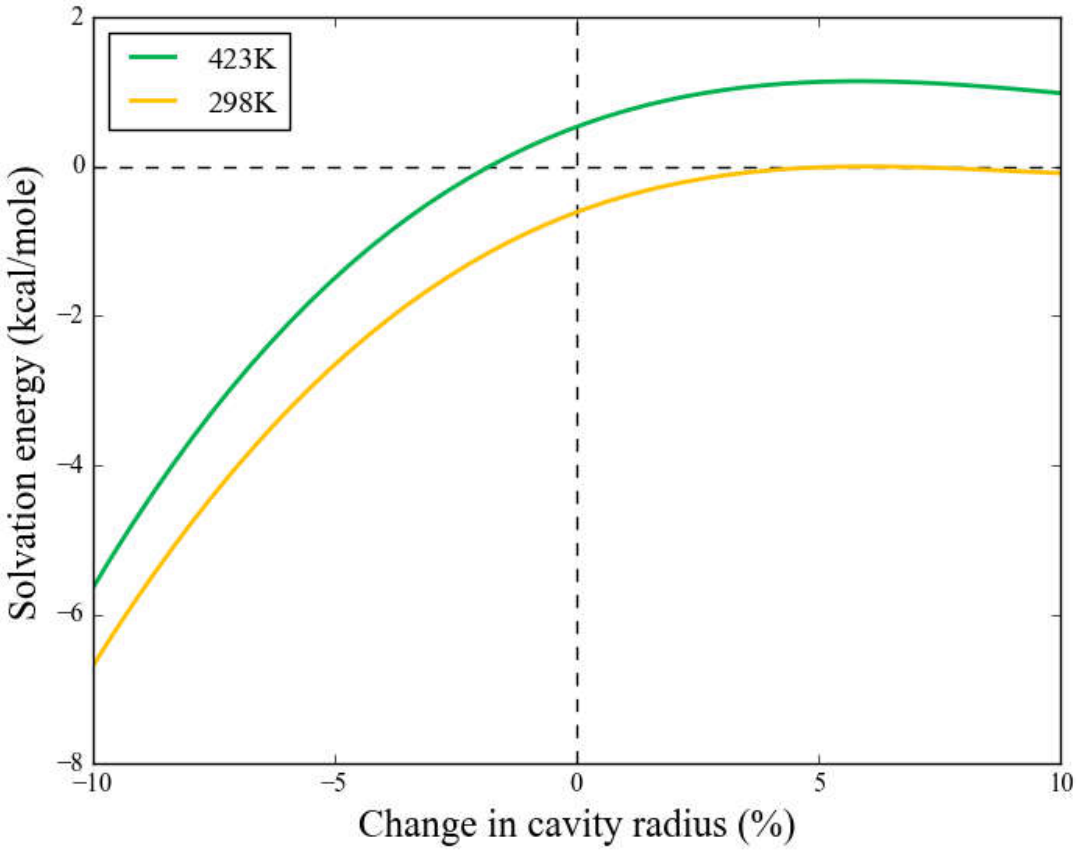

Figure 2.1: Effect of cavity radius of Ru (±10% of the Turbomole value of 2.223 Å) on the water solvation free energy of an adsorbed OH group (HCP) on Ru(0001) at 298 and 423 K. Plotted is the difference in the adsorption free energy of OH in the presence of liquid water (OH(g) + ∗(l) ↔ OH∗(l)) and absence of any aqueous solvent (OH(g) + ∗(g) ↔ OH∗(g)).

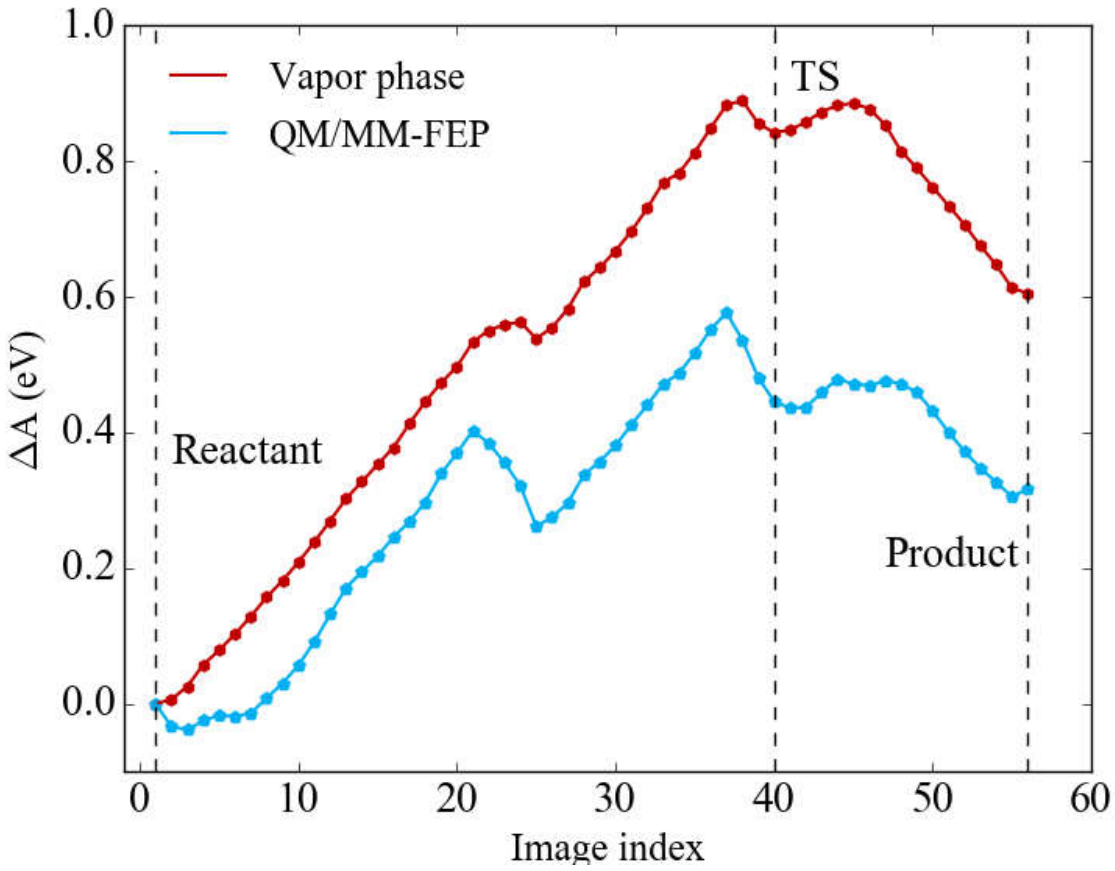

Figure 2.2: Free energy profile for O-H bond cleavage of ethylene glycol in vapor and aqueous phases over a Pt(111) model surface at 500 K (without considering vibrational contributions of the adsorbed ethylene glycol species to the partition function). The aqueous phase profile has been plotted for a single QM/MM calculation using Bennett Acceptance Ratio[111] (BAR) as the free energy estimator among the 10 QM/MM calculations performed. The transition state appears to have a lower energy compared to adjacent images because the intermediate images introduced along the approximate reaction coordinate were not optimized to the minimum free energy path.

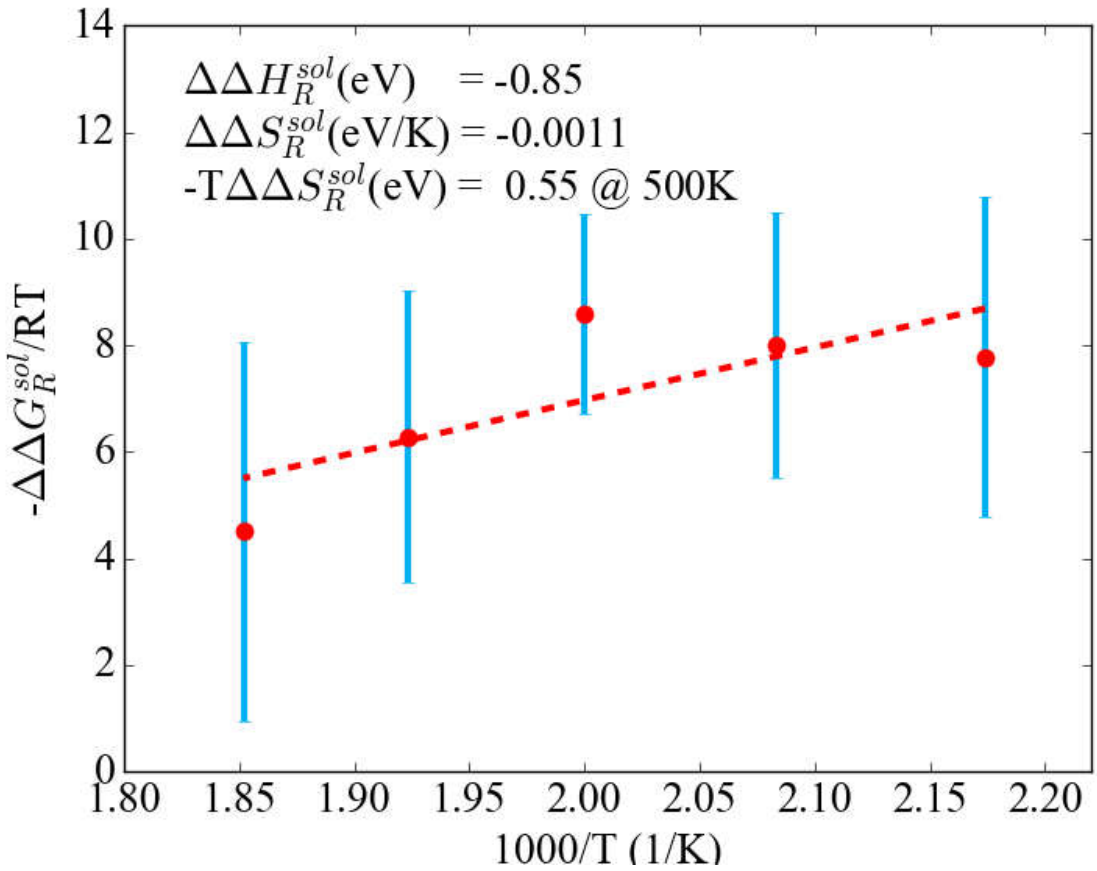

Figure 2.3: Temperature dependence of aqueous solvation effect on the free energy reaction for the primary O-H bond scission of ethylene glycol over a Pt(111) model surface. The error bars indicate 95% confidence interval for the aqueous phase effect on the free energy of the specified reaction.

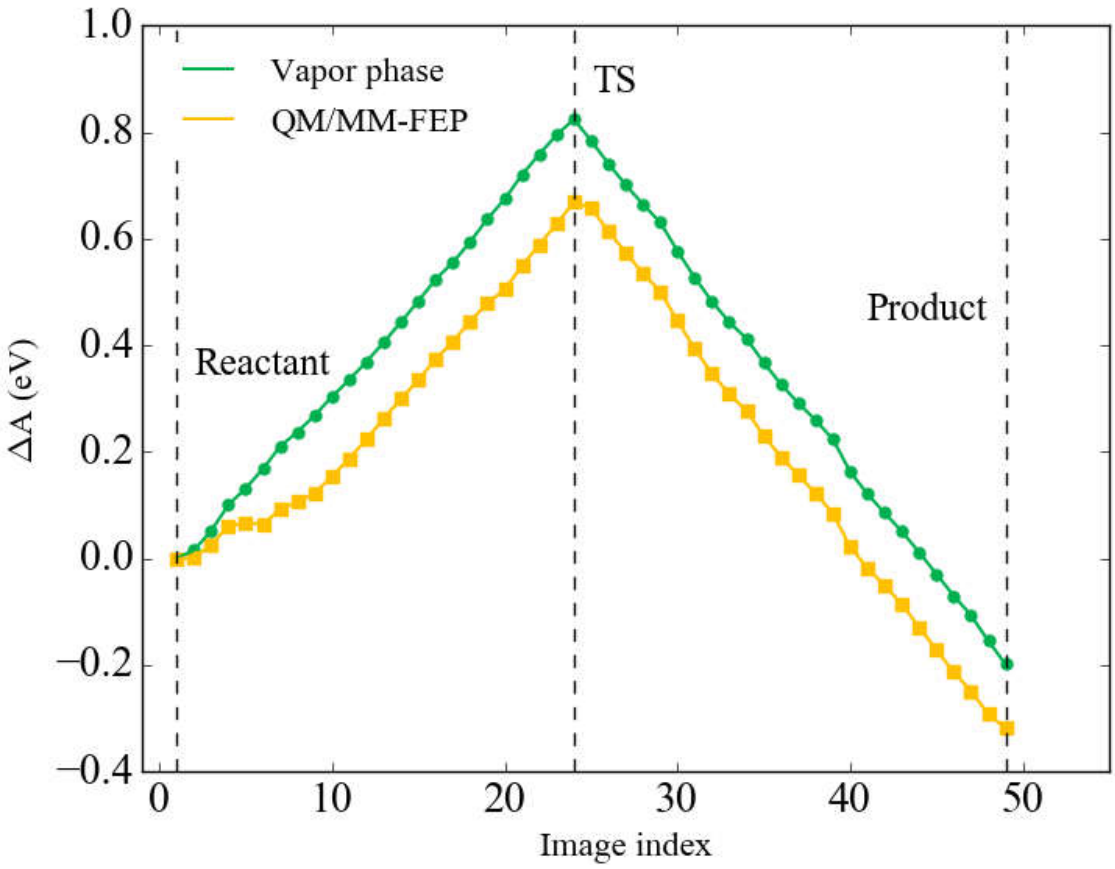

Figure 2.4: Free energy profile for C-H bond cleavage of ethylene glycol in vapor and aqueous phases over a Pt(111) model surface at 500 K (without considering vibrational contributions to the partition function). The aqueous phase profile has been drawn for a single QM/MM calculation using Bennett Acceptance Ratio[111] (BAR) as the free energy estimator among the 10 QM/MM calculations performed.

2.3 Bibliography

1. Berthelot, M.; Saint-Gilles, L. P. *Ann. Chim.* **1863,** *68*, 225.
2. Menschutkin, N. A. *Z. Physik. Chem.* **1890,** *5*, 589.
3. Cram, D. J.; Rickborn, B.; Kingsbury, C. A. *Journal of the American Chemical Society* **1961,** *83*, 3678-3687.
4. Reichardt, C.; Welton, T. In *Solvents and Solvent Effects in Organic Chemistry*, 4th, updated and enl. ed.; Reichardt, C.; Welton, T., Eds.; Wiley-VCH: Weinheim, Germany, 2011; p 177.
5. Dyson, P. J.; Jessop, P. G. *Catalysis Science & Technology* **2016,** *6*, 3302-3316.
6. Wan, H. J.; Vitter, A.; Chaudhari, R. V.; Subramaniam, B. *J Catal* **2014,** *309*, 174-184.
7. Hidalgo-Carrillo, J.; Aramendia, M. A.; Marinas, A.; Marinas, J. M.; Urbano, F. J. *Appl Catal a-Gen* **2010,** *385*, 190-200.
8. Behtash, S.; Lu, J. M.; Faheem, M.; Heyden, A. *Green Chem* **2014,** *16*, 4427-4428.
9. Akpa, B. S.; D'Agostino, C.; Gladden, L. F.; Hindle, K.; Manyar, H.; McGregor, J.; Li, R.; Neurock, M.; Sinha, N.; Stitt, E. H.; Weber, D.; Zeitler, J. A.; Rooney, D. W. *J Catal* **2012,** *289*, 30-41.
10. Ebbesen, S. D.; Mojet, B. L.; Lefferts, L. *J Catal* **2007,** *246*, 66-73.
11. Zope, B. N.; Hibbitts, D. D.; Neurock, M.; Davis, R. J. *Science* **2010,** *330*, 74-78.
12. Hibbitts, D. D.; Neurock, M. *J Catal* **2013,** *299*, 261-271.
13. Rossmeisl, J.; Skulason, E.; Bjorketun, M. E.; Tripkovic, V.; Norskov, J. K. *Chem Phys Lett* **2008,** *466*, 68-71.
14. Huang, Y. F.; Nielsen, R. J.; Goddard, W. A.; Soriaga, M. P. *Journal of the American Chemical Society* **2015,** *137*, 6692-6698.
15. Cheng, T.; Xiao, H.; Goddard, W. A. *J Phys Chem Lett* **2015,** *6*, 4767-4773.
16. Chant, K.; Norskov, J. K. *J Phys Chem Lett* **2016,** *7*, 1686-1690.
17. Huber, G. W.; Iborra, S.; Corma, A. *Chemical Reviews* **2006,** *106*, 4044-4098.
18. Corma, A.; Iborra, S.; Velty, A. *Chemical Reviews* **2007,** *107*, 2411-2502.
19. Stocker, M. *Angewandte Chemie-International Edition* **2008,** *47*, 9200-9211.
20. Honkala, K.; Hellman, A.; Remediakis, I. N.; Logadottir, A.; Carlsson, A.; Dahl, S.; Christensen, C. H.; Norskov, J. K. *Science* **2005,** *307*, 555-558.
21. Topsoe, H.; Hinnemann, B.; Norskov, J. K.; Lauritsen, J. V.; Besenbacher, F.; Hansen, P. L.; Hytoft, G.; Egeberg, R. G.; Knudsen, K. G. *Catal Today* **2005,** *107-08*, 12-22.
22. Linic, S.; Jankowiak, J.; Barteau, M. A. *J Catal* **2004,** *226*, 245-246.
23. Taylor, C. D.; Neurock, M. *Current Opinion in Solid State & Materials Science* **2005,** *9*, 49-65.
24. Faheem, M.; Suthirakun, S.; Heyden, A. *J Phys Chem C* **2012,** *116*, 22458-22462.
25. Ochterski, J. W. In *Thermochemistry in Gaussian*, Gaussian, Inc.: Wallingford,CT, 2000.
26. Tao, L.; Chen, G. J.; Zhao, L. X.; Xu, J. T.; Huang, E.; Liu, A. P.; Marquis, C. P.; Davis, T. P. *Chemistry-an Asian Journal* **2011,** *6*, 1398-1404.
27. Natarajan, S. K.; Behler, J. *Phys Chem Chem Phys* **2016,** *18*, 28704-28725.
28. Car, R.; Parrinello, M. *Phys Rev Lett* **1985,** *55*, 2471-2474.

29. Carloni, P.; Rothlisberger, U.; Parrinello, M. *Accounts of Chemical Research* **2002,** *35*, 455-464.
30. Iftimie, R.; Minary, P.; Tuckerman, M. E. *Proceedings of the National Academy of Sciences of the United States of America* **2005,** *102*, 6654-6659.
31. Chen, L. D.; Urushihara, M.; Chan, K. R.; Norskov, J. K. *Acs Catal* **2016,** *6*, 7133-7139.
32. Doering, D. L.; Madey, T. E. *Surf Sci* **1982,** *123*, 305-337.
33. Bodenschatz, C. J.; Sarupria, S.; Getman, R. B. *J Phys Chem C* **2015,** *119*, 13642-13651.
34. Badan, C.; Heyrich, Y.; Koper, M. T. M.; Juurlink, L. B. F. *J Phys Chem Lett* **2016,** *7*, 1682-1685.
35. Eriksson, A. E.; Baase, W. A.; Zhang, X. J.; Heinz, D. W.; Blaber, M.; Baldwin, E. P.; Matthews, B. W. *Science* **1992,** *255*, 178-183.
36. Funahashi, J.; Takano, K.; Yutani, K. *Protein Eng* **2001,** *14*, 127-134.
37. Kleinjung, J.; Fraternali, F. *Curr Opin Struc Biol* **2014,** *25*, 126-134.
38. Zhang, J.; Zhang, H. Y.; Wu, T.; Wang, Q.; van der Spoel, D. *J Chem Theory Comput* **2017,** *13*, 1034-1043.
39. Behtash, S.; Lu, J. M.; Walker, E.; Mamun, O.; Heyden, A. *J Catal* **2016,** *333*, 171-183.
40. Frisch, M. J.; al, e. In *Gaussian 09*, Gaussian, Inc.: Wallingford, CT, 2009.
41. Ahlrichs, R.; Bar, M.; Haser, M.; Horn, H.; Kolmel, C. *Chem Phys Lett* **1989,** *162*, 165-169.
42. Schafer, A.; Klamt, A.; Sattel, D.; Lohrenz, J. C. W.; Eckert, F. *Phys Chem Chem Phys* **2000,** *2*, 2187-2193.
43. Klamt, A. In *COSMO-RS: From Quantum Chemistry to Fluid Phase Thermodynamics and Drug Design*, 1st ed.; Elsevier Science Ltd.: Amsterdam, Netherlands, 2005.
44. Eckert, F.; Diedenhofen, M.; Klamt, A. *Molecular Physics* **2010,** *108*, 229-241.
45. Marenich, A. V.; Olson, R. M.; Kelly, C. P.; Cramer, C. J.; Truhlar, D. G. *J Chem Theory Comput* **2007,** *3*, 2011-2033.
46. Bochevarov, A. D.; Harder, E.; Hughes, T. F.; Greenwood, J. R.; Braden, D. A.; Philipp, D. M.; Rinaldo, D.; Halls, M. D.; Zhang, J.; Friesner, R. A. *Int J Quantum Chem* **2013,** *113*, 2110-2142.
47. Marenich, A. V.; Cramer, C. J.; Truhlar, D. G. *Journal of Chemical Theory and Computation* **2013,** *9*, 609-620.
48. Mathew, K.; Sundararaman, R.; Letchworth-Weaver, K.; Arias, T. A.; Hennig, R. G. *J Chem Phys* **2014,** *140*, 084106:1-8.
49. Michel, C.; Zaffran, J.; Ruppert, A. M.; Matras-Michalska, J.; Jedrzejczyk, M.; Grams, J.; Sautet, P. *Chem Commun* **2014,** *50*, 12450-12453.
50. Desai, S. K.; Pallassana, V.; Neurock, M. *J Phys Chem B* **2001,** *105*, 9171-9182.
51. Liu, Y.; Gregersen, B. A.; Hengge, A.; York, D. M. *Biochemistry-Us* **2006,** *45*, 10043-10053.
52. Kelly, C. P.; Cramer, C. J.; Truhlar, D. G. *J Phys Chem A* **2006,** *110*, 2493-2499.
53. Marenich, A. V.; Ding, W. D.; Cramer, C. J.; Truhlar, D. G. *J Phys Chem Lett* **2012,** *3*, 1437-1442.
54. Im, W.; Roux, B. *J Chem Phys* **2001,** *115*, 4850-4861.

55. Warshel, A.; Sharma, P. K.; Kato, M.; Parson, W. W. *Bba-Proteins Proteom* **2006,** *1764*, 1647-1676.
56. Kamerlin, S. C. L.; Haranczyk, M.; Warshel, A. *Chemphyschem* **2009,** *10*, 1125-1134.
57. Fogarty, J. C.; Aktulga, H. M.; Grama, A. Y.; van Duin, A. C. T.; Pandit, S. A. *J Chem Phys* **2010,** *132*, 174704:1-10.
58. Sato, F.; Hojo, S.; Sun, H. *J Phys Chem A* **2003,** *107*, 248-257.
59. Xie, T. J.; Sarupria, S.; Getman, R. B. *Mol Simulat* **2017,** *43*, 370-378.
60. Warshel, A.; Levitt, M. *J Mol Biol* **1976,** *103*, 227-249.
61. Field, M. J.; Bash, P. A.; Karplus, M. *J Comput Chem* **1990,** *11*, 700-733.
62. Bentzien, J.; Muller, R. P.; Florian, J.; Warshel, A. *J Phys Chem B* **1998,** *102*, 2293-2301.
63. Zhang, Y. K.; Liu, H. Y.; Yang, W. T. *J Chem Phys* **2000,** *112*, 3483-3492.
64. Faheem, M.; Heyden, A. *J Chem Theory Comput* **2014,** *10*, 3354-3368.
65. Svensson, M.; Humbel, S.; Froese, R. D. J.; Matsubara, T.; Sieber, S.; Morokuma, K. *Journal of Physical Chemistry* **1996,** *100*, 19357-19363.
66. Chung, L. W.; Hirao, H.; Li, X.; Morokuma, K. *Wiley Interdisciplinary Reviews-Computational Molecular Science* **2012,** *2*, 327-350.
67. Kresse, G.; Furthmuller, J. *Comp Mater Sci* **1996,** *6*, 15-50.
68. Kresse, G.; Furthmuller, J. *Phys Rev B* **1996,** *54*, 11169-11186.
69. Treutler, O.; Ahlrichs, R. *J Chem Phys* **1995,** *102*, 346-354.
70. Von Arnim, M.; Ahlrichs, R. *J Comput Chem* **1998,** *19*, 1746-1757.
71. Burow, A. M.; Sierka, M.; Doebler, J.; Sauer, J. *Journal of Chemical Physics* **2009,** *130*, 174710.
72. Gotz, K.; Meier, F.; Gatti, C.; Burow, A. M.; Sierka, M.; Sauer, J.; Kaupp, M. *Journal of Computational Chemistry* **2010,** *31*, 2568-2576.
73. Hu, H.; Lu, Z. Y.; Parks, J. M.; Burger, S. K.; Yang, W. T. *J Chem Phys* **2008,** *128*, 034105:1-18.
74. Todorov, I. T.; Smith, W.; Trachenko, K.; Dove, M. T. *J Mater Chem* **2006,** *16*, 1911-1918.
75. Hu, H.; Lu, Z. Y.; Yang, W. T. *Journal of Chemical Theory and Computation* **2007,** *3*, 390-406.
76. Hu, H.; Yang, W. T. *Annual Review of Physical Chemistry* **2008,** *59*, 573-601.
77. Hu, H.; Yang, W. T. *Journal of Molecular Structure-Theochem* **2009,** *898*, 17-30.
78. Hu, H.; Yang, W. T. *Journal of Physical Chemistry B* **2010,** *114*, 2755-2759.
79. Sato, H. *Physical Chemistry Chemical Physics* **2013,** *15*, 7450-7465.
80. Kovalenko, A. *Condens Matter Phys* **2015,** *18*, 32601:1-24.
81. Nishihara, S.; Otani, M. *Physical Review B* **2017,** *96*.
82. Roy, D.; Blinov, N.; Kovalenko, A. *Journal of Physical Chemistry B* **2017,** *121*, 9268-9273.
83. Fujita, T.; Yamamoto, T. *Journal of Chemical Physics* **2017,** *147*.
84. Shabaker, J. W.; Huber, G. W.; Davda, R. R.; Cortright, R. D.; Dumesic, J. A. *Catal Lett* **2003,** *88*, 1-8.
85. Huber, G. W.; Shabaker, J. W.; Evans, S. T.; Dumesic, J. A. *Appl Catal B-Environ* **2006,** *62*, 226-235.

86. Salciccioli, M.; Yu, W. T.; Barteau, M. A.; Chen, J. G. G.; Vlachos, D. G. *Journal of the American Chemical Society* **2011,** *133*, 7996-8004.
87. Perdew, J. P.; Burke, K.; Ernzerhof, M. *Phys Rev Lett* **1996,** *77*, 3865-3868.
88. Perdew, J. P.; Burke, K.; Ernzerhof, M. *Phys Rev Lett* **1997,** *78*, 1396-1396.
89. Faheem, M.; Saleheen, M.; Lu, J. M.; Heyden, A. *Catalysis Science & Technology* **2016,** *6*, 8242-8256. **A new transition state for primary C-H cleavage of ethylene glycol was later found which has 0.10 eV lower energy than reported herein.*
90. Gu, G. H.; Schweitzer, B.; Michel, C.; Steinmann, S. N.; Sautet, P.; Vlachos, D. G. *J Phys Chem C* **2017,** *121*, 21510-21519.
91. Desai, S. K.; Neurock, M. *Phys Rev B* **2003,** *68*, 075420:1-7.
92. Hibbitts, D. D.; Loveless, B. T.; Neurock, M.; Iglesia, E. *Angewandte Chemie-International Edition* **2013,** *52*, 12273-12278.
93. Santana, J. A.; Mateo, J. J.; Ishikawa, Y. *J Phys Chem C* **2010,** *114*, 4995-5002.
94. Skachkov, D.; Rao, C. V.; Ishikawa, Y. *J Phys Chem C* **2013,** *117*, 25451-25466.
95. Huang, Z. Q.; Long, B.; Chang, C. R. *Catalysis Science & Technology* **2015,** *5*, 2935-2944.
96. Nie, X. W.; Luo, W. J.; Janik, M. J.; Asthagiri, A. *J Catal* **2014,** *312*, 108-122.
97. Zhang, X. H.; Sewell, T. E.; Glatz, B.; Sarupria, S.; Getman, R. B. *Catal Today* **2017,** *285*, 57-64.
98. Carrasco, J.; Hodgson, A.; Michaelides, A. *Nat Mater* **2012,** *11*, 667-674.
99. Frassoldati, A.; Pinel, C.; Besson, M. *Catal Today* **2011,** *173*, 81-88.
100. Anderson, R.; Griffin, K.; Johnston, P.; Alsters, P. L. *Adv Synth Catal* **2003,** *345*, 517-523.
101. Israelachvili, J. N. In *Intermolecular and Surface Forces (Third Edition)*, Academic Press: San Diego, 2011; pp 71-90.
102. Cramer, C. J. In *Essentials of computational chemistry : theories and models*, J. Wiley: West Sussex, England ; New York, 2002; p xvii, 542 p.
103. Klamt, A. *J Phys Chem-Us* **1995,** *99*, 2224-2235.
104. Klamt, A.; Reinisch, J.; Eckert, F.; Graton, J.; Le Questel, J. Y. *Phys Chem Chem Phys* **2013,** *15*, 7147-7154.
105. Klamt, A.; Reinisch, J.; Eckert, F.; Hellweg, A.; Diedenhofen, M. *Phys Chem Chem Phys* **2012,** *14*, 955-963.
106. Behtash, S.; Lu, J. M.; Mamun, O.; Williams, C. T.; Monnier, J. R.; Heyden, A. *J Phys Chem C* **2016,** *120*, 2724-2736.
107. Delley, B. *Mol Simulat* **2006,** *32*, 117-123.
108. Hou, M. Q.; Mei, Q. Q.; Han, B. X. *J Colloid Interf Sci* **2015,** *449*, 488-493.
109. Behler, J.; Parrinello, M. *Phys Rev Lett* **2007,** *98*, 146401:1-4.
110. Behler, J. *J Phys-Condens Mat* **2014,** *26*, 183001:1-24.
111. Bennett, C. *Journal of Computational Physics* **1976,** *22*, 245-268.

CHAPTER 3

COMPUTATIONAL INVESTIGATION OF AQUEOUS-PHASE EFFECTS ON THE DEHYDROGENATION AND DEHYDROXYLATION OF POLYOLS OVER Pt(111)

Saleheen, M.; Zare, M.; Faheem, M.; Heyden, A.

Submitted to *The Journal of Physical Chemistry C*

3.1 Abstract

Prediction of solvation effects on the kinetics of elementary reactions occurring at metal-water interfaces is of high importance for the rational design of catalysts for the biomass- and electrocatalysis communities. A lack of knowledge of the reliability of various computational solvation schemes for processes on metal surfaces is currently a limiting factor. Using a multilevel quantum mechanical/molecular mechanical (QM/MM) description of the potential energy surface, we determined characteristic time and length scales for typical free energy perturbation (FEP) calculations of bond cleavages in ethylene glycol, a sugar surrogate molecule, over Pt(111). Our approach is based on our explicit solvation model for metal surfaces (eSMS) and the repetition of FEP calculations to estimate confidence intervals. Results indicate that aqueous phase effects on the free energies of elementary processes can be determined with 95% confidence intervals from limited configuration space sampling and the fixed charge approximation used in the QM/MM-FEP methodology of smaller 0.1 eV. Next, we computed the initial O-H, C-H, and C-OH bond cleavages in ethylene glycol over Pt(111) in liquid water utilizing two different metal-water interaction potentials. Our calculations predict that aqueous phase effects are small (< 0.1 eV) for the C-H bond cleavage and the activation barrier of the C-OH bond cleavage. In contrast, solvation effects are large (> 0.35 eV) for the O-H bond cleavage and the reaction free energy of the C-OH bond scission. While the choice of a different Pt-water force field can lead to differences in predicted solvation effects of up to 0.2 eV, the differences are usually smaller (< 0.1 eV) and the trends are always the same. In contrast, implicit solvation methods appear to currently not be able to reliably describe

solvation effects originating from hydrogen bonding for metal surfaces even qualitatively.

3.2 Introduction

The ubiquitous nature of solvents and their pervasive usage in the chemical industry[1] makes the study of solvent effects an important area of investigation. The fact that the presence and nature of solvents can affect chemical equilibria was recognized as early as 1896 with the concurrent revelation of the keto-enol tautomerism in 1,3-dicarbonyl compounds and the nitro-isonitro tautomerism of primary and secondary nitro compounds.[2-5] As evidenced by the seminal work of Menschutkin,[6] it was also demonstrated early on that the rate of chemical reactions can be attuned through the prudent choice of solvents. The role of solvents in homogeneous catalysis has long been systematically investigated and appropriated for industrial applications for several hydrogen addition and abstraction processes,[7-8] oxo-synthesis,[9-12] cross-coupling reactions,[13-15] cycloadditions[16-17] etc. One prominent example of the industrial practice of solvent effects is the aqueous two-phase catalysis in hydroformylation, which helps overcome the fundamental hurdle of homogeneously catalyzed processes, namely the separation of catalyst and product.[18] Solvents have also been reported to affect the activity and selectivity of certain heterogeneously catalyzed hydrogenations,[19-25] oxidations,[26-30] and electrochemical reactions.[31-34] It is now predominantly acknowledged that solvents have pronounced effects on reaction equilibria, reaction pathways, yields, and product selectivity. Therefore, it is no wonder that liquid-phase processing technologies are exceedingly sought after for the heterogeneously catalyzed conversion of highly functionalized lignocellulosic biomass which has the potential to reduce process

cost as well as increase the target product selectivity. To design highly active, selective, and robust catalysts for these processes, there is a critical need to gain a molecular-level understanding of the chemical reactions at the solid-liquid interface. By understanding the role of the solvent for surface catalyzed reactions, solvent properties can be chosen to tailor the catalyst activity and selectivity. This process of "solvent engineering" could lead to the design of more selective and less energy intensive processes for challenging chemical transformations such as the conversion of biomass. Despite considerable progress in our understanding of the stability and the surface properties of metal-supported nanoparticles in gas phase environments, the effect of a liquid phase is less investigated and not well understood, partly due to the limited availability of experimental (*in situ* and *in operando*)[28,35-38] and theoretical studies,[25,30,39-41] and partly due to the added complexity of a reaction system containing both a complex heterogeneous catalyst and a condensed phase.

Including the effect of a liquid phase environment to chemical reactions occurring at solid-liquid interfaces is an intricate challenge in computational chemistry due to the enormity of the tasks in hand, viz., (1) an all-atomistic quantum mechanical description of the chemically relevant part of the system involving all the atoms and their immediate neighborhood relevant to the bond breaking and forming processes, (2) computation of partition functions in condensed phase systems where the harmonic approximation[42] is no longer valid, which requires an extensive phase space sampling on a high dimensional potential energy surface, and (3) a sufficiently large computational model system that adequately describes the long ranged electrostatic interactions between solute and solvent molecules, the non-harmonic dynamic fluctuations of the complex liquid phase, and can

circumvent the pitfalls of finite-size effects.[43-44] While 'on the fly' electronic structure calculations in brute force ab initio molecular dynamics (AIMD) simulations[45-47] have been employed lately to present some thought-provoking results,[30,48-49] the massive computational cost associated with it constrains both the size of the simulation system (a few hundred atoms) and the time scale of simulation (a few picoseconds).[50-52] An alternative approach is to use continuum solvation models, where the solvent is replaced by a continuum with an appropriate dielectric constant and the solute is placed in cavities constructed within this continuum.[53] Although continuum solvation models provide a much faster way to approximate free energies of reaction in solution, they perform poorly for describing the anisotropic site-specific interactions between solute and solvent molecules.[54] The need for an accurate description of the potential energy surface (level of theory), statistically relevant portrayal of the phase space, and adequate model system-size, all the while keeping the computational cost affordable can be realized by employing multilevel quantum mechanical/molecular mechanical (QM/MM) methods.[55-57] In this class of methods, the active site and the immediate reaction environment are treated from first-principles while the nonreactive part of the system and the bulk of the solvent medium are treated using a classical molecular mechanical level of theory. We have previously developed such a hybrid QM/MM model dubbed as Explicit Solvation model for Metal Surfaces (eSMS)[58] for describing heterogeneously catalyzed reactions at solid-liquid interfaces and applied it to describe aqueous phase effects on the C-C bond cleavage of a double-dehydrogenated ethylene glycol moiety on Pt(111).

At first glance, the use of molecular dynamics (MD) simulations in hybrid QM/MM models for equilibrium phase space sampling and computation of a potential of

mean force appears trivial. The solute of interest surrounded by some number of solvent molecules is equilibrated with respect to an initial configuration, and dependent on the correlation time of the solvent molecules, the phase space is sampled by collecting assorted snapshots from the MD trajectories. The so-called 'equilibration' stage ensures that by the end of this stage the system is sampling from a proper thermodynamic ensemble, i.e., the averages and probability of localized fluctuations of thermodynamic properties follows statistical equilibrium rules. However, the significant computational effort needed for phase space sampling, paired with the requirement for results converged to the appropriate level of accuracy to answer the problem at hand, leads to a desire to identify *a priori* the required timescale for the equilibration and sampling phase of the MD simulations. This knowledge is particularly relevant also if a high level of theory such as DFT is needed to describe the entire simulation system, instead of a QM/MM level of theory. Only with such knowledge can we estimate whether enough computational resources are available for a given level of theory. Next, finite size effects are ubiquitous in many simulation phenomena.[59-60] For example, ensemble size effects[61-62] that arise from a too small number of particles in a simulation system and implicit or anomalous size effects[59,63-64] that can originate from an artificial stabilization of the system due to imposing an infinite periodicity are common challenges. Thus, for practical computations of solvation effects in heterogeneous catalysis, it is essential to possess a knowledge of a characteristic system size required for converged simulation results.

In a previous study, we performed a detailed first-principles vapor and aqueous phase (implicit solvation) investigation of ethylene glycol (EG) reforming over a Pt(111) model surface.[65] Our calculations suggested the primary O-H scission and the subsequent

α-H abstraction to be the key rate controlling steps over a wide range of temperatures (373-673 K). We then employed our QM/MM minimum free energy path (QM/MM-MFEP) methodology to calculate the aqueous phase effects on the above-mentioned bond cleavages (without optimization in aqueous phase).[54] Our results indicated that the aqueous phase has a much larger effect on the free energy of reaction and the free energy of activation of O-H splitting compared to that of C-H splitting. In this study, using the O-H splitting of ethylene glycol as a case study, we first identify convergence criteria for our QM/MM calculations, namely, the required timescale for equilibration, the required amount of phase space sampling, and the number of solvent molecules to be included in the simulation to accurately represent the physical system. Next, we investigate the initial O-H, C-H and C-OH bond dissociations in liquid water over Pt(111) using our QM/MM-FEP methodology with two different Pt-water force fields (Spohr-Heinzinger[66] and Metal potential[67]) and various implicit solvation methods.[53,68-70] Although the C-OH bond cleavage was not identified by our implicit solvation study to be rate controlling, understanding solvation effects for C-OH bond cleavages is similarly essential to C-H and O-H bond cleavages for catalytic biomass processing.

In contrast to our previous study, all reactants, products, and transition states for the above-mentioned reactions are optimized in the aqueous reaction environment. The results of these calculations suggest that aqueous phase effects are small (< 0.1 eV) for the C-H bond cleavage and the activation barrier of the C-OH bond cleavage while they are large (> 0.35 eV) for the O-H bond cleavage and the reaction free energy of the C-OH bond scission. While the choice of a different Pt-water force field can lead to differences in predicted solvation effects of up to 0.2 eV, the differences are usually much smaller (<

0.1 eV) and the trends are always the same. In contrast, implicit solvation methods appear to currently not be able to reliably describe these solvation effects for metal surfaces even qualitatively.

3.3 Computational Details

3.3.1 Planewave DFT Calculations

Vapor phase DFT calculations were carried out by employing periodic boundary conditions as implemented in the Vienna Ab Initio Simulation Package (VASP 5.4).[71-72] A frozen-core, all-electron projector augmented-wave (PAW)[73] method was utilized to avoid the singularities of Kohn-Sham wavefunctions at the nuclear positions. The number of valence electrons considered for Pt, C, O, and H are 10 ($5d^9 6s^1$), 4 ($2s^2 2p^2$), 6 ($2s^2 2p^4$), and 1($1s^1$), respectively. The purely quantum mechanical phenomena of electron exchange and correlation effects were accounted for by using the Perdew-Burke-Ernzerhof (PBE)[74-75] functional within the semi-local generalized gradient approximation.[76] Brillouin zone integrations have been performed with a 4×4×1 Monkhorst-Pack[77] k-point grid and electronic wavefunctions at each k-point were expanded using a discrete plane-wave basis set with kinetic energies limited to 400 eV. Due to the partial filling of bands for the metallic Pt, a first order smearing method (Methfessel-Paxton)[78] with 0.10 eV smearing width was employed, which allowed us to calculate the entropic contributions due to the smearing very accurately. Dipole and quadrupole corrections (along the surface normal) to the total energy have been calculated using a modified version of the Makov-Payne[79] method and Harris corrections, based on the non-self-consistent Harris-Foulkes[80-81] functional, have been applied to the

stress-tensor and forces. A 4×4-unit cell with four layers of metal atoms (bottom two layers fixed in their bulk positions) has been employed to mimic the Pt(111) model surface in the vapor phase. The interaction between the periodic images along the surface normal has been curtailed by introducing a 15 Å vacuum on top of the surface. The self-consistent field (SCF) convergence criterion for the electronic degrees of freedom of the valence electrons was set to 1.0×10^{-7} eV. Transition state structures for the elementary processes were located using a combination of climbing-image nudged elastic band[82-83] and dimer[84-85] methods. Finally, the minima and the first order saddle points were validated by computing the Hessian matrix and vibrational spectra.

3.3.2 Non-periodic cluster calculations

Cluster model DFT calculations in vacuum have been carried out using the TURBOMOLE 7.2 program package.[86-88] Two layers of Pt atoms with a hexagonal shaped geometry (51 atoms) were chosen to model the Pt(111) cluster surfaces. The convergence of the total QM/MM energy with respect to the lateral size and depth of the cluster geometry can be found elsewhere.[58] An improved version of the default TURBOMOLE basis sets (def-bases) with split valence and polarization functions (def2-SVP)[89-90] were employed to represent the adsorbate atoms. Pt atoms were represented using scalar relativistic effective core potentials (ECPs) in conjunction with split valence basis sets augmented by polarization functions.[90-91] Electron exchange and correlation effects were accounted for by employing the PBE functional.[74-75] To speed up the calculation as recommended by TURBOMOLE, the RI-J approximation with auxiliary basis sets was used to approximate the coulomb integrals.[92-93] An SCF convergence

criterion of 1.0×10^{-7} Hartree was established and a Gauss-Chebyshev type spherical grid, m4, was employed to perform the numerical integrations.[87]

3.3.3 Molecular Dynamics (MD) Simulations

MD simulations were carried out using the DL_POLY 4.03 molecular simulation program package.[94] The initial 4×4 Pt(111) unit cell was augmented laterally to a 16×20 surface with further vacuum added in the Z-direction resulting in a 45.0 Å × 48.7 Å × 49.0 Å simulation box comprising of 1280 Pt atoms. The simulation box height was selected based on the work from Behler et al.[95] who found that simulations of metal-water interfaces should contain a water layer of ~40 Å height. The experimental saturated liquid water density of ~0.8 g/cm^3 at 500 K was achieved by packing the simulation box with 2200 water molecules. All metal and adsorbate atoms were kept fixed while the geometry of water molecules was constricted to that of TIP3P[96] geometry with the RATTLE algorithm,[97] a velocity version of the SHAKE algorithm,[98] in conjunction with the velocity Verlet (VV) integrator[99] to solve the Newton's equations of motion. The TIP3P model was employed for the force field parameters of liquid water while the van der Waals parameters for adsorbate atoms were obtained from the OPLS force field.[100-101] In addition to the OPLS parameters, the Lennard-Jones parameters from the CHARMM all-atom force field[102] were used for the hydrogen atoms of the adsorbed moieties. Lennard-Jones parameters for hydrogen atoms are important in QM/MM optimizations that permit hydrogen atoms to approach water molecules and leave the protective environment of a neighboring carbon or oxygen atom. Both the Spohr-Heinzinger (SH)[66] and Metal potential[67] were employed to describe the Pt-water interaction. However, only the SH potential was utilized for the optimization of the adsorbed species in liquid water,

because this potential has recently been found to give a better description of the water-Pt(111) interaction compared to that of the Metal potential.[103] The charges for the QM atoms were estimated using the natural population analysis (NPA).[104] To describe the interaction of the TIP3P water point charges with the quantum chemically described cluster model, we employed the periodic electrostatic embedded cluster method (PEECM)[105] as implemented in TURBOMOLE. Simulations were carried out in a canonical ensemble (NVT) with Nosé-Hoover thermostat.[106-107] A 1 ps relaxation time constant for temperature fluctuations was used to maintain the average system temperature. Electrostatic interactions were accounted for by using the Smoothed Particle Mesh Ewald (SPME) method[108] with automatic parameter optimization for default SPME precision and a 12 Å cutoff radius was adopted for the van der Waals interactions and the transition between short and long range electrostatic interactions. If not specified differently, all systems were equilibrated for 250 ps and sampled for 725 ps using a 1 fs timestep. To optimize structures in an aqueous reaction environment, we utilized the fixed-size ensemble approximation with 10,000 MM conformations recorded every 50 fs. The time interval for recording structures is based on a recent study of liquid water by Cowan et al.[109] who concluded that "liquid water essentially loses the memory of persistent correlations in its structure within 50 fs".

3.3.4 QM/MM Energy Calculation

A QM/MM minimum free energy path (QM/MM-MFEP)[56-57] method for optimizing the intrinsic reaction coordinate on a potential of mean force (PMF) description of the reaction system has been implemented in our program packages. A full description of this methodology, eSMS (Explicit Solvation for Metal Surfaces) can be

found elsewhere.[58] Free energy calculations require energy evaluation from uncorrelated measurements of the system and ideally the energy estimator should also be capable of minimizing the statistical bias and variance of the free energy differences of the physical system being studied. Exponential averaging (EXP), also known as the Zwanzig relationship[110] has long been applied to study a variety of problems such as amino acid recognition,[111] RAS-RAF binding affinity,[112] and octanol/water partition coefficients,[113] etc. However, the EXP has been shown to represent poor efficiency and phase space overlap,[114-115] and also is largely dependent on the distribution of the QM/MM energy.[116] Here, we employed the Bennett acceptance ratio (BAR)[117] as the free energy estimator which uses both the forward and reverse distributions simultaneously in a more efficient way than simply averaging the forward and reverse exponential estimators. BAR has been demonstrated to be advantageous in practical atomistic simulations as it displays a lower bias and variance of the free energy estimates when compared to EXP and thermodynamic integration (TI).[114,118] Finally, the whole free energy estimation procedure has been repeated three times to establish 95% confidence intervals for evaluating the free energy of reaction and free energy of activation, assuming a normal distribution.[119] All uncertainties reported in this study are 95% confidence intervals.

3.3.5 Periodic Implicit Solvation Calculations

In addition to implicit solvation calculations performed with the iSMS method,[41] we performed implicit solvation calculations at 500 K using VASPsol[69-70] with a relative permittivity of water of 30.55 at reaction conditions.[120] We used the default values for the parameter n_C that defines the value at which the dielectric cavity forms and for the width of the diffuse cavity, σ .[69] We also employed the default effective surface tension

parameter, τ , for describing the cavitation, dispersion, and repulsive interaction between the solute and the solvent that are not captured by the electrostatic terms.[69] While this parameter is likely most accurate only for simulations at 298 K and not at 500 K, it is an optimized parameter of the solvent model that cannot easily be obtained at other temperatures. Due to the absence of adequate experimental solvation data at 500 K, we decided that the default parameter is likely most meaningful. All other computational details for periodic implicit solvation calculations were kept the same as in our periodic vapor phase calculations.

3.4 Results and Discussion

The bidentate binding mode of ethylene glycol on the Pt(111) surface in vapor phase (adsorption through hydroxyl groups and formation of intramolecular hydrogen bonds due to the directionality of the hydroxyl groups, Figure B.1a) makes the direct C-C and C-O bond cleavages energetically unfavorable with a high activation barrier of 2.07 eV and 2.09 eV, respectively. In the vapor phase, the initial hydrogen abstraction from the hydroxyl group to form an alkoxide intermediate is thermodynamically unfavorable ($\Delta E_{rxn} = +0.40\ eV$) compared to the dehydrogenation of ethylene glycol to form 1,2-dihydroxyethyl ($\Delta E_{rxn} = -0.48\ eV$). However, due to the close proximity of the H atom of the hydroxyl group to the surface and the required rotation of the second hydroxyl group away from the surface for the C-H scission, the O-H bond cleavage is slightly more energetically favorable.[54,65] The choice of the O-H bond scission reaction to establish the characteristic parameters for a well-converged QM/MM calculation has been motivated by the fact that the activation barrier is neither too high to make the FEP procedure computationally prohibitive, nor too low to make the PMF procedure ill-founded and the

characterization of the aqueous phase effect extremely problematic. We have recently demonstrated that in an aqueous reaction environment, the entropy-enthalpy compensation plays a major role in facilitating the O-H bond scission on hydrophobic interfaces and exhibits a substantial solvent effect on the free energy of reaction and free energy of activation, which makes this model reaction all the more compelling for determining characteristic parameters for explicit solvation calcualtions.[54]

3.4.1 Timescale for equilibration

Conventional approaches for achieving a thermal equilibrium in an MD simulation involve an equilibration stage. Although the timescale for the equilibration period is dependent on the initial phase space point and can be determined from the relaxation time of various properties and a normal distribution of their fluctuations; in practice, it is difficult to determine the slowest time scale of the simulation system and the equilibration time scale is often determined by computational affordability (even if it risks biasing the simulation result) and therefore, varies wildly from 300 fs in AIMD simulations[121] to 10 ps in QM/MM simulations[122] and 2 ns in combined DFT-MD[123-124] investigations that use a classical force field for the equilibration stage.

Figure B.4a illustrates the total energy and Figure B.4b depicts the root mean square fluctuations (RMSF) of the potential energy during a 975 ps MD simulation of ethylene glycol solvated by 2200 water molecules, thermally coupling all the atoms to a Nosé-Hoover heat bath at 500 K. While the total energy graph might suggest that an equilibrated state has been obtained after ~4 ps, the RMSF appears to be converged only after ~200 ps. In order to quantify the timescale required for equilibration to predict

aqueous phase effects on a surface catalyzed reaction with greater certainty, we performed QM/MM free energy perturbation calculations with three distinct equilibration periods of 50 ps, 100 ps, and 250 ps. For each equilibration timescale, we explored the equilibrium phase space for 150 ps (1000 MM conformations 150 fs apart) with 3 independent MD simulations. We employed BAR as the free energy estimator for each individual trajectory and computed 95% confidence intervals from the 3 independent observations. Figure 3.1 and Table B.1 display the variability in the estimation of the free energy of reaction and free energy of activation for our model reaction. Our calculations indicate that all equilibration stages lead overlapping error bars and approximately the same estimation of the free energy of reaction and activation ($\Delta G_{rxn} \approx -0.09\ eV, \Delta G^{\dagger} \approx 0.11$ eV). Also, predicted error bars are smaller than 0.06 eV and therefore well within the inherent error of density functional theory calculations.[125] Although the error bars are slightly larger for the simulations with the longest equilibration stage, we use in the following a 250 ps equilibration period for calculating aqueous phase effects on the free energies of surface catalyzed reactions. Our selection is motivated by the high degree of the RMSF in the potential energy at and below 100 ps (Figure B.4b), the fact that we do not possess estimates of the error bar of our error bars, and that we show in the next section that typical rotational water correlation times near our adsorbate are on the order of ~40 ps.

3.4.2 Configuration space sampling

An overarching theme in the calculation of liquid phase effects on free energies of elementary processes is the calculation of ensemble averages.[116,126] To calculate a reliable estimate of an ensemble average, the potential energy surface has to be adequately

sampled for all the relevant configurations of the system. However, the sheer size of the configuration space originating from the sizable number of solvent molecules included in the simulation box makes extensive exploration of the configuration space extremely challenging. Owing to a lack of consensus on how much sampling of the configurational space is sufficient for a solvated adsorbed carbohydrate species on a metal surface for an error smaller than 0.1 eV, we computed the average rotational correlation time for water molecules in close proximity (up to 5 Å) to adsorbed ethylene glycol on Pt(111) and performed QM/MM-MFEP calculations for our test reaction with ensemble averages calculated from 100, 500, and 1000 MM conformations that are 150 fs apart (i.e., sampling for 15 to 150 ps). Figure B.5 illustrates a three-exponential fit to the rotational correlation time of water molecules in close proximity to the adsorbate. The average rotational correlation lifetime is computed to be ~40 ps. This result agrees with both the correlation time of hydrogen bonds between a water layer and a hydrocarbon species adsorbed on Pt(111) and the hydrogen bond correlation time of a water layer on various Cu surfaces, all of which have been determined to be between 1 and 10 ps.[95,124] For the free energy calculations, the procedure was repeated 3 times with independent MD trajectories to establish the confidence interval estimates of the free energy of reaction (Figure 3.2a) and the free energy of activation (Figure 3.2b). Independent trajectories are obtained from trajectories separated by at least 125 ps which is significantly larger than the correlation times discussed above. As illustrated in the Figure 3.2, the uncertainty in the calculation of free energies are statistically indistinguishable (see also Table B.2). To err on the side of caution and sample for at least three times the correlation lifetime of water molecule rotations, we employed 1000 MM conformations for all subsequent free

energy calculations (sampling of 150 ps). A repetition of the simulations and computation of confidence intervals was found essential since the fluctuations of a single potential of mean force calculation were often significant as evidenced by 95% confidence intervals of up to 0.1 eV from 3 measurements. The significant fluctuations of a single potential of mean force calculation originate from both the limited phase space sampling and from the use of the fixed charge approximation used in the QM/MM-FEP methodology. We note that each FEP calculation requires one to compute the ESP charges on the QM atoms as a mean field of the electrostatic potential of 100 MM conformations. By repeating the calculations 3 times, we both increase our total configuration space sampling and obtain simulation results for 3 slightly different ESP charges on the QM atoms, overall improving the reliability of our predictions.

3.4.3 System-size effects

The infinite periodicity of a computational simulation system makes it less susceptible to finite-size effects when compared to non-periodic system simulations. However, a periodic system with a small simulation box tends to show crystal-like long-range order while an unnecessarily large simulation system might result in wasted computational resources without adding any germane information needed to describe the physical system.[127] To explore the effect of the system size on the solvent effect on free energies of our model reaction, we constructed four different simulation boxes by changing the lateral box size while maintaining a constant liquid height (49.0 Å) to keep the system pressure and density constant. In decreasing order, the lateral dimensions of the simulation boxes are $45.0\ \text{Å} \times 49.0\ \text{Å}$, $45.0\ \text{Å} \times 39.0\ \text{Å}$, $33.7\ \text{Å} \times 39.0\ \text{Å}$, and $33.7\ \text{Å} \times 29.2\ \text{Å}$, which corresponds to solvating the metal surface and adsorbate by

2200, 1760, 1320, and 990 water molecules. We note that we refrained from decreasing the box size below this point since it would result in a simulation box with the smallest dimension being less than twice the cutoff employed for calculating vdW interactions.

As shown in Figure 3.3, there is no statistically significant difference in the predicted free energies and we conclude that even our smallest simulation box is likely sufficiently large for our free energy calculations. Nevertheless, we use in the following our simulation box containing ~2200 water molecules. While for our eSMS solvation model, the length scales of relevance are not computationally prohibitive, for a full quantum chemical description of the potential energy surface it is interesting that correlation lengths appear to be smaller than 15 Å (half the shortest simulation box length).

3.4.4 Optimization of adsorbed moieties

Vapor phase optimized structures were employed as the initial configuration for the optimization of reactants, transition states, and product states of the O-H, C-OH, and C-H bond cleavages of ethylene glycol in aqueous phase. Each optimization cycle consisted of a 750 ps MD simulation with 250 ps of equilibration stage and 500 ps of equilibrium configuration space sampling. Geometries were then optimized in a fixed size ensemble of 10,000 MM conformations recorded at 50 fs intervals with a force-based convergence criterion of 1.0×10^{-3} au/atom. The optimized QM structure was then employed for the generation of a new ensemble of MM conformations and the whole procedure was repeated until the QM/MM energy was converged.

Generally, the aqueous phase appears to have only a minor effect on the reactant ($\Delta A_{RS} = -0.06 \pm 0.01\ eV$), product ($\Delta A_{PS} = -0.10 \pm 0.01\ eV$) and transition state ($\Delta A_{TS} = 0.03 \pm 0.01\ eV$) relaxations for the O-H bond cleavage. In the reactant state, going from the vapor (Figure B.1a) to an aqueous phase (Figure B.1b), the Pt-O bond length increases by 0.10 Å. Similarly, the product state (Figure B.1e & B.1f) is pushed upwards into the aqueous phase and the Pt-O bond length increases by 0.78 Å. Considering the hydrophobicity of the Pt(111) surface,[128] this places the adsorbed moiety in the immediate vicinity of the first layer of the water molecules (Figure B.6), leading to many hydrogen bonding arrangements plausible with the neighboring water molecules which results in a slightly stabilized reactant and product state. Additionally, for the reactant state, the distance between the hydrogen atom (H_2) of the non-reacting hydroxyl group and the oxygen atom of the reacting hydroxyl group (O_1) decreases by 0.18 Å, making intra-molecular hydrogen bonding more probable. The transition state does not show a significant change (less than 0.02 Å) in H_2-O_1 distance and the Pt-O bond length; only the transition state bond length gets reduced by 0.18 Å when going from the vapor to an aqueous phase.

Figure B.2 and B.3 illustrate the corresponding effect of an aqueous phase on the structure of various states in the C-H and C-OH bond cleavage reactions. Similar to the O-H bond cleavage, the transition state and the product state moieties of the C-OH bond cleavage reaction move upwards, going from vapor to aqueous phase, which explains their stabilization in an aqueous phase ($\Delta A_{TS} = -0.09 \pm 0.01\ eV, \Delta A_{PS} = -0.03 \pm 0.01\ eV$). The transition state bond length also increases by 0.10 Å due to the presence of an aqueous phase. Unlike the O-H and C-OH bond cleavages, the aqueous phase has

no perceptible effect on the transition state and the product state of the C-H bond cleavage ($\Delta A_{TS} = 0.06 \pm 0.01\ eV, \Delta A_{PS} = 0.01 \pm 0.01\ eV$). Except for a minimal rotational change, both the transition state and the product state of the C-H bond cleavage largely remain unaffected by the presence of an aqueous phase, resulting in a nominal solvent effect. The transition state bond length also remains largely unaltered (less than 0.02 Å) going from vapor to an aqueous phase.

3.4.5 Free energy profile

Figures 3.4-3.6 illustrate the free energy (potential of mean force) profiles for the O-H, C-H and C-OH bond cleavages, respectively. For the O-H and C-H bond cleavages, we presented previously[54] similar profiles without the optimization of the critical points in aqueous phase and without vdW parameters for hydrogen atoms of the adsorbate molecules that are only needed for an optimization. To establish adequate phase space overlap throughout the reaction coordinate, we introduced 41 intermediate states between the reactant and transition state, and 19 intermediate states between the transition state and the product state for the O-H cleavage reaction (Figure 3.4). The number of windows is determined by our desire to have an energy difference between windows smaller than twice the thermal energy($< 2\ k_B T$). Similarly, the free energy profile for the C-H cleavage reaction (Figure 3.5) has been constructed by inserting 26 intermediate states between the reactant and transition state, and 29 intermediate images between the transition state and the product state. Finally, the potential of mean force profile for the C-OH bond cleavage (Figure 3.6) has been constructed by inserting 72 intermediate states between the reactant and transition state, and 66 intermediate images between the

transition state and the product state. A summary of our calculation results is shown in Table 3.1 and Figure 3.7.

Figure 3.7 illustrates that the aqueous phase has a much larger effect on the O-H bond scission than on the C-H and C-OH bond scissions of ethylene glycol. The free energy of reaction of the C-OH bond scission is also significantly affected by the aqueous environment. These observations can be understood by the structural changes along the reaction coordinate in each of the above-mentioned reactions. The presence of liquid water and formation of hydrogen bonds between the adsorbate and the surrounding water weakens the intramolecular hydrogen bonding (increase in distance between OH groups) for the reactant, transition state, and product state of the C-H bond cleavage. The C-H bond scission also exposes a C atom to the neighboring aqueous phase environment which is unable to form hydrogen bonds with the water molecules. As a result, the aqueous phase has only a very minor effect on the net hydrogen bonding along the reaction coordinate and solvation effects are small and within the accuracy of our calculations. In contrast, the O-H bond cleavage exposes a highly electronegative O atom ($O^{\delta-} = -0.74\, e^{-}$) to the surrounding environment which is able to accept hydrogen bonds from the hydrogen atoms of the water molecules, changing the hydrogen bonding energy contribution along the reaction coordinate, and resulting in a sizable exergonic solvation effect on the free energy of reaction and free energy of activation.

The presence of an aqueous phase has a significant endergonic effect on the thermodynamics of the C-OH bond cleavage while the kinetics of the reaction remains unaffected. Figure B.7 shows a snapshot of the distribution of water molecules on top of the Pt(111) surface for the reactant, transition state, and product state of C-OH bond

cleavage of ethylene glycol. In the reactant state (Figure B.7a) the adsorbed species (ethylene glycol) is immersed in the first layer of water molecules. However, in the product state (Figure B.7c), the cleaved OH species lies beneath the layer of water molecules, which reduces the number of hydrogen bonding arrangements for the adsorbed moiety, resulting in an endergonic effect on the thermodynamics of the reaction. Unlike the O-H bond scission, the C-OH bond scission exposes a C atom to the surrounding aqueous phase environment which is unable to form hydrogen bonds with water molecules, leading to a nominal aqueous phase effect on the kinetics of this reaction. Michel and coworkers have recently claimed that C-OH bond cleavages are promoted by the explicit presence of a water molecule (microsolvation[129-131] approach).[132] While the inclusion of water coordinates in the reaction coordinate can indeed lead to a lower activation barrier that is currently not considered in our simulations, the microsolvation approach does not sample the configuration space and therefore neglects any temperature dependent entropic cost associated with placing a water molecule at a specific location.

3.4.6 Comparison of metal-water interaction potentials

The predictive power of any solvation approaches that uses classical molecular mechanics simulations suffer from a fundamental issue; the accuracy and transferability of force fields.[103,133-134] To compare how the metal-water interaction potentials affect the reaction thermodynamics and kinetics, we have performed our QM/MM FEP calculations for the O-H, C-H, and C-OH bond cleavages of ethylene glycol with two different force field parameters; the Spohr-Heinzinger (SH) potential[66] and Lennard-Jones (LJ) potential.[67] Figure B.6 illustrates the distance distribution of water O atoms over a

Pt(111) surface using the above-mentioned metal-water interaction potentials. The LJ potential predicts a higher density of water molecules closer to the surface compared to the SH potential. Also, the highest water density is by ~0.1 Å closer to the surface for the LJ potential, although some water molecules move slightly closer to the surface for the SH potential.

Table 3.1 and Figure 3.7 show the effect of these potentials on the thermodynamics and kinetics of our test reactions. The aqueous phase exerts an endergonic effect on the thermodynamics of the C-OH bond cleavage of ethylene glycol. While both the LJ and SH potentials predict only a nominal effect on the free energy of activation, the LJ potential predicts a less endergonic effect on the free energy of reaction ($\Delta G_{rxn}^{LJ} = 0.49 \pm 0.02\ eV$) compared to that of the SH potential ($\Delta G_{rxn}^{SH} = 0.57 \pm 0.02\ eV$). This phenomenon can likely be explained by the LJ potential having a higher water density closer to the surface (Figure B.6), being able to at least somewhat stabilize the surface OH group in the product state (see Figure B.7). Next, for the C-H bond cleavage, both Pt-water potentials predict similarly small solvation effects with the LJ potential predicting a minimally larger effect on the activation and reaction free energies. Finally, the LJ potential shows a less exergonic effect on the O-H bond scission of ethylene glycol compared to the SH potential. For the O-H cleavage of ethylene glycol, all stationary points are submerged in the surface water layer such that the effect of Pt-water potential originates likely from the difference in water density adjacent to the surface (Figure B.6). While both potentials suggest that O-H bond dissociation is significantly accelerated and more exergonic in liquid water, intricacies of the potential lead to free energy predictions deviating by as much as 0.2 eV. Given the large solvation

effects for O-H bond dissociations, it appears that a more accurate/reliable Pt-water potential is required to predict solvation effects for O-H bond cleavage with an accuracy comparable to DFT.

3.4.7 Comparison between implicit and explicit solvation methods

Finally, we compare our explicit solvation results to implicit solvation calculations performed with VASPsol[69-70] and our iSMS methodology.[41] Both implicit solvation models (iSMS and VASPsol) fail to capture the full solvent stabilization during the O-H cleavage of ethylene glycol (see Table 3.1 and Figure 3.7). However, VASPsol predicts even an endergonic effect on both the free energy of reaction and the free energy of activation for this model reaction. This prediction contradicts both of our predictions with iSMS and explicit solvation methodology (and are contradictory to our intuition and experimental studies).[128,135-140] For the C-H bond cleavage, implicit and explicit solvation models anticipate comparable solvent effects which is plausible considering that directional hydrogen bonding contributions do not change significantly along the reaction coordinate for this reaction. Finally, for the C-OH bond cleavage both implicit models do not predict the strong endergonic solvent effect on the reaction thermodynamics of the C-OH bond cleavage that results from the water molecules being unable to fully solvate the surface OH group in the product state. To conclude, the reliability of implicit solvation calculations for heterogeneous (metal) catalysis applications is currently limited (unknown) due to the very limited availability of experimental data that can be used in the parameterization of the implicit solvation models. This is currently a clear advantage of explicit solvation models that rely “only” on a meaningful potential energy description.

3.5 Conclusion

Very little experimental information is currently available to assess the accuracy of various computational approaches for predicting solvation effects on free energies of activation and free energies of reaction for elementary processes on heterogeneous catalysts. As a result, computational models can primarily only be compared against each other and chemical intuition. In principle, the most accurate computational solvation models use an explicit description of the solvent molecules and describe the potential energy surface at a high level of theory. This however requires sufficient configuration space sampling which is usually not affordable for a high level of theory description of the potential energy surface. In this contribution, using the O-H splitting reaction of ethylene glycol over Pt(111) as a case study and characteristic reaction for various biomass platform molecule conversion reactions over noble metal catalysts, we studied the required timescale to reach thermal equilibrium, the sampling time scale necessary to explore the configuration space, and the size of the simulation system for obtaining reliable and converged free energies of activation and reaction with our eSMS methodology for studying solvation effects in heterogeneous catalysis. Due to the difficulty in determining the correlation time in free energy calculations, we recommend that all explicit solvation calculations be repeated multiple times just as it is common for experiments. Only by repeating simulations at least three times can confidence intervals (resulting from insufficient configuration space sampling and intricacies from our QM/MM-FEP methodology) be estimated. Assuming our test reactions are characteristic for various reactions on metal surfaces, our heuristic recommendations lead to free energies with 95% confidence intervals of < 0.1 eV.

After having established protocols for calculating solvent effects using multiscale models, we calculated solvent effects on the free energy of reaction and free energy of activation for primary dehydrogenation and dehydroxylation reactions of ethylene glycol at the hydroxyl group and α-C. Vapor phase optimized geometries were re-optimized in the aqueous phase environment and vibrational contributions were calculated using numerical gradients and central differences with a 0.02 au step size, assuming non-equilibrium solvation. Our explicit solvation model predicts that aqueous phase effects are small (< 0.1 eV) for the C-H bond cleavage and the activation barrier of the C-OH bond cleavage. In contrast, solvation effects are large (> 0.35 eV) for the O-H bond cleavage and the reaction free energy of the C-OH bond scission. While the choice of a different Pt-water force field can lead to differences in predicted solvation effects of up to 0.2 eV, the differences are usually much smaller (< 0.1 eV) and the trends are always the same. In contrast, implicit solvation models only qualitatively agree with the explicit solvation results for the C-H bond cleavage and they are unable to anticipate the hydrogen bonding stabilization for the O-H and even the C-OH cleavage reactions.

3.6 Acknowledgements

Dr. Michael R. Shirts from the University of Colorado Boulder is gratefully acknowledged for help with the statistical analysis of our results and the implementation of the Bennett Acceptance Ratio (BAR) as the free-energy estimator. This research has been funded by the United States Department of Energy, Office of Basic Energy Sciences (DE-SC0007167). M.Z. acknowledges financial support from the National Science Foundation (OIA-1632824). Computing resources provided by the National Energy Research Scientific Computing Center (NERSC), Texas Advanced Computing Center

(TACC), and Pacific Northwest National Laboratory (PNNL) are gratefully acknowledged.

3.7 Tables and Figures

Table 3.1: Aqueous phase effects on the free energy of reaction and the free energy of activation of model reactions of ethylene glycol over Pt(111) at 500 K. QM/MM-FEP calculations describe the solvent effect on the critical points identified by gas-phase calculations while using the gas-phase vibrational partition function for the adsorbed species and transition states. The superscript SH and LJ (SH = Spohr-Heinzinger, LJ = Metal Lennard-Jones) denotes the potential used to describe the metal-water interaction. QM/MM-FEP(OPT) represents the solvent effects for the model reactions (using SH potential) where the respective reactant, transition, and product states have all been optimized in an aqueous-phase environment and the vibrational frequencies are computed in the liquid phase assuming the timescale for re-orientation of solvent molecules is much larger than the timescale for molecular vibrations. Implicit solvation calculations have been performed using both non-periodic (iSMS)[41] and periodic (VASPsol)[69] approaches.

Reaction	Reaction Environment	ΔG_{rxn} (eV)	$\Delta G^{\dagger}$ (eV)
$CH_2OHCH_2OH ** + * \leftrightarrow CH_2OCH_2OH ** + H *$	Vapor phase	0.45	0.70
	iSMS	0.36	0.68
	VASPsol	0.57	0.76
	QM/MM-FEP^{SH}	-0.09±0.06	0.11±0.04
	QM/MM-FEP^{LJ}	0.08±0.02	0.29±0.01
	QM/MM-FEP^{SH}(OPT)	-0.23±0.05	0.21±0.03
$CH_2OHCH_2OH ** + * \leftrightarrow CHOHCH_2OH ** + H *$	Vapor phase	-0.40	0.73
	iSMS	-0.39	0.65
	VASPsol	-0.35	0.59
	QM/MM-FEP^{SH}	-0.38±0.02	0.64±0.02
	QM/MM-FEP^{LJ}	-0.26±0.06	0.56±0.01
	QM/MM-FEP^{SH}(OPT)	-0.36±0.01	0.73±0.02

$CH_2OHCH_2OH ** + *$ $\leftrightarrow CH_2CH_2OH ** + OH *$	Vapor phase	0.26	2.11
	iSMS	0.15	2.04
	VASPsol	0.30	2.04
	QM/MM-FEP^{SH}	0.57±0.02	2.16±0.01
	QM/MM-FEP^{LJ}	0.49±0.02	2.18±0.01
	QM/MM-FEP^{SH}(OPT)	0.64±0.03	2.11±0.03

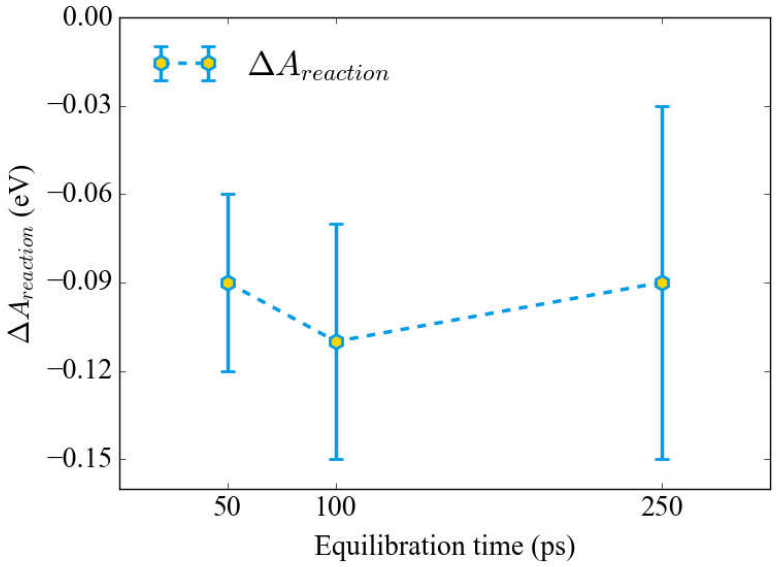

(a)

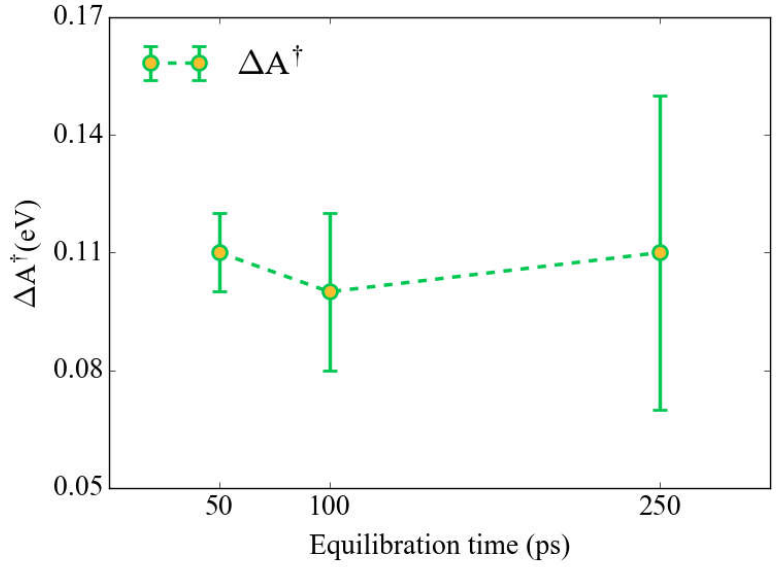

(b)

Figure 3.1: 95% confidence interval estimates of (a) free energy of reaction and the (b) free energy of activation of the O-H bond cleavage of ethylene glycol over a Pt(111) surface at 500 K. Total QM/MM energies have been computed by employing three distinct equilibration times of 50 ps, 100 ps, and 250 ps.

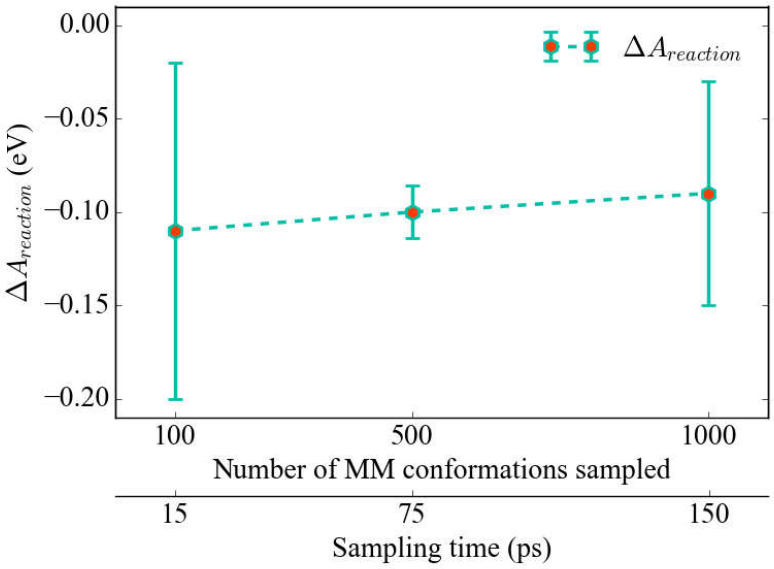

(a)

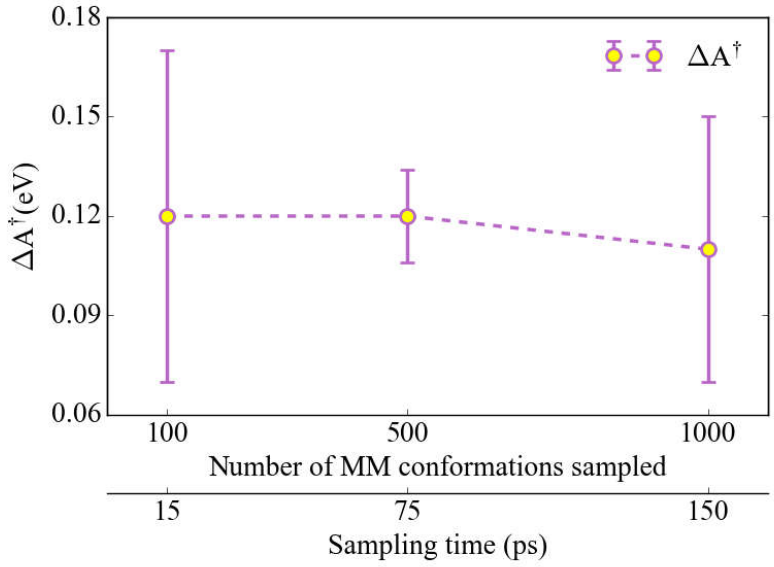

(b)

Figure 3.2: Effect of phase space sampling time on the estimation of (a) free energy of reaction and (b) free energy of activation of the model O-H bond scission reaction of ethylene glycol on a Pt(111) surface at 500 K. The error bars represent the 95% confidence interval estimate of the free energy of the specified reaction.

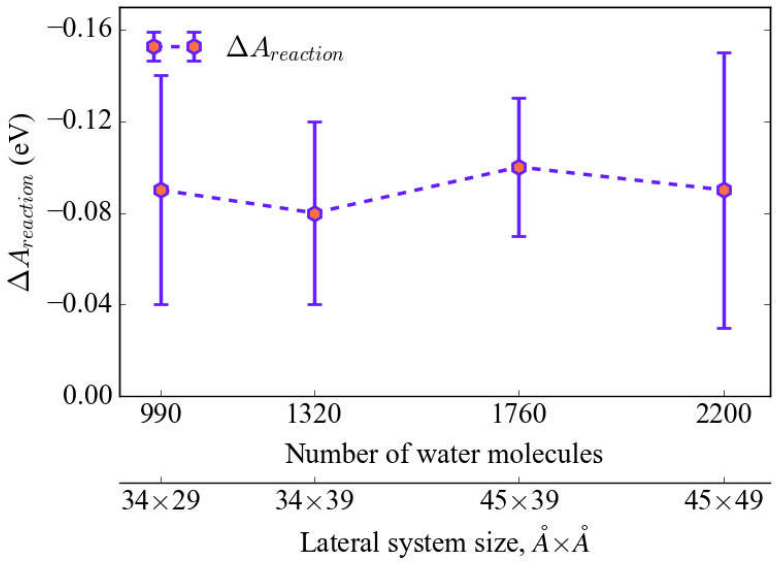

(a)

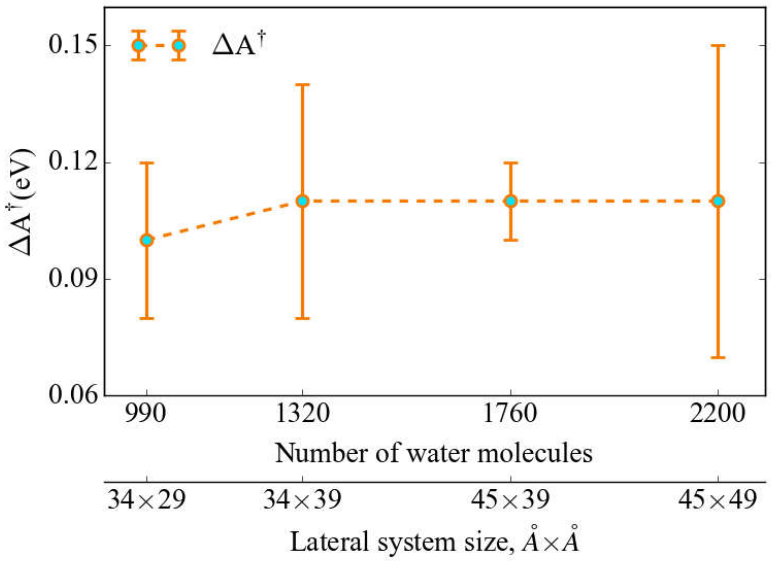

(b)

Figure 3.3: System size effect on (a) free energy of reaction and (b) free energy of activation of the prototypical O-H bond cleavage reaction of ethylene glycol on a Pt(111) model surface at 500K. The error bars represent the 95% confidence interval estimate of the free energy of the specified reaction.

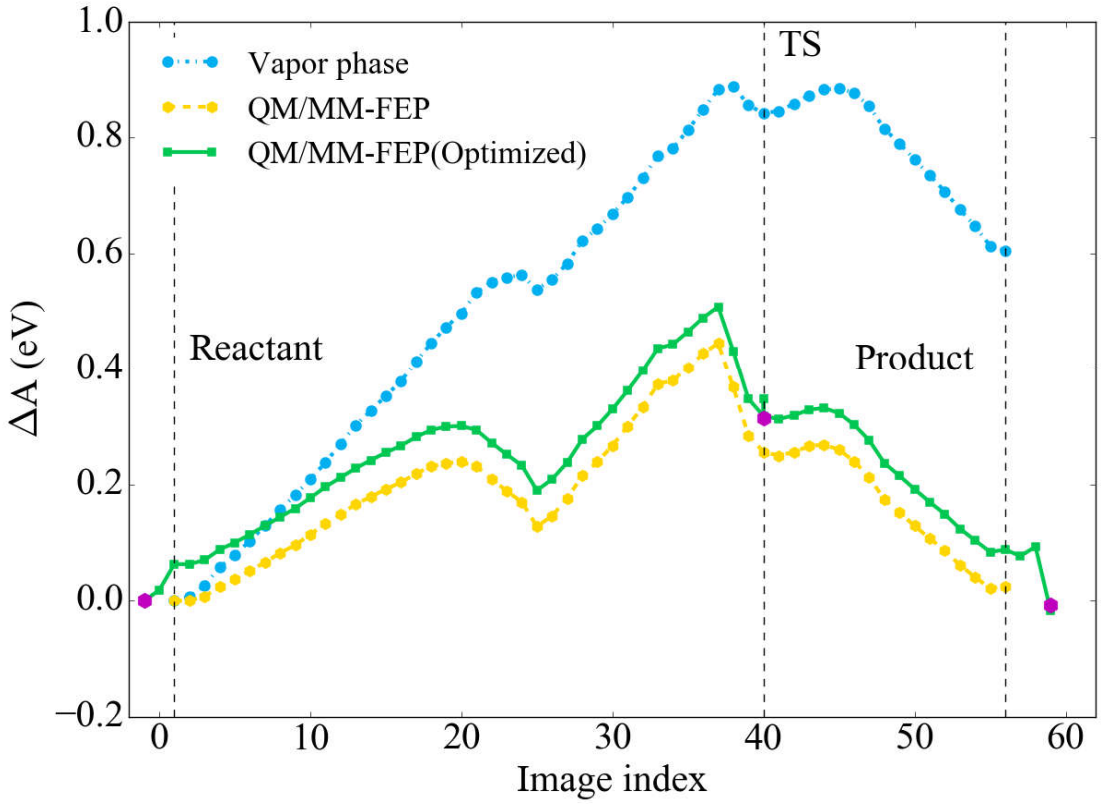

Figure 3.4: Free energy profile for the O-H bond cleavage of ethylene glycol in vapor and aqueous phases on a Pt(111) model surface at 500 K without considering vibrational contributions to the partition function. See Table 3.1 for corresponding data that include vibrational contributions. The points lying on the vertical dashed lines represent the geometries optimized in vapor phase while the magenta dots on the QM/MM-FEP(Optimized) profile represent the aqueous phase optimized structures of the reactant state, transition state, and product state for the O-H bond cleavage. The aqueous phase profiles portray the average of 3 QM/MM-FEP calculations that possess 95% confidence intervals smaller than ±0.1 eV.

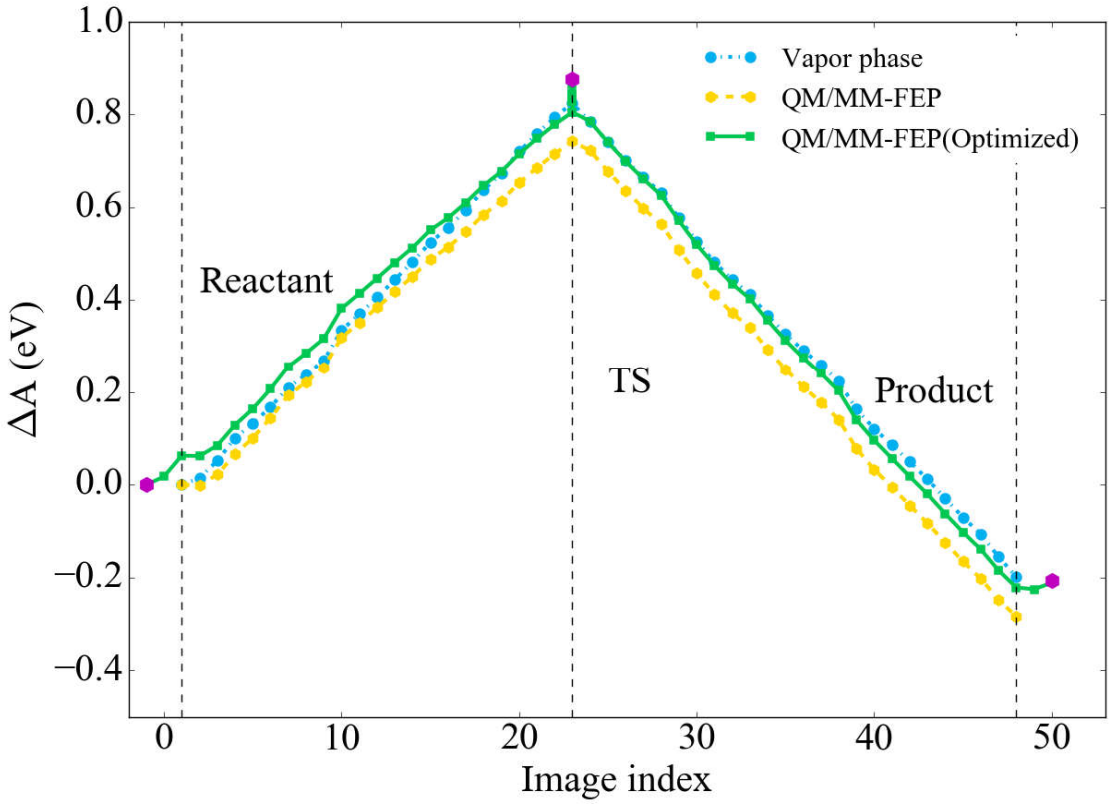

Figure 3.5: Free energy profile for the C-H bond cleavage of ethylene glycol in vapor and aqueous phases on a Pt(111) model surface at 500 K without considering vibrational contributions to the partition function. See Table 3.1 for corresponding data that include vibrational contributions. The points lying on the vertical dashed lines represent the geometries optimized in vapor phase while the magenta dots on the QM/MM-FEP(Optimized) profile represent the aqueous phase optimized structures of the reactant state, transition state, and product state for the C-H bond cleavage. The aqueous phase profiles are the average of 3 QM/MM-FEP calculations that possess 95% confidence intervals smaller than ±0.1 eV.

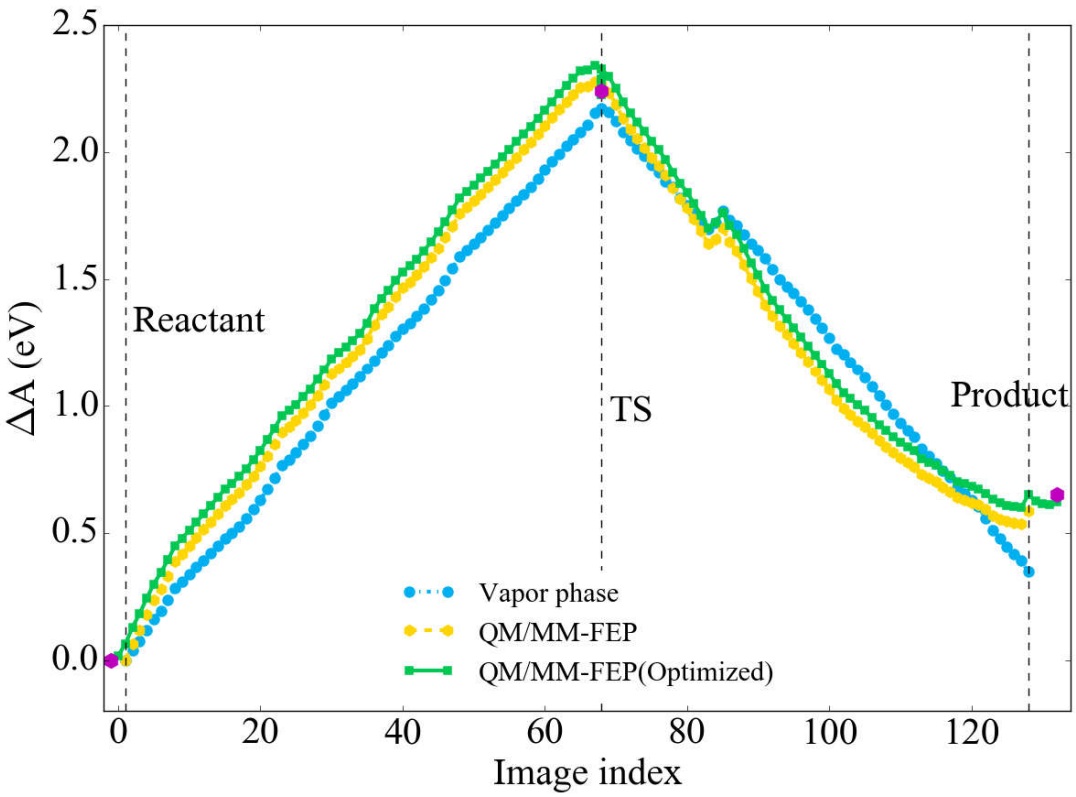

Figure 3.6: Free energy profile for the C-OH bond cleavage of ethylene glycol in vapor and aqueous phases on a Pt(111) model surface at 500 K without considering vibrational contributions to the partition function. See Table 3.1 for corresponding data that include vibrational contributions. The points lying on the vertical dashed lines represent the geometries optimized in vapor phase while the magenta dots on the QM/MM-FEP(Optimized) profile represent the aqueous phase optimized structures of the reactant state, transition state, and product state for the C-OH bond cleavage. The aqueous phase profiles are the average of 3 QM/MM-FEP calculations that possess 95% confidence intervals smaller than ±0.1 eV.

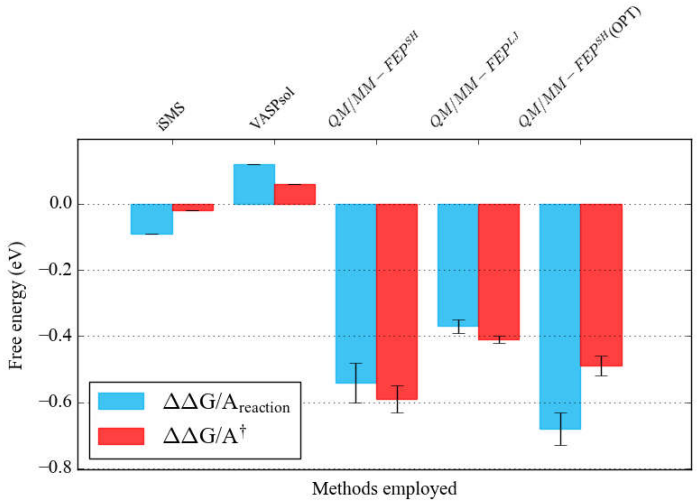
iSMS
VASPsol
QM/MM – FEP^SH
QM/MM – FEP^LJ
QM/MM – FEP^SH(OPT)
0.0
−0.2
−0.4
−0.6
−0.8
Free energy (eV)
ΔΔG/A_reaction
ΔΔG/A†
Methods employed

(a)

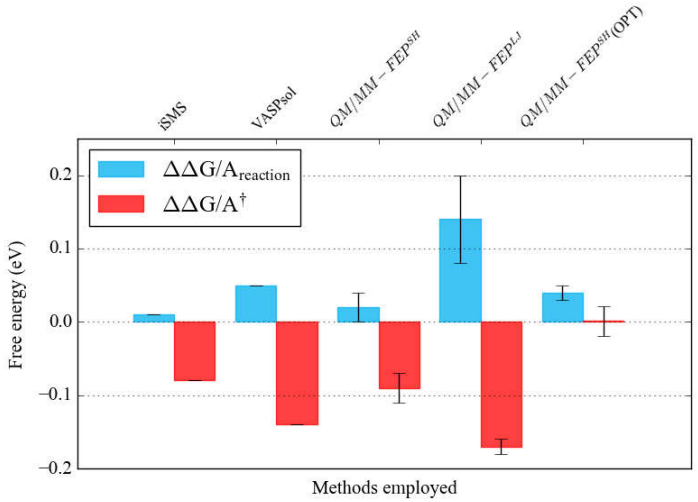
iSMS
VASPsol
QM/MM – FEP^SH
QM/MM – FEP^LJ
QM/MM – FEP^SH(OPT)
0.2
0.1
0.0
−0.1
−0.2
Free energy (eV)
ΔΔG/A_reaction
ΔΔG/A†
Methods employed

(b)

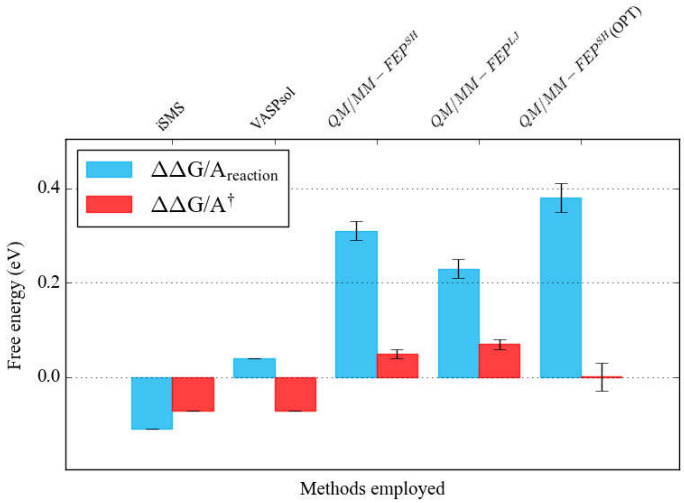

(c)

Figure 3.7: Effect of aqueous phase on the free energy of reaction and activation of a) O-H, b) C-H, and c) C-OH bond cleavages of ethylene glycol over Pt(111) using different implicit and explicit solvation models. Error bars for the explicit solvation models are 95% confidence intervals.

3.8 Bibliography

1. In *Handbook of Solvents* 2nd ed.; Wypych, G., Ed. ChemTec Publishing: Oxford, 2014; Vol. 2, pp 1-261.
2. Claisen, L. Beiträge zur Kenntniss der 1,3 - Diketone und verwandter Verbindungen. *Justus Liebigs Ann Chem* **1896,** *291*, 25-137.
3. Wislicenus, W. Ueber die Isomerie der Formylphenylessigester. *Justus Liebigs Ann Chem* **1896,** *291*, 147-216.
4. Hantzsch, A. Zur Kenntniss der Säureamide. *Justus Liebigs Ann Chem* **1897,** *296*, 84-94.
5. Reichardt, C.; Welton, T. In *Solvents and Solvent Effects in Organic Chemistry*, 4th, updated and enl. ed.; Reichardt, C.; Welton, T., Eds.; Wiley-VCH: Weinheim, Germany, 2011.
6. Menschutkin, N. A. N. Menschutkin. Beiträgen zur Kenntnis der Affinitätskoeffizienten der Alkylhaloide und der organischen Amine. *Z. Physik. Chem.* **1890,** *5*, 589.
7. Knowles, W. S. Asymmetric hydrogenation. *Acc Chem Res* **1983,** *16*, 106-112.
8. Valgimigli, L.; Banks, J. T.; Ingold, K. U.; Lusztyk, J. Kinetic Solvent Effects on Hydroxylic Hydrogen-Atom Abstractions Are Independent of the Nature of the Abstracting Radical - 2 Extreme Tests Using Vitamin-E and Phenol. *J Am Chem Soc* **1995,** *117*, 9966-9971.
9. Wiebus, E.; Cornils, B. Industrial-Scale Oxo Synthesis with an Immobilized Catalyst. *Chem-Ing-Tech* **1994,** *66*, 916-923.
10. Beller, M.; Cornils, B.; Frohning, C. D.; Kohlpaintner, C. W. Progress in Hydroformylation and Carbonylation. *J Mol Catal a-Chem* **1995,** *104*, 17-85.
11. Cornils, B. Exciting Results from the Field of Homogeneous 2-Phase Catalysis. *Angew. Chem. Int. Ed. Engl.* **1995,** *34*, 1575-1577.
12. Cornils, B.; Wiebus, E. Aqueous Catalysts for Organic-Reactions. *Chemtech* **1995,** *25*, 33-38.
13. Malleron, J. L.; Juin, A.; Baudry, L.; Desmazeau, P.; Girardet, C.; MHoumadi, C.; Guyen, T. P. H. N. Database related to palladium-catalyzed organic chemistry. *Abstr Pap Am Chem Soc* **1997,** *213*, 412-Orgn.
14. Phan, N. T. S.; Van Der Sluys, M.; Jones, C. W. On the nature of the active species in palladium catalyzed Mizoroki-Heck and Suzuki-Miyaura couplings - Homogeneous or heterogeneous catalysis, a critical review. *Adv Synth Catal* **2006,** *348*, 609-679.
15. Dyson, P. J.; Jessop, P. G. Solvent effects in catalysis: rational improvements of catalysts via manipulation of solvent interactions. *Catal Sci Technol* **2016,** *6*, 3302-3316.
16. Bini, R.; Chiappe, C.; Mestre, V. L.; Pomelli, C. S.; Welton, T. A rationalization of the solvent effect on the Diels-Alder reaction in ionic liquids using multiparameter linear solvation energy relationships. *Org Biomol Chem* **2008,** *6*, 2522-2529.
17. Breslow, R.; Guo, T. Diels-Alder Reactions in Nonaqueous Polar-Solvents - Kinetic Effects of Chaotropic and Antichaotropic Agents and of Beta-Cyclodextrin. *J Am Chem Soc* **1988,** *110*, 5613-5617.
18. Cornils, B.; Herrmann, W. A.; Eckl, R. W. Industrial aspects of aqueous catalysis. *J Mol Catal a-Chem* **1997,** *116*, 27-33.

19. Rajadhyaksha, R. A.; Karwa, S. L. Solvent Effects in Catalytic-Hydrogenation. *Chem Eng Sci* **1986,** *41*, 1765-1770.
20. Mukherjee, S.; Vannice, M. A. Solvent effects in liquid-phase reactions - I. Activity and selectivity during citral hydrogenation on Pt/SiO2 and evaluation of mass transfer effects. *J Catal* **2006,** *243*, 108-130.
21. Mukherjee, S.; Vannice, M. A. Solvent effects in liquid-phase reactions - II. Kinetic modeling for citral hydrogenation. *J Catal* **2006,** *243*, 131-148.
22. Akpa, B. S.; D'Agostino, C.; Gladden, L. F.; Hindle, K.; Manyar, H.; McGregor, J.; Li, R.; Neurock, M.; Sinha, N.; Stitt, E. H.; Weber, D.; Zeitler, J. A.; Rooney, D. W. Solvent effects in the hydrogenation of 2-butanone. *J Catal* **2012,** *289*, 30-41.
23. McManus, I.; Daly, H.; Thompson, J. M.; Connor, E.; Hardacre, C.; Wilkinson, S. K.; Bonab, N. S.; ten Dam, J.; Simmons, M. J. H.; Stitt, E. H.; D'Agostino, C.; McGregor, J.; Gladden, L. F.; Delgado, J. J. Effect of solvent on the hydrogenation of 4-phenyl-2-butanone over Pt based catalysts. *J Catal* **2015,** *330*, 344-353.
24. Behtash, S.; Lu, J. M.; Walker, E.; Mamun, O.; Heyden, A. Solvent effects in the liquid phase hydrodeoxygenation of methyl propionate over a Pd(111) catalyst model. *J Catal* **2016,** *333*, 171-183.
25. Behtash, S.; Lu, J. M.; Mamun, O.; Williams, C. T.; Monnier, J. R.; Heyden, A. Solvation Effects in the Hydrodeoxygenation of Propanoic Acid over a Model Pd(211) Catalyst. *J Phys Chem C* **2016,** *120*, 2724-2736.
26. Date, M.; Haruta, M. Moisture effect on CO oxidation over Au/TiO2 catalyst. *J Catal* **2001,** *201*, 221-224.
27. Date, M.; Okumura, M.; Tsubota, S.; Haruta, M. Vital role of moisture in the catalytic activity of supported gold nanoparticles. *Angew. Chem. Int. Ed. Engl.* **2004,** *43*, 2129-2132.
28. Ebbesen, S. D.; Mojet, B. L.; Lefferts, L. In situ ATR-IR study of CO adsorption and oxidation over Pt/Al2O3 in gas and aqueous phase: Promotion effects by water and pH. *J Catal* **2007,** *246*, 66-73.
29. Huang, J. H.; Akita, T.; Faye, J.; Fujitani, T.; Takei, T.; Haruta, M. Propene Epoxidation with Dioxygen Catalyzed by Gold Clusters. *Angew. Chem. Int. Ed. Engl.* **2009,** *48*, 7862-7866.
30. Zope, B. N.; Hibbitts, D. D.; Neurock, M.; Davis, R. J. Reactivity of the Gold/Water Interface During Selective Oxidation Catalysis. *Science* **2010,** *330*, 74-78.
31. Rossmeisl, J.; Skulason, E.; Bjorketun, M. E.; Tripkovic, V.; Norskov, J. K. Modeling the electrified solid-liquid interface. *Chem Phys Lett* **2008,** *466*, 68-71.
32. Miller, K. L.; Lee, C. W.; Falconer, J. L.; Medlin, J. W. Effect of water on formic acid photocatalytic decomposition on TiO2 and Pt/TiO2. *J Catal* **2010,** *275*, 294-299.
33. Staszak-Jirkovsky, J.; Subbaraman, R.; Strmcnik, D.; Harrison, K. L.; Diesendruck, C. E.; Assary, R.; Frank, O.; Kobr, L.; Wiberg, G. K. H.; Genorio, B.; Connell, J. G.; Lopes, P. P.; Stamenkovic, V. R.; Curtiss, L.; Moore, J. S.; Zavadil, K. R.; Markovic, N. M. Water as a Promoter and Catalyst for Dioxygen Electrochemistry in Aqueous and Organic Media. *Acs Catal* **2015,** *5*, 6600-6607.
34. Cheng, T.; Xiao, H.; Goddard, W. A. Free-Energy Barriers and Reaction Mechanisms for the Electrochemical Reduction of CO on the Cu(100) Surface, Including Multiple Layers of Explicit Solvent at pH 0. *J Phys Chem Lett* **2015,** *6*, 4767-4773.

35. Zhang, L.; Karim, A. M.; Engelhard, M. H.; Wei, Z. H.; King, D. L.; Wang, Y. Correlation of Pt-Re surface properties with reaction pathways for the aqueous-phase reforming of glycerol. *J Catal* **2012,** *287*, 37-43.
36. Tupy, S. A.; Karim, A. M.; Bagia, C.; Deng, W. H.; Huang, Y. L.; Vlachos, D. G.; Chen, J. G. G. Correlating Ethylene Glycol Reforming Activity with In Situ EXAFS Detection of Ni Segregation in Supported NiPt Bimetallic Catalysts. *Acs Catal* **2012,** *2*, 2290-2296.
37. Karim, A. M.; Howard, C.; Roberts, B.; Kovarik, L.; Zhang, L.; King, D. L.; Wang, Y. In Situ X-ray Absorption Fine Structure Studies on the Effect of pH on Pt Electronic Density during Aqueous Phase Reforming of Glycerol. *Acs Catal* **2012,** *2*, 2387-2394.
38. He, R.; Davda, R. R.; Dumesic, J. A. In situ ATR-IR spectroscopic and reaction kinetics studies of water-gas shift and methanol reforming on Pt/Al2O3 catalysts in vapor and liquid phases. *J Phys Chem B* **2005,** *109*, 2810-2820.
39. Taylor, C. D.; Neurock, M. Theoretical insights into the structure and reactivity of the aqueous/metal interface. *Curr Opin Solid St M* **2005,** *9*, 49-65.
40. Yoon, Y.; Rousseau, R.; Weber, R. S.; Mei, D. H.; Lercher, J. A. First-Principles Study of Phenol Hydrogenation on Pt and Ni Catalysts in Aqueous Phase. *J Am Chem Soc* **2014,** *136*, 10287-10298.
41. Faheem, M.; Suthirakun, S.; Heyden, A. New Implicit Solvation Scheme for Solid Surfaces. *J Phys Chem C* **2012,** *116*, 22458-22462.
42. Cramer, C. J. In *Essentials of computational chemistry : theories and models*, J. Wiley: West Sussex, England ; New York, 2002; p xvii, 542 p.
43. Okamoto, Y. Density-functional calculations of atomic and molecular adsorptions on 55-atom metal clusters: Comparison with (111) surfaces. *Chem Phys Lett* **2005,** *405*, 79-83.
44. Okamoto, Y. Comparison of hydrogen atom adsorption on Pt clusters with that on Pt surfaces: A study from density-functional calculations. *Chem Phys Lett* **2006,** *429*, 209-213.
45. Car, R.; Parrinello, M. Unified Approach for Molecular-Dynamics and Density-Functional Theory. *Phys Rev Lett* **1985,** *55*, 2471-2474.
46. Carloni, P.; Rothlisberger, U.; Parrinello, M. The role and perspective of a initio molecular dynamics in the study of biological systems. *Acc Chem Res* **2002,** *35*, 455-464.
47. Iftimie, R.; Minary, P.; Tuckerman, M. E. Ab initio molecular dynamics: Concepts, recent developments, and future trends. *Proc Natl Acad Sci USA* **2005,** *102*, 6654-6659.
48. Hibbitts, D. D.; Neurock, M. Influence of oxygen and pH on the selective oxidation of ethanol on Pd catalysts. *J Catal* **2013,** *299*, 261-271.
49. Chen, L. D.; Urushihara, M.; Chan, K. R.; Norskov, J. K. Electric Field Effects in Electrochemical CO2 Reduction. *Acs Catal* **2016,** *6*, 7133-7139.
50. Mattsson, T. R.; Paddison, S. J. Methanol at the water-platinum interface studied by ab initio molecular dynamics. *Surf Sci* **2003,** *544*, L697-L702.
51. Otani, M.; Hamada, I.; Sugino, O.; Morikawa, Y.; Okamoto, Y.; Ikeshoji, T. Structure of the water/platinum interface - a first principles simulation under bias potential. *Phys Chem Chem Phys* **2008,** *10*, 3609-3612.

52. Yang, J.; Dauenhauer, P. J.; Ramasubramaniam, A. The role of water in the adsorption of oxygenated aromatics on Pt and Pd. *J Comput Chem* **2013,** *34*, 60-66.
53. Klamt, A.; Schuurmann, G. Cosmo - a New Approach to Dielectric Screening in Solvents with Explicit Expressions for the Screening Energy and Its Gradient. *J Chem Soc, Perkin Trans 2* **1993**, 799-805.
54. Saleheen, M.; Heyden, A. Liquid-Phase Modeling in Heterogeneous Catalysis. *Acs Catal* **2018,** *8*, 2188-2194.
55. Zhang, Y. K.; Liu, H. Y.; Yang, W. T. Free energy calculation on enzyme reactions with an efficient iterative procedure to determine minimum energy paths on a combined ab initio QM/MM potential energy surface. *J Chem Phys* **2000,** *112*, 3483-3492.
56. Hu, H.; Lu, Z. Y.; Yang, W. T. QM/MM minimum free-energy path: Methodology and application to triosephosphate isomerase. *J Chem Theory Comput* **2007,** *3*, 390-406.
57. Hu, H.; Lu, Z. Y.; Parks, J. M.; Burger, S. K.; Yang, W. T. Quantum mechanics/molecular mechanics minimum free-energy path for accurate reaction energetics in solution and enzymes: Sequential sampling and optimization on the potential of mean force surface. *J Chem Phys* **2008,** *128*, 034105:1-18.
58. Faheem, M.; Heyden, A. Hybrid Quantum Mechanics/Molecular Mechanics Solvation Scheme for Computing Free Energies of Reactions at Metal-Water Interfaces. *J Chem Theory Comput* **2014,** *10*, 3354-3368.
59. Salacuse, J. J.; Denton, A. R.; Egelstaff, P. A.; Tau, M.; Reatto, L. Finite-size effects in molecular dynamics simulations: Static structure factor and compressibility .2. Application to a model krypton fluid. *Phys Rev E* **1996,** *53*, 2390-2401.
60. Castro-Roman, F.; Benz, R. W.; White, S. H.; Tobias, D. J. Investigation of finite system size effects in molecular dynamics simulations of lipid bilayers. *J Phys Chem B* **2006,** *110*, 24157-24164.
61. Lebowitz, J. L.; Percus, J. K. Long-Range Correlations in a Closed System with Applications to Nonuniform Fluids. *Phys Rev* **1961,** *122*, 1675-1691.
62. Lebowitz, J. L.; Percus, J. K. Thermodynamic Properties of Small Systems. *Phys Rev* **1961,** *124*, 1673-1681.
63. Mandell, M. J. Properties of a Periodic Fluid. *J Stat Phys* **1976,** *15*, 299-305.
64. Pratt, L. R.; Haan, S. W. Effects of Periodic Boundary-Conditions on Equilibrium Properties of Computer-Simulated Fluids .1. Theory. *J Chem Phys* **1981,** *74*, 1864-1872.
65. Faheem, M.; Saleheen, M.; Lu, J. M.; Heyden, A. Ethylene glycol reforming on Pt(111): first-principles microkinetic modeling in vapor and aqueous phases. *Catal Sci Technol* **2016,** *6*, 8242-8256. **A new transition state for primary C-H cleavage of ethylene glycol was later found which has 0.10 eV lower energy than reported herein.*
66. Spohr, E. Computer-Simulation of the Water Platinum Interface. *J Phys Chem-Us* **1989,** *93*, 6171-6180.
67. Heinz, H.; Vaia, R. A.; Farmer, B. L.; Naik, R. R. Accurate Simulation of Surfaces and Interfaces of Face-Centered Cubic Metals Using 12-6 and 9-6 Lennard-Jones Potentials. *J Phys Chem C* **2008,** *112*, 17281-17290.
68. Klamt, A. Conductor-Like Screening Model for Real Solvents - a New Approach to the Quantitative Calculation of Solvation Phenomena. *J Phys Chem-Us* **1995,** *99*, 2224-2235.

69. Mathew, K.; Sundararaman, R.; Letchworth-Weaver, K.; Arias, T. A.; Hennig, R. G. Implicit solvation model for density-functional study of nanocrystal surfaces and reaction pathways. *J Chem Phys* **2014,** *140*, 084106:1-8.
70. Fishman, M.; Zhuang, H. L. L.; Mathew, K.; Dirschka, W.; Hennig, R. G. Accuracy of exchange-correlation functionals and effect of solvation on the surface energy of copper. *Phys Rev B* **2013,** *87*.
71. Kresse, G.; Furthmuller, J. Efficiency of ab-initio total energy calculations for metals and semiconductors using a plane-wave basis set. *Comput Mater Sci* **1996,** *6*, 15-50.
72. Kresse, G.; Furthmuller, J. Efficient iterative schemes for ab initio total-energy calculations using a plane-wave basis set. *Phys Rev B* **1996,** *54*, 11169-11186.
73. Blochl, P. E. Projector Augmented-Wave Method. *Phys Rev B* **1994,** *50*, 17953-17979.
74. Perdew, J. P.; Yue, W. Accurate and Simple Density Functional for the Electronic Exchange Energy - Generalized Gradient Approximation. *Phys Rev B* **1986,** *33*, 8800-8802.
75. Perdew, J. P.; Wang, Y. Accurate and Simple Analytic Representation of the Electron-Gas Correlation-Energy. *Phys Rev B* **1992,** *45*, 13244-13249.
76. Perdew, J. P.; Burke, K.; Ernzerhof, M. Generalized gradient approximation made simple. *Phys Rev Lett* **1996,** *77*, 3865-3868.
77. Monkhorst, H. J.; Pack, J. D. Special Points for Brillouin-Zone Integrations. *Phys Rev B* **1976,** *13*, 5188-5192.
78. Methfessel, M.; Paxton, A. T. High-Precision Sampling for Brillouin-Zone Integration in Metals. *Phys Rev B* **1989,** *40*, 3616-3621.
79. Makov, G.; Payne, M. C. Periodic Boundary-Conditions in Ab-Initio Calculations. *Phys Rev B* **1995,** *51*, 4014-4022.
80. Harris, J. Simplified Method for Calculating the Energy of Weakly Interacting Fragments. *Phys Rev B* **1985,** *31*, 1770-1779.
81. Matthew, W.; Foulkes, C.; Haydock, R. Tight-Binding Models and Density-Functional Theory. *Phys Rev B* **1989,** *39*, 12520-12536.
82. Henkelman, G.; Jonsson, H. Improved tangent estimate in the nudged elastic band method for finding minimum energy paths and saddle points. *J Chem Phys* **2000,** *113*, 9978-9985.
83. Henkelman, G.; Uberuaga, B. P.; Jonsson, H. A climbing image nudged elastic band method for finding saddle points and minimum energy paths. *J Chem Phys* **2000,** *113*, 9901-9904.
84. Henkelman, G.; Jonsson, H. A dimer method for finding saddle points on high dimensional potential surfaces using only first derivatives. *J Chem Phys* **1999,** *111*, 7010-7022.
85. Heyden, A.; Bell, A. T.; Keil, F. J. Efficient methods for finding transition states in chemical reactions: Comparison of improved dimer method and partitioned rational function optimization method. *J Chem Phys* **2005,** *123*, 224101:1-14.
86. Ahlrichs, R.; Bar, M.; Haser, M.; Horn, H.; Kolmel, C. Electronic-Structure Calculations on Workstation Computers - the Program System Turbomole. *Chem Phys Lett* **1989,** *162*, 165-169.

87. Treutler, O.; Ahlrichs, R. Efficient Molecular Numerical-Integration Schemes. *J Chem Phys* **1995,** *102*, 346-354.
88. Von Arnim, M.; Ahlrichs, R. Performance of parallel TURBOMOLE for density functional calculations. *J Comput Chem* **1998,** *19*, 1746-1757.
89. Schafer, A.; Horn, H.; Ahlrichs, R. Fully Optimized Contracted Gaussian-Basis Sets for Atoms Li to Kr. *J Chem Phys* **1992,** *97*, 2571-2577.
90. Weigend, F.; Ahlrichs, R. Balanced basis sets of split valence, triple zeta valence and quadruple zeta valence quality for H to Rn: Design and assessment of accuracy. *Phys Chem Chem Phys* **2005,** *7*, 3297-3305.
91. Russo, T. V.; Martin, R. L.; Hay, P. J. Effective Core Potentials for Dft Calculations. *J Phys Chem-Us* **1995,** *99*, 17085-17087.
92. Eichkorn, K.; Weigend, F.; Treutler, O.; Ahlrichs, R. Auxiliary basis sets for main row atoms and transition metals and their use to approximate Coulomb potentials. *Theor Chem Acc* **1997,** *97*, 119-124.
93. Weigend, F. Accurate Coulomb-fitting basis sets for H to Rn. *Phys Chem Chem Phys* **2006,** *8*, 1057-1065.
94. Todorov, I. T.; Smith, W.; Trachenko, K.; Dove, M. T. DL_POLY_3: new dimensions in molecular dynamics simulations via massive parallelism. *J Mater Chem* **2006,** *16*, 1911-1918.
95. Natarajan, S. K.; Behler, J. Neural network molecular dynamics simulations of solid-liquid interfaces: water at low-index copper surfaces. *Phys Chem Chem Phys* **2016,** *18*, 28704-28725.
96. Jorgensen, W. L.; Chandrasekhar, J.; Madura, J. D.; Impey, R. W.; Klein, M. L. Comparison of Simple Potential Functions for Simulating Liquid Water. *J Chem Phys* **1983,** *79*, 926-935.
97. Andersen, H. C. Rattle - a Velocity Version of the Shake Algorithm for Molecular-Dynamics Calculations. *J Comput Phys* **1983,** *52*, 24-34.
98. Smith, W.; Forester, T. R. Parallel Macromolecular Simulations and the Replicated Data Strategy .2. The Rd-Shake Algorithm. *Comput Phys Commun* **1994,** *79*, 63-77.
99. Swope, W. C.; Andersen, H. C.; Berens, P. H.; Wilson, K. R. A Computer-Simulation Method for the Calculation of Equilibrium-Constants for the Formation of Physical Clusters of Molecules - Application to Small Water Clusters. *J Chem Phys* **1982,** *76*, 637-649.
100. Jorgensen, W. L. Optimized Intermolecular Potential Functions for Liquid Alcohols. *J Phys Chem-Us* **1986,** *90*, 1276-1284.
101. Geerke, D. P.; Van Gunsteren, W. F. The performance of non-polarizable and polarizable force-field parameter sets for ethylene glycol in molecular dynamics simulations of the pure liquid and its aqueous mixtures. *Mol Phys* **2007,** *105*, 1861-1881.
102. MacKerell, A. D.; Bashford, D.; Bellott, M.; Dunbrack, R. L.; Evanseck, J. D.; Field, M. J.; Fischer, S.; Gao, J.; Guo, H.; Ha, S.; Joseph-McCarthy, D.; Kuchnir, L.; Kuczera, K.; Lau, F. T. K.; Mattos, C.; Michnick, S.; Ngo, T.; Nguyen, D. T.; Prodhom, B.; Reiher, W. E.; Roux, B.; Schlenkrich, M.; Smith, J. C.; Stote, R.; Straub, J.; Watanabe, M.; Wiorkiewicz-Kuczera, J.; Yin, D.; Karplus, M. All-atom empirical potential for molecular modeling and dynamics studies of proteins. *J Phys Chem B* **1998,** *102*, 3586-3616.

103. Steinmann, S. N.; De Morais, R. F.; Gotz, A. W.; Fleurat-Lessard, P.; Iannuzzi, M.; Sautet, P.; Michel, C. Force Field for Water over Pt(111): Development, Assessment, and Comparison. *J Chem Theory Comput* **2018,** *14*, 3238-3251.
104. Reed, A. E.; Weinstock, R. B.; Weinhold, F. Natural-Population Analysis. *J Chem Phys* **1985,** *83*, 735-746.
105. Burow, A. M.; Sierka, M.; Dobler, J.; Sauer, J. Point defects in CaF2 and CeO2 investigated by the periodic electrostatic embedded cluster method. *J Chem Phys* **2009,** *130*, 174710:1-11.
106. Nose, S. A Unified Formulation of the Constant Temperature Molecular-Dynamics Methods. *J Chem Phys* **1984,** *81*, 511-519.
107. Hoover, W. G. Canonical Dynamics - Equilibrium Phase-Space Distributions. *Phys Rev A* **1985,** *31*, 1695-1697.
108. Essmann, U.; Perera, L.; Berkowitz, M. L.; Darden, T.; Lee, H.; Pedersen, L. G. A Smooth Particle Mesh Ewald Method. *J Chem Phys* **1995,** *103*, 8577-8593.
109. Cowan, M. L.; Bruner, B. D.; Huse, N.; Dwyer, J. R.; Chugh, B.; Nibbering, E. T. J.; Elsaesser, T.; Miller, R. J. D. Ultrafast memory loss and energy redistribution in the hydrogen bond network of liquid H2O. *Nature* **2005,** *434*, 199-202.
110. Zwanzig, R. W. High-Temperature Equation of State by a Perturbation Method .1. Nonpolar Gases. *J Chem Phys* **1954,** *22*, 1420-1426.
111. Archontis, G.; Simonson, T.; Moras, D.; Karplus, M. Specific amino acid recognition by aspartyl-tRNA synthetase studied by free energy simulations. *J Mol Biol* **1998,** *275*, 823-846.
112. Jun, Z.; Thomas, S.; Masha, F.; Hiroshi, M.; R., T. H. Protein-protein recognition: An experimental and computational study of the R89K mutation in Raf and its effect on Ras binding. *Protein Science* **1999,** *8*, 50-64.
113. Best, S. A.; Merz, K. M.; Reynolds, C. H. Free energy perturbation study of octanol/water partition coefficients: Comparison with continuum GB/SA calculations. *J Phys Chem B* **1999,** *103*, 714-726.
114. Shirts, M. R.; Pande, V. S. Comparison of efficiency and bias of free energies computed by exponential averaging, the Bennett acceptance ratio, and thermodynamic integration. *J Chem Phys* **2005,** *122*, 144107:1-16.
115. Lu, N. D.; Singh, J. K.; Kofke, D. A. Appropriate methods to combine forward and reverse free-energy perturbation averages. *J Chem Phys* **2003,** *118*, 2977-2984.
116. Ryde, U. How Many Conformations Need To Be Sampled To Obtain Converged QM/MM Energies? The Curse of Exponential Averaging. *J Chem Theory Comput* **2017,** *13*, 5745-5752.
117. Bennett, C. Efficient Estimation of Free Energy Differences from Monte Carlo Data. *J Comput Phys* **1976,** *22*, 245-268.
118. Shirts, M. R.; Bair, E.; Hooker, G.; Pande, V. S. Equilibrium free energies from nonequilibrium measurements using maximum-likelihood methods. *Phys Rev Lett* **2003,** *91*.
119. Kreyszig, E. In *Advanced Engineering Mathematics*, 9th ed.; John Wiley & Sons, Inc.: New York, 2006.
120. Fernandez, D. P.; Goodwin, A. R. H.; Lemmon, E. W.; Sengers, J. M. H. L.; Williams, R. C. A formulation for the static permittivity of water and steam at

temperatures from 238 K to 873 K at pressures up to 1200 MPa, including derivatives and Debye-Huckel coefficients. *J Phys Chem Ref Data* **1997,** *26*, 1125-1166.
121. Herron, J. A.; Morikawa, Y.; Mavrikakis, M. Ab initio molecular dynamics of solvation effects on reactivity at electrified interfaces. *Proc Natl Acad Sci USA* **2016,** *113*, E4937-E4945.
122. Bulo, R. E.; Michel, C.; Fleurat-Lessard, P.; Sautet, P. Multiscale Modeling of Chemistry in Water: Are We There Yet? *J Chem Theory Comput* **2013,** *9*, 5567-5577.
123. Xie, T. J.; Sarupria, S.; Getman, R. B. A DFT and MD study of aqueous-phase dehydrogenation of glycerol on Pt(111): comparing chemical accuracy versus computational expense in different methods for calculating aqueous-phase system energies. *Mol Simulat* **2017,** *43*, 370-378.
124. Zhang, X.; DeFever, R. S.; Sarupria, S.; Getman, R. B. Free Energies of Catalytic Species Adsorbed to Pt(111) Surfaces under Liquid Solvent Calculated Using Classical and Quantum Approaches. *Journal of Chemical Information and Modeling* **2019**.
125. Walker, E.; Ammal, S. C.; Terejanu, G. A.; Heyden, A. Uncertainty Quantification Framework Applied to the Water-Gas Shift Reaction over Pt-Based Catalysts. *J Phys Chem C* **2016,** *120*, 10328-10339.
126. Hu, H.; Yang, W. T. Development and application of ab initio QM/MM methods for mechanistic simulation of reactions in solution and in enzymes. *J Mol Struc-Theochem* **2009,** *898*, 17-30.
127. deSouza, O. N.; Ornstein, R. L. Effect of periodic box size on aqueous molecular dynamics simulation of a DNA dodecamer with particle-mesh Ewald method. *Biophys J* **1997,** *72*, 2395-2397.
128. Zhang, X. H.; Sewell, T. E.; Glatz, B.; Sarupria, S.; Getman, R. B. On the water structure at hydrophobic interfaces and the roles of water on transition-metal catalyzed reactions: A short review. *Catal Today* **2017,** *285*, 57-64.
129. Michel, C.; Zaffran, J.; Ruppert, A. M.; Matras-Michalska, J.; Jedrzejczyk, M.; Grams, J.; Sautet, P. Role of water in metal catalyst performance for ketone hydrogenation: a joint experimental and theoretical study on levulinic acid conversion into gamma-valerolactone. *Chem Commun* **2014,** *50*, 12450-12453.
130. Desai, S. K.; Pallassana, V.; Neurock, M. A periodic density functional theory analysis of the effect of water molecules on deprotonation of acetic acid over Pd(III). *J Phys Chem B* **2001,** *105*, 9171-9182.
131. Liu, Y.; Gregersen, B. A.; Hengge, A.; York, D. M. Transesterification thio effects of phosphate diesters: Free energy barriers and kinetic and equilibrium isotope effects from density-functional theory. *Biochemistry-Us* **2006,** *45*, 10043-10053.
132. Schweitzer, B.; Steinmann, S.; Michel, C. Can microsolvation effects be estimated from vacuum computations? A case-study of alcohol decomposition at the H2O/Pt(111) interface. *Phys Chem Chem Phys* **2018**.
133. Behler, J.; Parrinello, M. Generalized neural-network representation of high-dimensional potential-energy surfaces. *Phys Rev Lett* **2007,** *98*, 146401:1-4.
134. Behler, J. Representing potential energy surfaces by high-dimensional neural network potentials. *J Phys-Condens Mat* **2014,** *26*, 183001:1-24.
135. Desai, S. K.; Neurock, M. First-principles study of the role of solvent in the dissociation of water over a Pt-Ru alloy. *Phys Rev B* **2003,** *68*, 075420:1-7.

136. Hibbitts, D. D.; Loveless, B. T.; Neurock, M.; Iglesia, E. Mechanistic Role of Water on the Rate and Selectivity of Fischer-Tropsch Synthesis on Ruthenium Catalysts. *Angew. Chem. Int. Ed. Engl.* **2013,** *52*, 12273-12278.
137. Santana, J. A.; Mateo, J. J.; Ishikawa, Y. Electrochemical Hydrogen Oxidation on Pt(110): A Combined Direct Molecular Dynamics/Density Functional Theory Study. *J Phys Chem C* **2010,** *114*, 4995-5002.
138. Skachkov, D.; Rao, C. V.; Ishikawa, Y. Combined First-Principles Molecular Dynamics/Density Functional Theory Study of Ammonia Electrooxidation on Pt(100) Electrode. *J Phys Chem C* **2013,** *117*, 25451-25466.
139. Nie, X. W.; Luo, W. J.; Janik, M. J.; Asthagiri, A. Reaction mechanisms of CO2 electrochemical reduction on Cu(111) determined with density functional theory. *J Catal* **2014,** *312*, 108-122.
140. Huang, Z. Q.; Long, B.; Chang, C. R. A theoretical study on the catalytic role of water in methanol steam reforming on PdZn(111). *Catal Sci Technol* **2015,** *5*, 2935-2944.

CHAPTER 4

INVESTIGATION OF SOLVENT EFFECTS ON THE HYDRODEOXYGENATION OF GUAIACOL OVER Ru CATALYST

Saleheen, M.; Verma, A. M.; Mamun, O; Lu, J.; Heyden, A.

To be submitted

4.1 Abstract

The effects of a liquid phase environment on the hydrodeoxygenation of guaiacol, a prototypical compound of phenol derivatives and lignin derived oligomers over Ru catalyst have been investigated from first principles. A microkinetic reactor model with parameters obtained from density functional theory and implicit solvation schemes was developed to study the effects of condensed phases on the reaction mechanism and kinetic parameters. Phenol was found to be the major aromatic product across all reaction environments. Our model predicts that less protic solvents such as 1-butanol, diethyl ether, and n-hexane have a positive effect on the reaction kinetics compared to vapor and aqueous phases for the production of phenolics. The dominant reaction mechanism for unsaturated aromatics production remains unchanged across all reaction medium. Next, we investigated the possibility of cycloalkane production through hydrogenation of phenol in vapor and liquid phase environments. Our calculations indicated that the reaction pathway for cycloalkane production from phenol is most likely to go through initial dehydrogenation at the hydroxyl group. Based on the vapor phase density functional theory calculations, we proposed a probable reaction pathway and calculated the condensed phase effects along the reaction route. We observed that aqueous phase has a more favorable effect for cycloalkane production from phenol compared to that of vapor phase and other less protic solvents.

Keywords: Solvent effects; Guaiacol; Phenol; Hydrodeoxygenation; Microkinetic modeling; Density functional theory; Ruthenium

4.2 Introduction

The discourse about the feasibility and the economic viability of utilizing biomass as an alternative energy source to produce biofuels has been intensified lately.[1] Despite the sustainability and the environmental friendliness of this renewable resource, the over reliance of the existing technologies on food grade biomass resources poses some significant challenges.[2-3] Therefore, upgrading of lignocellulosic biomass to second generation liquid transportation fuels has been receiving widespread attention.[4-6] Thermochemical conversion processes such as flash pyrolysis or hydrothermal liquefaction can be employed to produce environmentally benign bio-oils from these biomass sources. Bio-oils have higher energy density and better transportability than feedstock biomass and can generate CO_2 and SO_x credits with lower NO_x emissions compared to fossil fuels.[7] Depending on the biomass sources and the conversion processes adopted, the oxygen content in bio-oils can approach as high as 50%, despite having low sulfur and nitrogen content in comparison to fossil-based oils.[8-9] The presence of a large oxygen content combined with corrosive acids and reactive aldehydes in the complex bio-oil mixture leads to several undesirable properties, such as low heating value, high viscosity, non-volatility, thermal instability, high degree of corrosiveness, and tendency to polymerize upon exposure to air[9] which limits the prospect of direct substitution of bio-oils for petroleum fuels. Therefore, some upgrading processes need to be employed to reduce the O/C ratio of the pyrolysis oil for wider range of applications.

Catalytic flash pyrolysis and hydrodeoxygenation (HDO) are two of the most promising catalytic upgrading processes for bio-oil. In-situ catalytic flash pyrolysis processes have the advantage of being operated at atmospheric pressure in absence of

hydrogen;[7] however, the high degree of oxygen removal and the ability to prevent coke deposition on the catalyst surface have made HDO the more promising alternative.[10] Catalytic HDO of bio-oils is typically performed at high hydrogen pressure to reduce the oxygen content as well as to increase the H/C ratio. Sulfided catalysts such as CoMo and NiMo on γ-Al_2O_3 support have been thoroughly studied for HDO due to their conventional industrial application in the hydrodesulfurization (HDS) of petroleum oils.[11-13] However, the instability of the sulfided catalysts in presence of sulfur free bio-oils,[14-15] evolution of sulfur containing HDO intermediates owing to the co-feeding of H_2S to maintain the sulfide structure,[16] boehmite formation of the acidic support in presence of water present in the bio-oil mixture,[15,17] and deactivation of the catalyst surface by polymerization and coke formation[18-19] restrict the prospect employing conventional HDS catalysts for HDO purposes. The tendency of bio-oils to thermal degradation and coke formation makes noble metals industrially attractive catalysts despite the higher cost due to their excellent activity, selectivity and stability.[16,20] They are expected to operate at mild reaction conditions without any introduction of sulfur, and fast deactivation by coke formation in the presence of phenolic compounds can be avoided by employing high hydrogen pressure during HDO. Nonetheless, further improvement of the catalyst design by tailoring the active phase and the support is required to reduce the hydrogen consumption and increase the yield of selective oils.

Bio-oils derived from different feedstocks are typically a complex mixture of water (10-30%) and 300 different organic compounds, comprising of insoluble pyrolytic lignin, aldehydes, organic acids, sugar oligomers, alcohols, and phenol derivatives.[21] Guaiacyl species, being the primary structure of lignin, are predominant in bio-oils and

tend to repolymerize to form coke and heavy hydrocarbons during bio-oil upgrading processes.[22-23] The presence of these diverse organic compounds complicates the bio-oil upgrading process which makes the mechanistic investigation of reaction pathways and catalytic activities very challenging. Therefore, for better understanding of the catalytic upgrading process, it is imperative to select a model compound representative of the pyrolysis oil. In the current study, guaiacol (2-methoxyphenol) has been chosen as the prototypical compound of phenol derivatives and lignin derived oligomers which contains a phenyl ring, two different oxygenated functions, and has been known to play a significant role in the catalyst deactivation process. HDO of guaiacol over a wide range of monometallic transition metals such as Pt[16,24-31], Rh[16,26,30,32], Pd[16,26,28,30,33-34], Ru[26,28,30,33,35-36], Fe[28,37], Mo[33], Ir[33], W[33], Cu[28,33]; post transition metals such as Sn[24] as well as bimetallic catalysts such as Rh-Pd[32], Rh-Pt[32], Pt-Sn[24], Ni-Cu[38], Pd-Fe[28] have been reported. Due to the critical role of metal-support interaction, support acidity, susceptibility of conventional γ-Al_2O_3 support to coke formation[8,39], and its instability in presence of water[17,39]; various supports such as C[26,28,33,35], ZrO_2[16,32,38], TiO_2[29,35], SiO_2[26,35,37-38], CeO_2[38,40], MgO[27,36] have also been tested rigorously. Heeres et al.[41] presented a thorough catalyst screening using noble metals catalysts and compared that with the conventional hydrotreatment catalysts for HDO of fast pyrolysis oil. They addressed Ru/C as the most promising candidate for bio-oil upgrading regarding oil yields, deoxygenation activity, and hydrogen consumption. Our group has previously reported an in-depth vapor phase mechanistic investigation of HDO of guaiacol over Ru(0001) model surface and concluded phenol to be the major product.[42] However, the presence of substantial amount of water in bio-oil feed (30%) combined with the

production of more water during the HDO process can affect the activity as well as the surface structure and chemical composition of the catalysts.[9] If used as a solvent, water has the potential to increase the targeted product selectivity, reduce the undesirable thermal degradation, and facilitate product separation. Sharpless et al.[43] reported accelerated reaction rates of hydrophobic organic compounds in water and argued that the biphasic boundary between water and hydrophobic oil can also play a role. Conversely, Grunwaldt and coworkers[44-45] have investigated various polar and non-polar solvents influence on HDO of guaiacol over Pt based catalysts and reported a higher HDO ability in presence of non-polar solvents.

To address this lack of fundamental understanding of solvent effects, we report herein an investigation of solvent influence on the reaction mechanism and possible activity descriptors for HDO of guaiacol over Ru(0001) model surface. Several studies conducted at relatively mild reaction conditions have reported the presence of aromatic ring saturated products[36,46] which was not considered in our previous study. Therefore, in this study, we have extended our calculations to investigate the formation of phenyl ring saturated products in vapor phase and condensed phases. While electrostatic interactions and hydrogen bonding contributions are instrumental for the interaction between a polar adsorbate and a polar solvent, london dispersion forces play a crucial part for non-polar adsorbate-solvent systems. To consider both of these scenarios, four different solvents of varying degree of polarity (depending on Kamlet and Taft's solvatochromic parameters) have been employed for this study.[47] Specifically, we focused on the effects of liquid water which is a polar, protic solvent, 1-butanol, a polar aprotic solvent, diethyl ether, a 'borderline' polar aprotic solvent, and a non-polar solvent, n-hexane. Using first

principles calculations and a novel implicit solvation scheme for solid surfaces (iSMS),[48] we characterized the solvent effects on the thermodynamics and kinetics of elementary reactions. A mean field microkinetic reactor model was then developed to reexamine the most abundant surface intermediates, dominant reaction pathways, and general kinetic trends in condensed phases. We conclude our findings with a deliberation of our hypotheses and suggest further research. To the best of our knowledge, no theoretical report on solvent effects on the catalytic hydrodeoxygenation of guaiacol over transition metals catalysts has yet been published.

4.3 Computational Approach

4.3.1 Solvation Model

Solvent molecules can affect activity and selectivity of a heterogeneously catalyzed reaction in a number of ways, it can 1) compete with the adsorbed moieties for the active catalyst sites, 2) directly involve itself in the reaction coordinate, thereby providing lower energy pathways, for example, Grotthuss mechanism,[49] and 3) affect the stability of the charged intermediates or transition states. While computational investigations of chemical reactions occurring at solid-liquid interfaces can be very challenging,[50] in this study, the liquid phase effect has been approximated by employing the iSMS method.[48] A detailed discussion about the iSMS methodology and validation can be found elsewhere.[48,50-54]

The fundamental idea behind the iSMS methodology is to include long-range metallic interactions through periodic-slab models in the absence of solvent molecules and to represent the liquid phase effect as a perturbation on the (free) energy differences

which is described by (sufficiently large) cluster models embedded in an isotropic continuum of constant dielectric. Consequently, the free energy function of a moiety adsorbed on a periodic metal slab submerged in liquid can be illustrated using the following subtraction scheme,

$$G^{liquid}_{surface+intermediate} = G^{vacuum}_{surface+intermediate} + (G^{liquid}_{cluster+intermediate} - E^{vacuum}_{cluster+intermediate}) \quad (4.1)$$

where $G^{vacuum}_{surface+intermediate}$ is the free energy of the adsorbed moieties in vapor phase, $G^{liquid}_{cluster+intermediate}$ is the free energy of the surface cluster model immersed in an implicit solvent which is fashioned by extracting selected metal atoms and removing the periodic boundary conditions, and $E^{vacuum}_{cluster+intermediate}$ is the DFT energy of the same cluster in absence of any fluid phase environment. Conductor-like Screening Model for Real Solvents (COSMO-RS)[55] approach using the COSMOtherm program package[56] has been employed to finally compute $G^{liquid}_{surface+intermediate}$. Solvent thermodynamic properties are readily available in COSMOtherm database,[56] which are based on the quantum chemical COSMO calculations at the BP-TZVP level of theory. For any other adsorbed moiety, the COSMO-RS input file was generated with the help of COSMO calculations at the same level of theory.

4.3.2 Periodic and Non-periodic DFT Calculations

The catalyst model investigated in this study has been explored earlier for the vapor phase hydrodeoxygenation of guaiacol over Ru(0001) model surface,[42] and we encourage the interested readers to review the methods section of that article for a comprehensive summary of the computational details employed to perform the periodic

plane-wave DFT calculations. However, it has been demonstrated lately that the Bayesian error estimation functional with van der Waals correction (BEEF-vdW)[57] perform significantly better for calculating the adsorption energies of larger adsorbates[58-59] as well as simple adsorbates such as CO[60-61] in comparison to the PBE functional[62] with dispersion corrections.[63] Hence, the energetics of the adsorption-desorption processes as well as the all the elementary steps of the phenol hydrogenation network investigated in this study have been computed utilizing the BEEF-vdW functional. Non-periodic cluster model DFT calculations have been performed using the TURBOMOLE 6.5[64-65] program package. The cluster surfaces have been constructed by removing the periodicity of the geometries obtained from plane-wave DFT calculations and modeled as a 5×5 surface with 2 layers of metal atoms. Atoms that comprise the adsorbate molecules have been characterized by employing all electron basis sets of triple-ζ quality,[66] while a relativistic small core potential (ECP) combined with a basis set of the same quality as the adsorbate atoms have been employed for the valence electrons of the metal (Ru) atoms.[67] Electron exchange and correlation terms of DFT have been described by utilizing the BP86 functional[68-69] and coulomb potentials were approximated in conjunction with the RI-J approximation using auxiliary basis sets.[70-71] Single point energy calculations have been performed for the cluster models using a self-consistent field energy convergence criterion of 1.0×10^{-7} Ha with an m4 spherical grid.[72] Multiple spin states were investigated for each cluster model to identify the lowest energy spin state. For the lowest energy spin state, Conductor like screening model calculations (COSMO)[73-74] were performed where the solute molecule is embedded in a molecule shaped cavity surrounded by a dielectric medium of infinite dielectric constant (hence Conductor).

Finally, the dielectric constant was scaled down to the respective dielectric constant of the solvents by utilizing the COSMO-RS[56] program package to obtain the solvation energy. Considering the ambiguity associated with the interpretation of cavity radius of transition metal atoms in implicit solvation models,[50,75] all calculations have been repeated with a 10% incremental change on the default cavity radius of Ru atoms.

4.3.3 Solvents Investigated

HDO of guaiacol have been previously studied for the pure reactant diluted in water, diethylether, decane, octanol, hexadecane, and tetrahydrofuran experimentally.[44,76-78] In organic chemistry, the solvent effects have been attempted to understand regarding the polarity of the solvent, which can be very challenging to convey quantitatively. Empirical estimation of solvent polarity has been calculated based on linear free energy relationships of substituent solvent parameters and equilibrium, kinetic, and spectroscopic measurements.[47] By employing solvatochromic comparison method in linear solvation energy relationship (LSER) theory, Kamlet and Taft presented a set of solvent parameters to establish a solvent polarity scale, namely, $\pi^*, \alpha,$ and $\beta,$ which are related to distinct configurational properties in solution, e.g., solubilities, partition coefficients, thermodynamic and kinetic properties of chemical reactions, etc.[79-81] They correlated solvent dependent physicochemical properties of a given solvent and a reference solvent by introducing some solvent independent coefficients (s, a, b) which specifies the susceptibility of the corresponding parameters, dipolarity/polarizability (π^*), hydrogen-bond donor acidities (α), and hydrogen-bond acceptor basicities (β), respectively. Table C.1 from the supporting information includes the Kamlet-Taft solvent parameters as well as the normalized solvent polarity parameter (E_T^N) for the four

different solvents explored in this study, i.e., water, 1-butanol, diethylether, and n-hexane. The recorded values clearly indicate that water is the most polar protic solvent with high polarizability and hydrogen bond donating ability while n-hexane lies at the other end of the spectrum with no hydrogen bond accepting/donating capability. 1-butanol and diethylether lies in between the above mentioned two as evident from their normalized polarity values.

4.4. Model Development

4.4.1 Microkinetic Modeling

To analyze the implication of reaction energies and the reaction pathways under realistic process conditions, a mean-field microkinetic model was formulated. The formulation of the partition function in the liquid phase environment is complex and dynamic contributions to the free energy of the solute are in general insensitive to whether the solute vibrational frequencies are computed in the gas phase or in the solution. In the parameterization of implicit solvation models, the vibrational partition function is computed for the gas phase species. Hence, the zero-point corrections to the 0 K energies and vibrational partition functions under harmonic approximation were calculated using the vibrational frequencies (ν_i) obtained from vapor phase periodic plane-wave DFT calculations.

$$E_{ZPE} = \frac{1}{2}\sum_i h\nu_i \tag{4.2}$$

$$q_{vib} = \prod_i \frac{1}{1 - \exp(\frac{h\nu_i}{k_B T})} \tag{4.3}$$

It should be noted here that the frequency calculations include relaxations of only adsorbed moieties which result in a reduction of the accuracy of low-lying frequencies that are coupled with surface metal atoms. Considering the accuracy of DFT (or lack thereof) and the inadequacy of harmonic approximation to describe low-lying frequencies, we established a 100 cm^{-1} cutoff value for frequencies (real) that lie below the aforementioned value. This accommodation was not required for the gas phase molecules since the rotational and the vibrational partition functions were rigorously calculated using statistical mechanics.[82]

To account for the liquid phase environment, the solvation free energy obtained from COSMO-RS calculations were utilized to reparametrize the microkinetic model. For the adsorption/desorption processes,

$$\Delta G_{solvent} = \Delta G_{gas} + G_{ads}(solv) - G_{Ru}(solv) \tag{4.4}$$

where $G_{ads}(solv)$ and $G_{Ru}(solv)$ are the free energies of solvation of a Ru cluster with and without an adsorbate, respectively. It is worth mentioning here that the chemical potential of all the gas phase species in a particular solvent is given by the partial pressure (fugacity) of that species in the vapor phase which is in equilibrium with the solvent phase, i.e. we assumed gas-liquid equilibrium in the absence of any mass transfer limitations. The free energy of reaction ($\Delta G^{rxn}_{solvent}$) and free energy of activation ($\Delta G^{\ddagger}_{solvent}$) of the elementary surface reactions were calculated as,

$$\Delta G^{rxn}_{solvent} = \Delta G^{rxn}_{gas} + G_{FS}(solv) - G_{IS}(solv) \tag{4.5}$$

$$\Delta G^{\ddagger}_{solvent} = \Delta G^{\ddagger}_{gas} + G_{TS}(solv) - G_{IS}(solv) \tag{4.6}$$

where the subscripts IS, TS, and FS denotes the initial state, transition state, and final state, respectively. All reactions were presumed to be reversible reactions. Forward rate constants were calculated using harmonic transition state theory (hTST)[83] for all surface mediated elementary processes.

$$k_{forward} = \frac{\gamma k_B T}{h} \exp\left(\frac{-\Delta G^{\ddagger}}{k_B T}\right) \tag{4.7}$$

Here, $\Delta G^{\ddagger}$ is the free energy of activation, T is the absolute temperature, γ is the transmission coefficient, which was assumed to be 1.0 for all cases, and k_B and h are the Boltzmann and Planck constants, respectively. Collision theory was employed for calculating the forward rate constants of non-activated adsorption processes.

$$k_{forward} = \frac{\sigma}{N_o \sqrt{2\pi m k_B T}} \tag{4.8}$$

Here, σ stands for the sticking probability (assumed to be 1.0 for all cases), N_o is the number of catalytic sites per unit surface area, and m is the molecular weight of the adsorbate. Thermodynamic consistency was ensured by calculating the reverse rate constants from thermodynamic equilibrium constants.

$$K_{eq} = \exp\left(\frac{-\Delta G^{rxn}}{k_B T}\right) \tag{4.9}$$

$$k_{reverse} = \frac{k_{forward}}{K_{eq}} \tag{4.10}$$

Finally, with all the rate parameters known, a microkinetic reactor model was developed as a system of differential algebraic equations (DAEs). The fractional coverage of a surface intermediate at steady state is given by,

$$\frac{d\theta_i}{dt} = \sum_j \nu_{i,j} r_j = 0 \tag{4.11}$$

where index i refers to the ith adsorbed species and index j loops over all the elementary reactions. Furthermore, the total number of catalytic sites were conserved, and overall site balance equation was employed to calculate the fractional coverage of empty sites.

$$\sum_i n_i \theta_i = 1 \tag{4.12}$$

A complete list of the number of sites assigned to each species (n_i) can be found in our vapor phase study.[42] All microkinetic models were initialized with a clean Ru surface and solved as a system of DAEs to achieve fractional surface coverages and turnover frequencies (TOFs) at steady state under realistic process conditions.

4.4.2 Adsorbate-adsorbate Interactions

Adsorbate-adsorbate interactions can play a significant role on the adsorption strength as well as the stability of the adsorbed moieties which in turn can affect catalytic activity of transition metal catalysts.[54,75,84-85] Getman et al.[86-87] demonstrated a remarkable change in NO_2 dissociation capability of Pt(111) surface when O coverage is typical of NO oxidation catalysts. As reported in our vapor phase study,[42] without considering any adsorbate-adsorbate interactions, H, CO, and phenoxy (C_6H_5O) become the most abundant surface intermediates while performing a microkinetic modeling study. Hence, to mimic the local chemical environment dependence of adsorption energy in a realistic reaction environment, lateral interaction functional forms have been included in our microkinetic model. While the true description of adsorbate-adsorbate interactions can be very complicated and computationally demanding to realize, we employed the two-

parameter lateral interaction model proposed by Grabow et al.[88] considering its simplicity. Table C.2 of the supporting information includes the functional forms of the lateral interactions introduced in our microkinetic models. A detailed description of the calculation procedure to obtain these functional forms have been discussed in our vapor phase invetigation.[42]

4.5 Results and Discussion

Experimental studies have reported a range of alicyclic and aromatic products for HDO of guaiacol such as 2-methoxy-cyclohexanol, cyclohexanol, cyclohexanone, cyclohexane, benzene, catechol etc. with phenol being a major intermediate detected at short reaction times.[28,30,33,36,46] Therefore, in this study, we aim to describe HDO of guaiacol over Ru(0001) catalysts in two segments. At first, we carried out our study in condensed phases to verify the formation of phenol from hydrodeoxygenation of guaiacol. Next, we examine the possibility of phenyl ring saturation in vapor and condensed phases to produce two major products observed in experimental studies, cyclohexanol and cyclohexanone from phenol.[78,89-92]

4.5.1 HDO of Guaiacol to Unsaturated Aromatics

4.5.1.1 Solvent Effects on the Adsorption Strength of Reaction Intermediates

The introduction of solvent using a continuum solvation model can alter the adsorption strength of reaction intermediate in two different ways, i) incorporating an implicit solvent introduces the previously unaccounted for adsorbate-solvent interaction, and ii) it modifies the metal-adsorbate interaction by changing the electronic structure of the metal due to indirect solvent-metal interactions. Solvent induced changes in the

adsorption strength of a reaction intermediate can significantly affect the overall activity of a catalyst site by modifying the activation and reaction free energies. To investigate the effects of solvent on the adsorption strength of the intermediates involved in HDO of Guaiacol, we computed the difference in adsorption free energy in the absence and presence of solvent,

$$A(g) + *(g) \leftrightarrow A*(g) \tag{4.13}$$

$$A(g) + *(l) \leftrightarrow A*(l) \tag{4.14}$$

$$\Delta\left(G_{ads,A}\right) = G_{ads,A}(l) - G_{ads,A}(g)$$

$$= [G^{A*}(l) - G^{A*}(g)] - [G^{*}(l) - G^{*}(g)] \; = \Delta(\Delta G) \tag{4.15}$$

where, $G_{ads,A}(l)$ and $G_{ads,A}(g)$ are the free energies of adsorption of a gas molecule of intermediate A in the presence and absence of the solvent, $G^{A*}(l)$ and $G^{A*}(g)$ are free energies of adsorbed moiety A in the presence and absence of solvent, and $G^{*}(l)$ and $G^{*}(g)$ are free energies of the clean surface model in the presence and absence of solvent, respectively. It should be noted here that while many adsorbed moieties can be unstable when separated from their adsorption site; nonetheless, this scheme permits us to compare relative adsorption strength in liquid phase environment with respect to gas phase adsorption strength.

The investigated surface moieties in the reaction network of HDO of guaiacol and the calculated change in their adsorption strength in various reaction environments are listed in Table 4.1. In total, we investigated 39 surface intermediates in our reaction network that includes guaiacol, phenol, catechol, and their derivatives. Snapshots of all adsorbed geometries can be found in our previous vapor phase study.[42] For the

convenience of comparison of solvent effect on the adsorption strength of the surface intermediates, we classified the intermediates into four different classes of structurally similar species.

Class I: Guaiacol and Its Derivatives

Presence of a liquid-phase environment significantly stabilizes the adsorption of guaiacol on Ru(0001) sites ($\Delta(\Delta G^{water}) = -0.22\ eV, \Delta(\Delta G^{1-butanol}) = -0.47\ eV, \Delta\left(\Delta G^{diethylether}\right) = -0.43\ eV, \Delta(\Delta G^{n-hexane}) = -0.33\ eV$). Solvents employed in this study can be arranged in the order of their effect on adsorption strength of guaiacol and its dehydrogenated and partially hydrogenated derivatives as 1-Butanol > Diethyl ether > n-Hexane > Water. This phenomenon can be attributed to the fact that guaiacol has a large non-polar aromatic ring with a polar hydroxyl group and slightly polar methoxy group. The presence of a polar solvent (Water) ensures favorable solute-solvent interaction i.e. formation of hydrogen bonds, thereby increasing the adsorption strength of guaiacol and its derivatives. Reducing the polarity of the solvent (1-Butanol, Diethyl ether) enhances the stabilization of adsorption strength of these species because of the additional favorable interaction between non-polar fragments of solute and solvent due to increased London forces all the while retaining some of the favorable interaction between polar fragments of solute and solvent. For non-polar aprotic solvents such as n-hexane, the stabilization of adsorption strength only comes from the favorable solute-solvent interaction due to London dispersion forces, which reduces the solvent effect on the adsorption strength of guaiacol and its derivatives compared to that of 1-Butanol and Diethyl ether. Partially hydrogenated ($C_6H_4H_{\alpha/\beta}(OH)(OC_xH_y)$), x=[0,1], y=[0,3]) and

dehydrogenated ($C_6H_4(O_vH_w)(O_xC_yH_z)$), v=[0,1], w=[0,1], x=[0,1], y=[0,1], z=[0,3]) species of guaiacol all maintain the same order of solvent effect on the adsorption strength. For example, 2-methoxy-phenyl ($C_6H_4(OCH_3)$) intermediate can be produced by $C_{aryl(\alpha)}$-OH bond scission of guaiacol. Due to the loss of polar hydroxyl group, the solvent stabilization of the adsorption strength in water gets reduced ($\Delta(\Delta G^{water}) = -0.07\ eV$) compared to that of guaiacol, while the increasingly non-polar solvents such as 1-Butanol, Diethyl ether and n-Hexane retain most of the solvent stabilization ($\Delta(\Delta G^{1-butanol}) = -0.35\ eV, \Delta\left(\Delta G^{diethylether}\right) = -0.33\ eV, \Delta(\Delta G^{n-hexane}) = -0.24\ eV$) due to dispersion forces between non-polar fragments of solute and solvent.

Class II: Phenol, Anisole, Catechol, Benzene and Their Derivatives

Phenol, due to the presence of strongly polar hydroxyl group shows significant solvent stabilization in aqueous phase ($\Delta(\Delta G^{water}) = -0.20\ eV$), and the presence of non-polar aromatic ring ensures the increase in adsorption strength for other solvents with various degree of polarity ($\Delta(\Delta G^{1-butanol}) = -0.38\ eV, \Delta\left(\Delta G^{diethylether}\right) = -0.35\ eV, \Delta(\Delta G^{n-hexane}) = -0.26\ eV$). On the other end of the spectrum, benzene, being non-polar, shows small solvent stabilization in its adsorption strength in the aqueous phase (($\Delta(\Delta G^{water}) = -0.10\ eV$). However, the favorable solute-solvent interaction due to increased london dispersion forces in other solvents, it shows a sizable solvent stabilization in adsorption strength ($\Delta(\Delta G^{1-butanol}) = -0.26\ eV, \Delta\left(\Delta G^{diethylether}\right) = -0.24\ eV, \Delta(\Delta G^{n-hexane}) = -0.17\ eV$). Overall, phenol ($C_6H_5OH$), anisole ($C_6H_5OCH_3$), catechol ($C_6H_4(OH)_2$), Benzene($C_6H_6$), and their

dehydrogenated surface intermediates follow the same order of solvent stabilization as mentioned before for guaiacol species.

Class III: Methane and Its Derivatives

Methane and its dehydrogenated derivatives such as methyl (CH_3), methylene (CH_2), and methylidene (CH) show marginally weaker adsorption strength in the aqueous phase due to their non-polar nature. For example, adsorption strength of methane in liquid water gets increased by 0.04 eV. We also find that adsorption strength of methane and its derivatives is hardly affected by the presence of other solvents such as 1-butanol, diethyl ether, and n-hexane.

Class IV: Methanol and Its Derivatives

Presence of liquid water weakens the adsorption strength of strongly polar methanol and its dehydrogenated species methoxy (CH_3O) ($\Delta(\Delta G^{water}_{methanol}) = 0.12\ eV, \Delta\left(\Delta G^{water}_{methoxy}\right) = 0.09\ eV$). This inverse solvent effect on a polar species can be rationalized by observing their binding modes and their strongly polar nature. Both methanol and methoxy species binds to the Ru(0001) surface through the O atom, a hydrogen bond donor. Due to their polar nature, these species have a favorable solute-solvent interaction in polar solvents (through hydrogen bonding) which in turn weakens solute-surface interaction, thereby reducing the adsorption strength when following bond order conservation principles. As we decrease the polarity of the solvents, the adsorption strength gets stabilized. For less polar dehydrogenated species such as formaldehyde (CH_2O) and formyl (CHO), the presence of a liquid phase environment hardly affects the adsorption strength.

4.5.1.2 Solvent Effects on Elementary Processes

Figure 4.1 illustrates a schematic of the investigated elementary reactions involved in the HDO of guaiacol over Ru(0001) model surface. Energetics of all adsorption/desorption reactions are reported in Table 4.2 using PBE-D3 and BEEF-vdW functionals in different reaction environments at 473K reaction temperature. Free energies of reaction and free energies of activation of all elementary surface processes in different reaction environment are listed in Table 4.3 for a reaction temperature of 473K.

In the following, we discuss the solvent effects on the free energy of reaction and free energy of activation of various elementary processes involved in HDO of guaiacol. For the convenience of comparison, the reaction pathways have been labeled from 2 to 8 according to the first reaction step labeled in Figure 4.1, adsorption of guaiacol being the first reaction step. Pathways 2 and 3 start with selective hydrogenation of $C_{aryl(\beta)}$ and $C_{aryl(\alpha)}$ of guaiacol, respectively. Direct removal of a hydroxyl group, methoxy group, and a methyl group from guaiacol have been considered in pathways 4, 5, and 7, respectively. Pathways 6 and 8 considers the dehydrogenation of guaiacol through C-H bond scission of the methoxy group and O-H bond scission of the hydroxyl group, respectively.

I: Selective hydrogenation of the phenyl ring

Selective hydrogenation of the phenyl ring of guaiacol to form $C_6H_4H_\beta(OH)(OCH_3)$ (step 2) and $C_6H_4H_\alpha(OH)(OCH_3)$ (step 3) are both endergonic steps in the vapor phase ($\Delta G_{rxn} = 0.40$ eV and $\Delta G_{rxn} = 0.51$ eV, respectively) and kinetically demanding with a free energy of activation of 1.10 eV and 1.14 eV, respectively, which makes pathways 2 and 3 unfavorable. Liquid solvents employed in this study (water, 1-

butanol, diethyl ether, and n-hexane) have an unfavorable effect on the free energies of $C_{aryl(\beta)}$-H hydrogenation, making it more endergonic (free energy of reaction ranging from 0.41 eV to 0.49 eV) and making it kinetically more demanding. Liquid water does not have any effect on the free energy of reaction of $C_{aryl(\alpha)}$-H hydrogenation, with a minimal increase of the free energy of activation ($\Delta(\Delta G^{\ddagger})$=0.04eV). Employing other solvents such as 1-butanol, diethyl ether, or n-hexane have a minimal exergonic effect on the free energy of reaction with a slight increase in the free energy of activation ($\Delta(\Delta G^{\ddagger}_{1-\text{butanol}})$ =0.06eV, $\Delta(\Delta G^{\ddagger}_{\text{diethyl ether}})$ =0.06eV, $\Delta(\Delta G^{\ddagger}_{\text{n-hexane}})$ =0.07eV).

Similar to the vapor phase, further dehydrogenation of the methoxy group (step 9) remains challenging compared to the methoxy group removal (step 10) of $C_6H_4H_\beta(OH)(OCH_3)$ in all solvents studied. Liquid water increases the free energy of activation of subsequent methylene group removal (step 23) process by 0.16 eV while it remains largely unaffected in all other solvent medium. Energetics of the hydrogenation of resulting $C_6H_4H_\beta(OH)(O)$ species to produce $C_6H_5(OH)_2$ (step 36) also show minimal perturbation from the vapor phase for different solvent media. The final step to produce phenol involves dehydroxylation of the phenyl ring (step 41) and employing increasingly non-polar solvents makes this step more facile by 0.11-0.15 eV.

Less protic solvent mediums such as 1-butanol, diethyl ether, and n-hexane have an endergonic effect on the free energy of activation for dehydroxylation of $C_{aryl(\alpha)}$ hydrogenated species of guaiacol (step 11) to produce anisole while the energetics remain unchanged in water compared to that of vapor phase. Different reaction medium also exerts limited effect on the kinetics of the subsequent dehydrogenations of anisole (step

24 and step 37). Overall, the energetics of pathways 2 and 3 suggest that HDO of guaiacol does not proceed through selective hydrogenation of the phenyl ring, similar to the vapor phase, which supports the experimental observations.[28]

II: Direct removal of functional groups

Pathways 4, 5, and 7 consider direct removal of -OH, -OCH_3, and -CH_3 functional group, which were found to be kinetically difficult in the vapor phase and it remains the same in liquid phase environment. Liquid phase environment exerts an endergonic effect on the thermodynamics of removal of hydroxyl species from guaiacol to produce 2-methoxy phenyl species ($C_6H_4OCH_3$) (step 4). While presence of an aqueous phase increases the free energy of activation by 0.07 eV, other solvent media hardly affects the kinetics of the reaction. Subsequent hydrogenation to anisole, however, gets more exergonic in the liquid phase environment with water contributing the most $\Delta(\Delta G_{rxn}) = -0.22$ eV) while the kinetics also become slightly facilitated.

In the methoxy group removal pathway (pathway 5), the removal of -OCH_3 species (step 5) becomes kinetically more unfavorable in water ($\Delta(\Delta G^{\dagger})$=0.07eV) while other solvents have a minimal effect. Subsequent hydrogenation of 2-hydroxy phenyl species (C_6H_4OH) to produce phenol (step 13) becomes thermodynamically more favorable in the liquid phase environment compared to that of vapor phase.

The seventh pathway consists of removal of a methyl group from guaiacol to produce a hydrogen catecholate species ($C_6H_4(OH)(O)$) (step 7) which is largely exergonic in the vapor phase ($\Delta G_{rxn} = -1.35$ eV). Introduction of a liquid phase environment has an endergonic effect on the thermodynamics of the reaction while the

kinetics remain mostly unchanged. The hydrogen catecholate can be hydrogenated to catechol (step 18) which remains largely unchanged in liquid water, while less protic solvents have a favorable effect on both the thermodynamics and the kinetics of this elementary process. Catechol can be either dehydroxylated to 2-hydroxy phenyl species (C_6H_4OH) (step 27) or hydrogenated to produce $C_6H_5(OH)_2$ species (step 28) which are both kinetically very demanding. Presence of a liquid phase environment does not affect the kinetics of these processes while having minimal effect on thermodynamics.

In summary, liquid phase environment does not help these kinetically demanding processes of direct functional group removal to make them more facile.

III: Dehydrogenation of methoxy and hydroxyl groups

In pathways 6 and 8, we discuss the initial dehydrogenation of -OCH_3 and -OH group of guaiacol. The removal of methoxy group from guaiacol to produce 2-methylene-oxy-phenol intermediate ($C_6H_4(OH)(OCH_2)$) (step 6) is both thermodynamically and kinetically favorable in the vapor phase ($\Delta G_{rxn} = -0.36$ eV, $\Delta G^{\ddagger} = 0.50$ eV). Introduction of aqueous phase has an endergonic effect on the free energy of reaction ($\Delta(\Delta G_{rxn}) = 0.09$ eV) with negligible impact on the free energy of activation ($\Delta(\Delta G^{\ddagger}) = 0.02$ eV). All the other less protic solvents (1-butanol, diethyl ether, and n-hexane) have a less endergonic effect on the thermodynamics of the reaction compared to water ($\Delta(\Delta G_{rxn}) = 0.04$ eV) with kinetics remaining unperturbed. 2-methylene-oxy-phenol species can go through -OCH_2 removal (step 14), dehydrogenation at the hydroxyl group (step 15), dehydrogenation of the methylene group (step 16), and removal of -CH_2 (step 17). The most facile path in the vapor phase is dehydrogenation of the methylene group

(step 16) ($\Delta G_{rxn} = -0.53$ eV, $\Delta G^{\ddagger} = 0.02$ eV), which remains unchanged in the liquid phase environment. However, while the liquid phase environment does not affect the free energy of reaction of this elementary step, the free energy of activation is perturbed differently for polar and non-polar solvents. The reaction becomes barrierless in an aqueous phase while for other solvents, the free energy of activation increases by 0.10 eV compared to that of the vapor phase. The product of step 16, 2-methylidyne-oxy-phenol ($C_6H_4(OH)(OCH)$) can then either undergo methyne (-CH) removal to produce hydrogen catecholate intermediate ($C_6H_4(OH)O$) (step 26) or formyl (-OCH) removal to produce 2-hydroxy-phenyl species (C_6H_4OH) (step 25). Step 26 is much more facile compared to step 25 in the vapor phase which remains consistent in the presence of liquid phase environment. However, while liquid water makes the process more exergonic by 0.09 eV, other less protic solvents makes it more endergonic by 0.17 eV compared to that of the vapor phase. Elementary processes involving $C_6H_4(OH)O$ species have already been discussed in the previous section and consequently will not be discussed further.

Finally, the pathway eight, which involves dehydrogenation of the hydroxyl group of guaiacol to produce guaiacolate intermediate($C_6H_4(O)(OCH_3)$) (step 8) is the most facile reaction pathway in vapor phase ($\Delta G_{rxn} = -0.77$ eV, $\Delta G^{\ddagger} = 0.29$ eV). In the liquid phase, all solvents pose an endergonic effect on the free energy of reaction of this elementary process by ~0.10 eV. The free energy of activation remains unaltered in less protic solvents while liquid water shows an endergonic effect ($\Delta(\Delta G^{\ddagger}) = 0.08$ eV) making this step competitive with the dehydrogenation of the methoxy group of guaiacol (step 6). Next, the methoxy group is dehydrogenated (step 22) which is more facile ($\Delta G_{rxn} = -0.32$ eV, $\Delta G^{\ddagger} = 0.53$ eV) compared to the alternative step which involves

complete removal of the methoxy group (step 21) ($\Delta G_{rxn} = 0.21$ eV, $\Delta G^{\ddagger} = 1.08$ eV) in the vapor phase. Liquid water further facilitates the kinetics of methoxy group dehydrogenation step (step 22) ($\Delta(\Delta G^{\ddagger}) = -0.06$ eV). The product of step 22, 2-methylene-oxy-phenolate ($C_6H_4(O)(OCH_2)$) species then undergoes a barrierless dehydrogenation reaction (step 33) across all reaction environment to produce 2-methylidyne-oxy-phenolate ($C_6H_4(O)(OCH)$) species where the thermodynamics of the process becomes slightly exergonic (by ~0.05 eV) when using less protic solvents compared to that of the vapor phase. In the vapor phase, two kinetically competing reactions develop at this point, methylidyne (-CH) removal (step 34) and hydrogen removal (step 35) from $C_6H_4(O)(OCH)$ intermediate. In the liquid phase environment, the reactions become further competitive, e.g., the difference between the free energy of activation of these two elementary processes in 1-butanol solvent is 0.07 eV. The product of step 34, a catecholate species ($C_6H_4O_2$) then undergoes hydrogenation (step 42) which connects the eighth pathway with the sixth at this point. Product of the other elementary step (step 35), 2-carbide-oxy-phenolate species ($C6H_4(O)(OC)$) then goes through decarbonylation (step 43) to produce 2-oxyphenyl (C_6H_4O) intermediate. While the kinetics of this reaction mostly remains unperturbed due to the presence of a liquid phase, the free energy of reaction becomes more endergonic ($\Delta(\Delta G_{rxn}) = 0.21$ eV) in liquid water while other less protic solvents makes this process more exergonic ($\Delta(\Delta G_{rxn}) = -0.08$ eV). Lastly, the C_6H_4O species gets hydrogenated to phenol (C_6H_5OH) (step 30) and aqueous phase environment facilitates this process both thermodynamically ($\Delta(\Delta G_{rxn}) = -0.12$ eV) and kinetically ($\Delta(\Delta G^{\ddagger}) = -0.09$ eV).

Based on thermodynamics and kinetics of the elementary processes, we can presume that the dominant reaction pathway of the vapor phase (pathway 8) remains dominant in all condensed phase reaction medium. However, any computational catalysis study based on only free energies remains inadequate for not considering the realistic reaction conditions and not predicting the experimental observables which can be compared directly. Therefore, in the following sections, we investigate the effect of solvents on the turn-over frequency (TOF) and the coverage of most abundant surface intermediates through mean-field microkinetic modeling.

4.5.1.3 Mean-field Microkinetic Modeling

In our previous study, we investigated the vapor phase kinetics of HDO of guaiacol over Ru(0001) surface[42] where we found that at low hydrogen partial pressure and moderate reaction temperature (573K), kinetically the most favorable pathway proceeds through dehydrogenation of the hydroxyl group of guaiacol (pathway 8) and the major reaction product was phenol with catechol as the most relevant side product. In this study, we extend our microkinetic model to account for the effect of solvation by including the change in free energy of reaction and free energy of activation due to the presence of a condensed phase. We utilized the experimental reaction conditions of 0.50 g of guaiacol in 10 g of solvent under relatively mild reaction conditions (473 K) and 15 bar partial pressure of H_2, similar to the reaction conditions of Tomishige et al.[36,46] To find the corresponding partial pressure of guaiacol, we utilized the modified Raoult's law,

$$f_{gua}^{v} = P_{gua} = x_{gua}\gamma_{gua}P_{gua}^{sat} \quad (4.16)$$

Thermodynamic data such as activity coefficient, saturation pressure of guaiacol, and fugacity of pure solvent have been calculated using COSMOtherm program package.[73-74] We calculated guaiacol partial pressure to be 0.94 bar at 473 K and assuming a 1% conversion, the phenol partial pressure was set at 9.4×10^{-3} bar. Using low conversion conditions to other reaction products such as catechol, anisole, and benzene, their partial pressures were set at 10^{-6} bar. We chose a slightly higher partial pressure of CO (10^{-4} bar) to observe the poisoning effect of CO on the reaction mechanism, similar to our prior research.[42] For all simulations, we employed the same coverage dependent adsorption energies as reported in our previous contribution[42] for the three most abundant surface intermediates of the vapor phase, H, CO, and phenoxy (C_6H_5O). A summary of our calculated TOFs at four different reaction temperatures and at various reaction environments are presented in Table 4.4.

I. Liquid Water Effects

In the presence of an aqueous phase at 473 K (i.e., at a corresponding equilibrium water partial pressure of 15.536 bar), we observe that the surface is predominantly covered with CH, CO, H, and phenoxy (C_6H_5O) species (Table 4.5). The computed overall TOF decreases by a factor of 2.9 going from the vapor phase ($TOF_{overall\text{-}vapor} = 1.95 \times 10^{-4}$) to an aqueous phase ($TOF_{overall\text{-}water} = 6.70 \times 10^{-5}$). The calculated TOFs along the dominant reaction pathway in different reaction environments are shown in Figure 4.2. The major product in the aqueous phase is predicted to be phenol ($TOF_{phenol} = 6.66 \times 10^{-5}$), similar to the vapor phase.[42] However, unlike the vapor phase where catechol was found to be the major side product, in liquid water we found benzene to be

the major side product with a two order of magnitude lower production rate than that of phenol ($TOF_{benzene} = 4.02 \times 10^{-7}$).

As we have reported previously,[50,75] a fundamental caveat of using a continuum solvation scheme to compute the solvent effects is the uncertainty associated with the cavity radius of transition metal atoms. To account for the uncertainty of Ru atoms, we performed our aqueous phase calculations at three different cavity radii of Ru atoms: the default cavity radius provided by the TURBOMOLE[64] program package (2.223 Å), a 10% increased cavity radius (2.445 Å), and a 10% decreased cavity radius (2.0007 Å). Our microkinetic model results indicated that the usage of different cavity radius does not change the dominant reaction mechanism in an aqueous phase. However, we also observed that the overall TOF lowers by 2 orders of magnitude ($TOF_{water}^{COSMO-10} = 1.35 \times 10^{-7}$) when we decrease the cavity radius of Ru atoms while with a 10% increase, TOF increases by a factor of 1.22 ($TOF_{water}^{COSMO+10} = 8.19 \times 10^{-5}$).

Hellinger et al.[44] studied the solvent effect on HDO of guaiacol over Pt/SiO_2 and Pt/H-MFI 90 catalysts at 450 K and 50 bar hydrogen partial pressure. They surmised that polar solvents lead to lower conversion of HDO of guaiacol due to the oxygen containing solvents being strongly adsorbed on the active sites of the catalysts leading to blockage of active sites,[93] which partly explains our model predicted lower activity of Ru catalysts in aqueous phase. Nakagawa et al.[36] investigated of HDO of guaiacol over Ru/C catalysts in aqueous phase at relatively low temperature (433K) and 15 bar H_2 partial pressure. The major products they observed are phenyl ring saturated products such as cyclohexanol, 2-methoxycyclohexanol, and cyclohexane. Addition of MgO to the reaction media increased the yield of cyclohexanol and methanol. Using the same reaction conditions,

Ishikawa et al.[46] studied HDO of guaiacol over carbon black supported Ru-MnO_x catalyst (Ru-MnO_x/C) and found cyclohexanol and methanol to be the major product. However, in both cases they observed phenol at short reaction times and the selectivity of phenol decreased with guaiacol conversion and cyclohexanol production, which agrees with our calculations of HDO of guaiacol at low conversion conditions.

II. Less Protic Solvent (1-Butanol, Diethyl ether, and n-Hexane) Effects

Microkinetic models for 1-butanol, diethyl ether, and n-hexane were performed under similar reaction conditions except that we employed a water partial pressure similar to our vapor phase simulations ($P_{H_2O} = 10^{-6}$ bar). Our simulations predict a factor two increase in catalytic activity ($TOF_{1-butanol} = 4.66 \times 10^{-4}, TOF_{diethyl\ ether} = 4.33 \times 10^{-4}, TOF_{n-hexane} = 5.17 \times 10^{-4}$) relative to the vapor phase ($TOF_{1-butanol} = 1.95 \times 10^{-4}$) for less protic solvents which agrees with the observation of Hellinger et al.[44] that non polar solvents have a positive effect on the HDO of guaiacol. Except for higher temperatures (>523 K), we found that the presence of a less protic solvent facilitates the phenol production. Chen et al.[76] reported phenol as an intermediate for HDO of guaiacol over Ru/C at 413-533 K and 4 MPa hydrogen partial pressure using ethanol as a solvent, which has a normalized polarity close to that of 1-butanol. Lu et al.[77] investigated the HDO of guaiacol over Ru/TiO_2, Ru/ZrO_2, and Ru supported on TiO_2-ZrO_2 composite oxides at 473-533K and 2 MPa hydrogen partial pressure using a non-polar solvent, n-dodecane as the reaction medium. They found 2-methoxycyclohexanol, cyclohexanol, and phenol to be the major reaction products at low reaction temperature (473K) which partially confirms our microkinetic model predictions.

4.5.1.4 Apparent Activation Barrier, Reaction Orders, and Sensitivity Analysis

We calculated the apparent activation barrier (E_a) and reaction orders ($n_{gua}, n_{CO}, \& n_{H_2}$) (Table 4.6), and performed sensitivity analysis in different reaction environments (Table 4.7). Going from the vapor to an aqueous phase, the estimated apparent activation barrier for the temperature range of 423 K-573 K increases by 0.03 eV which explains the decrease in TOF in liquid water. In less protic solvents such as 1-butanol, diethyl ether, and n-hexane, we predict very similar apparent activation energies of 1.55 eV, 1.57 eV, and 1.58 eV, respectively.

Next, we investigated the dependence of overall TOF on the partial pressures of guaiacol, CO, and H_2, and the results have been summarized in Table 4.6. An increase in partial pressure of guaiacol increases the reaction rate across all reaction environment with the less protic solvents predicting same reaction order for guaiacol (0.12). Site blocking due to increase in CO partial pressure leads to a negative reaction order for CO in all reaction environments where aqueous phase shows the more pronounced effect (n_{co}^{water}= -0.65). We also observed an inhibiting effect of low H_2 partial pressure (0.20 – 0.40 bar) in vapor and aqueous phase environment. However, our model indicated that in other less protic solvents, even at low temperature range, the hydrogen reaction order remains positive. Further increase in partial pressure of hydrogen (0.60 - 20.0 bar) assists the reaction rate in all reaction environments.

To identify the rate controlling steps and surface intermediates, we used Campbell's degree of rate control and degree of thermodynamic rate control[94-96] analyses. Results of the sensitivity analyses are summarized in Table 4.7. We observed that H, CO,

and CH have a poisoning effect on the catalyst due to their high surface coverage in vapor and aqueous phase processing conditions such that destabilizing their adsorption increases the overall reaction rate. In less protic reaction environments, the largest degree of rate controlling species was found to be $C_6H_4O_2$ which has a similar poisoning effect on the surface. Due to the high surface coverage of the CH species in vapor and aqueous phases, our model predicts methyl hydrogenation to methane as one of the rate controlling steps in the reaction mechanism. However, in less protic solvents, dehydrogenation of the hydrogen catecholate species ($C_6H_4(OH)O$) to 2-oxyphenyl (C_6H_4O), which serves as a precursor to phenol production, becomes the most rate controlling reaction such that lowering the activation barrier increases the overall reaction rate. Across all reaction environments, our model predicts that dehydrogenation of 2-methyledyne-oxy-phenolate species ($C_6H_4(O)(OCH)$) to catecholate species ($C_6H_4O_2$) has an inhibiting effect while dehydrogenation to 2-carbide-oxy-phenolate intermediate ($C_6H_4(O)(OC)$) facilitates the overall TOF. Owing to the lack of availability of free sites available for catalysis, our model also predicts a moderate degree of rate control for the guaiacol adsorption process.

4.5.2 Hydrogenation of Phenol to Alicyclic Products

4.5.2.1 Reaction Network

The hydro-upgrading of phenol to cycloalkanes can occur in a number of different ways. Hydrogen addition steps can happen at the α-C (C_1 pathway), ortho- (C_2 pathway), meta- (C_3 pathway), or para- (C_4 pathway) positions of the phenolic ring to produce cyclohexanol and cyclohexanone (Figure 4.4 and Figure 4.5). Furthermore, phenol can

undergo dehydrogenation to produce a phenoxy species and then go through hydrogenation steps to produce cyclohexanone. Cyclohexanone can then undergo keto-enol tautomerization to form cyclohexanol (Keto-enol tautomerization pathway, Figure 4.6). The naming convention employed in the reaction network schemes is as follows: first hydrogenation of the phenyl ring at C_x position leads to the formation of HCX-1 intermediate species [X=1, 2, 3, 4], and subsequent hydrogenated moieties are denoted adding a second integer. Different structures with same number of hydrogenations of phenol are distinguished by adding a letter at the end. For example, HC1-3a (Figure 4.4) refers to an intermediate species in C_1 hydrogenation pathway with three hydrogenations of the phenyl ring, the last of which occurs at the C_5 position, while HC1-3b refers to an adsorbed species of the same pathway with same number of hydrogenations, the last of which happening at C_6 position. Finally, cyclohexanol being a species hydrogenated at all six carbons of phenol is denoted as HC-6 species.

For the keto-enol tautomerization pathway (Figure 4.7), dehydrogenation of phenol at the hydroxyl group leads to the formation of a phenoxy species (KET-1). Subsequent hydrogenated products along the reaction network are denoted using an integer after 'KET', e.g., KET-5d refers the to a phenolate species that has been hydrogenated four times, the last of which occurs at C_6 position. KET-6 (Cyclohexanone) refers to complete hydrogenation of the phenolate species. In total, we investigated 114 elementary steps along the reaction network for phenol hydrogenation to cycloalkanes over Ru(0001) surface. Table C.3 of the supporting information summarizes the free energies of these elementary processes at three different reaction temperatures. In the following sections, we discuss the energetics of these elementary processes in vapor and

condensed phases. Unless otherwise stated, the free energies of reaction and free energies of activation are interpreted at 473 K reaction temperature.

4.5.2.2 Energetics in Vapor Phase

In C_1 pathway, addition of a hydrogen to phenol (step 1) leads to the formation HC1-1 species ($C_6H_5H_\alpha OH$) which is an endergonic process ($\Delta G_{rxn} = 0.41$ eV) and requires overcoming a free energy of activation of 1.16 eV. Subsequent hydrogenation to HC1-2a (step 2, second hydrogenation at the para- position) or HC1-2b (step 3, second hydrogenation at the ortho- position) are both highly endergonic processes with free energies of reaction of 0.85 eV and 0.80 eV, respectively (See Table C.3). In pathway C_2, hydrogenation of phenol (step 37) results in HC2-1 species ($C_6H_5H_{ortho}OH$) which is a thermodynamically and kinetically challenging process ($\Delta G_{rxn} = 0.58$ eV, $\Delta G^{\ddagger} = 1.11$ eV). HC2-1 can then undergo a second hydrogenation step to produce HC2-2a (step 38) or HC2-2b (step 39) which are again thermodynamically demanding processes ($\Delta G_{rxn}^{38} = 0.62$ eV, $\Delta G_{rxn}^{39} = 0.78$ eV).

Hydrogenation of phenol at the meta position (Pathway C_3) leading to the formation of HC3-1 species (step 52) is a kinetically difficult endergonic process ($\Delta G^{\ddagger} = 1.05$ eV). Second hydrogenations of phenol along this reaction pathway to produce HC3-2a or HC3-2b moieties are also endergonic processes with free energies of reaction of 0.72 eV and 0.74 eV, respectively. Along the C_4 pathway, hydrogenation of phenol (step 77) produces HC4-1 ($C_6H_5H_{para}OH$) species which is also an endergonic and kinetically challenging process ($\Delta G_{rxn} = 0.71$ eV, $\Delta G^{\ddagger} = 1.15$ eV).

Finally, in the keto-enol tautomerization pathway (Figure 4.7), the initial O-H scission of phenol at the hydroxyl group (step 80) was found to be a facile exergonic process ($\Delta G_{rxn} = -0.76$ eV, $\Delta G^{\ddagger} = 0.31$ eV). Therefore, it is most likely that phenol at first undergoes to dehydrogenation to form a phenolate species before further hydrogenations. Subsequent hydrogenations of phenolate (KET-1) species to KET-2a (step 81) and KET-2b (step 102) are both thermodynamically challenging processes ($\Delta G_{rxn}^{81} = 0.99$ eV, $\Delta G_{rxn}^{102} = 0.94$ eV). Due to the enormity of the reaction network, we made use of the Evans-Polanyi principle[97] at this stage, which points to the favorability of step 102 over step 81 due to its less endergonicity. Thermodynamics of subsequent hydrogenations of KET-2b species (step 103, 104, 105, and 106) predicts the most thermodynamically favorable pathway to be step 105 to produce KET-3g species ($\Delta G_{rxn} = 0.27$ eV, $\Delta G^{\ddagger} = 0.84$ eV). Next, KET-3g is hydrogenated to KET-4d (step 109) which is an endergonic process with challenging kinetics ($\Delta G_{rxn} = 0.42$ eV, $\Delta G^{\ddagger} = 1.06$ eV). KET-4d intermediate, which is the same as KET-4b, is subsequently hydrogenated to KET-5c (step 92) or KET-5d (step 93), of which the former is thermodynamically more favorable ($\Delta G_{rxn}^{92} = 0.17$ eV, $\Delta G_{rxn}^{93} = 0.82$ eV) with a free energy of activation of 1.07 eV. KET-5c then undergoes hydrogenation (step 96) to produce KET-6 (Cyclohexanone) with a moderately endergonic reaction free energy ($\Delta G_{rxn} = 0.32$ eV) and a high free energy of activation ($\Delta G^{\ddagger} = 1.21$ eV). KET-6 finally undergoes hydrogenation at the hydroxyl group to form KET-7a (step 98) and subsequently hydrogenated (step 100) to produce HC-6 (Cyclohexanol). Although kinetically very demanding, on the basis of these energetics calculations alone, the likely pathway to produce cyclohexanol from phenol proceeds through,

$\text{Phenol} \rightarrow \text{KET} - 1 \rightarrow \text{KET} - 2\text{b} \rightarrow \text{KET} - 3\text{g} \rightarrow \text{KET} - 4\text{b} \rightarrow \text{KET} - 5\text{c} \rightarrow \text{KET} - 6 \rightarrow \text{KET} - 7\text{a} \rightarrow \text{HC} - 6$. This probable pathway is highlighted in figure 4.6. Next, we look into the condensed phase effects on this more likely path to understand if the presence of solvent causes the difference.

4.5.2.3 Energetics in Liquid Phase

Table 4.8 summarizes the thermodynamics and kinetics of the important elementary surface processes for hydrogenation of phenol at various reaction environments. Presence of a solvent barely affects the thermodynamics or the kinetics of phenolate (KET-1) production from phenol (step 80) or the subsequent hydrogenation steps to form KET-2b species (step 102) and KET-3g species (step 105). However, liquid water reduces the free energy of activation of the next hydrogenation step to produce KET-4d/b species (step 109) by 0.13 eV where the non-polar aprotic n-hexane demonstrates less dramatic effect. Introduction of a liquid phase environment also facilitates the subsequent hydrogenation of KET-4b to KET-5c (step 92), with water displaying the largest facilitating effect ($\Delta\left(\Delta G^{\ddagger}_{\text{water}}\right) = -0.17$ eV). KET-5c then undergoes hydrogenation to produce KET-6 species (step 96) where condensed phases have a nominal effect on the thermodynamics of the reaction. However, the reaction become more facile in the liquid phase, with liquid water reducing the free energy of activation by 0.17 eV. The thermodynamics and kinetics of the final two subsequent hydrogenation steps (step 98 & 100) are minimally affected by the presence of a condensed phase. Overall, addition of a liquid phase reaction media facilitates the likely pathway proposed in the previous section with liquid water liquid water exhibiting the

largest facilitating effect which compare favorably with the observation of Zhong et al.[92] However, the kinetics of some of these elementary processes (Table 4.8) still remains very demanding.

4.6 Conclusion

Solvent influence on the hydrodeoxygenation of guaiacol over Ru(0001) model surface has been investigated in a two-step fashion by means of periodic and non-periodic DFT calculations, implicit solvation calculations with the iSMS scheme, and microkinetic modeling. In the first step, we examined the formation of unsaturated aromatic products such as phenol, anisole, catechol etc. from guaiacol. We developed mean-field microkinetic reactor models at different temperatures and experimental reaction conditions.[36,46] Under all reaction environments and reaction conditions, we found the same dominating HDO mechanism with the most favored pathway following the initial dehydrogenation at the hydroxyl group of guaiacol, followed by complete dehydrogenation of the methoxy group and subsequent decarbonylation, which then undergoes two subsequent hydrogenations to produce phenol. Less protic solvents such as 1-butanol, diethyl ether, and n-hexane demonstrates higher HDO ability compared to that of vapor and aqueous phases which is qualitatively in good agreement with the experimental results.[44] After verifying the presence of phenol, which is often referred to as a 'short-lived intermediate', we investigated the production of cycloalkanes through phenol hydrogenation in vapor and condensed phases. We observed that dehydrogenation of phenol to a phenolate species (keto-enol tautomerization pathway) is the most likely pathway to produce cyclohexanol and cyclohexanone from phenol. Based on the vapor phase first-principles calculations, we proposed a plausible pathway for cycloalkane

formation. Next, we investigated the solvent effects on this probable reaction pathway and demonstrated a facilitating effect of the aqueous phase along the proposed reaction mechanism which is in line with experimental observations.[98] Therefore, our study addresses a crucial issue, how the presence of a condensed phase affects the hydrogenation of aromatic rings on Ru catalysts. We should note here that the proposed pathway still remains kinetically very challenging and it is possible that the cyclohexanone and cyclohexanol production follows a different reaction route along the keto-enol tautomerization pathway. Investigations have also shown that the support plays a major role in the hydrogenation of phenol which might also facilitate the kinetics of the reactions along the hypothesized reaction mechanism.[89] However, a full computational investigation of phenol hydrogenation is out of the scope of the present study and we encourage further computational investigations on phenol hydrogenation for the production of cycloalkanes.

4.7 Acknowledgements

We gratefully acknowledge the financial support of United States Department of Energy, Office of Basic Energy Sciences (DE-SC0007167). Computing resources provided by the National Energy Research Scientific Computing Center (NERSC), Texas Advanced Computing Center (TACC), and Pacific Northwest National Laboratory (PNNL) are gratefully acknowledged.

4.8 Tables and Figures

Table 4.1: Solvent effects on the adsorption strength of various surface intermediates in the HDO of Guaiacol over Ru(0001) model surface at 473 K temperature.

Surface Intermediates	Water Δ(ΔG) (eV)	1-Butanol Δ(ΔG) (eV)	Diethyl ether Δ(ΔG) (eV)	n-Hexane Δ(ΔG) (eV)
$C_6H_4(OH)(OCH_3)$	-0.22	-0.47	-0.43	-0.33
$C_6H_4H_\beta(OH)(OCH_3)$	-0.18	-0.36	-0.34	-0.25
$C_6H_4H_\alpha(OH)(OCH_3)$	-0.19	-0.53	-0.50	-0.39
$C_6H_4OCH_3$	-0.07	-0.35	-0.33	-0.24
C_6H_4OH	-0.20	-0.33	-0.31	-0.22
$C_6H_4(OH)(OCH_2)$	-0.15	-0.43	-0.40	-0.30
$C_6H_4(OH)(O)$	-0.22	-0.26	-0.23	-0.15
$C_6H_4(O)(OCH_3)$	-0.16	-0.35	-0.31	-0.22
$C_6H_4H_\beta(OH)(OCH_2)$	-0.37	-0.38	-0.35	-0.26
$C_6H_5OCH_3$	-0.25	-0.41	-0.38	-0.29
$C_6H_4(OH)(OCH)$	-0.17	-0.44	-0.41	-0.30
$C_6H_4(OH)_2$	-0.22	-0.39	-0.36	-0.25
C_6H_4O	-0.05	-0.33	-0.31	-0.22
$C_6H_4(O)(OCH_2)$	-0.14	-0.29	-0.25	-0.17
$C_6H_4H_\beta(OH)(O)$	-0.19	-0.33	-0.29	-0.20
$C_6H_5OCH_2$	-0.17	-0.32	-0.28	-0.19
C_6H_5O	-0.13	-0.32	-0.29	-0.20
C_6H_5OH	-0.20	-0.38	-0.35	-0.26
$C_6H_5(OH)_2$	-0.14	-0.28	-0.25	-0.18
$C_6H_4O_2$	-0.26	-0.34	-0.31	-0.23
C_6H_5	-0.14	-0.31	-0.29	-0.21
C_6H_6OH	-0.22	-0.28	-0.25	-0.17
C_6H_6	-0.11	-0.26	-0.24	-0.17
$C_6H_4H\alpha(O)(OH)$	-0.19	-0.27	-0.24	-0.17
$C_6H_4(O)(OCH)$	-0.18	-0.34	-0.32	-0.24
$C_6H_4(O)(OC)$	-0.27	-0.32	-0.29	-0.20
H	0.04	0.01	0.01	0.01
OH	0.04	-0.02	-0.02	0.01
H_2O	0.01	-0.10	-0.09	-0.05
CH	-0.05	-0.02	-0.01	0.01
CH_2	0.02	-0.02	-0.01	0.00
CH_3	0.11	-0.01	-0.01	0.00
CH_4	0.04	-0.03	-0.03	-0.03
CO	0.00	-0.06	-0.06	-0.04
CHO	0.02	-0.04	-0.04	-0.01
CH_2O	-0.02	-0.03	-0.02	0.00

CH_3O	0.09	-0.07	-0.06	-0.04
CH_3OH	0.12	-0.10	-0.09	-0.05

Table 4.2: Energetics of adsorption-desorption reactions (in eV) for HDO of guaiacol in the limit of zero coverage at 473 K temperature under different reaction environments.

ID	Reaction	Vapor phase, ΔG_{rxn}	Water, ΔG_{rxn}	1-Butanol, ΔG_{rxn}	Diethyl ether, ΔG_{rxn}	n-Hexane, ΔG_{rxn}
1	$C_6H_4(OH)(OCH_3)$ (gas) + 4* ↔ $C_6H_4(OH)(OCH_3)$ ****	-0.29	-0.51	-0.75	-0.72	-0.62
53	$C_6H_5(OCH_3)$**** ↔ $C_6H_5(OCH_3)$ (gas) + 4*	0.35	0.60	0.75	0.73	0.64
54	$C_6H_4(OH)_2$**** ↔ $C_6H_4(OH)_2$(gas) + 4*	0.41	0.63	0.80	0.77	0.66
55	C_6H_5OH**** ↔ C_6H_5OH (gas) + 4*	0.45	0.65	0.83	0.80	0.71
56	C_6H_6*** ↔ C_6H_6(gas) + 3*	0.47	0.58	0.72	0.70	0.64
57	CH_4* ↔ CH_4(gas) + *	-0.39	-0.43	-0.36	-0.36	-0.36
58	CH_3OH* ↔ CH_3OH (gas) + *	-0.38	-0.50	-0.28	-0.29	-0.33
59	H_2O* ↔ H_2O (gas) + *	-0.33	-0.34	-0.23	-0.24	-0.28
60	CO* ↔ CO (gas) + *	0.96	0.96	1.02	1.01	1.00
53	H* ↔ 0.5H_2 (gas) + *	0.18	0.22	0.19	0.19	0.19

Table 4.3: Energetics of all elementary surface reaction steps (in eV) for HDO of guaiacol to unsaturated aromatics in the limit of zero coverage at 473 K temperature in the presence of liquid water, 1-butanol, diethyl ether, and n-hexane solvents.

ID	Reaction	Vapor phase		Water		1-Burtanol		Diethyl ether		n-Hexane	
		ΔG_{rxn}	$\Delta G^{\ddagger}$	ΔG_{rxn}	$\Delta G^{\ddagger}$	ΔG_{rxn}	$\Delta G^{\ddagger}$	ΔG_{rxn}	$\Delta G^{\ddagger}$	ΔG_{rxn}	$\Delta G^{\ddagger}$
2	$C_6H_4(OH)(OCH_3)$**** + H* ↔ $C_6H_4H_\beta(OH)(OCH_3)$**** + *	0.40	1.10	0.41	1.12	0.49	1.27	0.48	1.28	0.47	1.25
3	$C_6H_4(OH)(OCH_3)$ **** + H* ↔ $C_6H_4H_\alpha(OH)(OCH_3)$**** + *	0.51	1.14	0.51	1.18	0.43	1.20	0.44	1.20	0.45	1.21
4	$C_6H_4(OH)(OCH_3)$**** + * ↔ $C_6H_4(OCH_3)$**** + OH*	-0.22	1.06	-0.03	1.13	-0.13	1.06	-0.13	1.06	-0.12	1.07
5	$C_6H_4(OH)(OCH_3)$**** + * ↔ C_6H_4OH**** + CH_3O*	-0.49	0.88	-0.37	0.95	-0.43	0.89	-0.42	0.90	-0.42	0.90
6	$C_6H_4(OH)(OCH_3)$**** + 2* ↔ $C_6H_4(OH)(OCH_2)$***** + H*	-0.36	0.50	-0.25	0.52	-0.32	0.51	-0.32	0.51	-0.32	0.51
7	$C_6H_4(OH)(OCH_3)$**** + * ↔ $C_6H_4(OH)(O)$**** + CH_3*	-1.35	1.40	-1.23	1.43	-1.15	1.36	-1.15	1.37	-1.17	1.38
8	$C_6H_4(OH)(OCH_3)$**** + * ↔ $C_6H_4(O)(OCH_3)$**** + H*	-0.77	0.29	-0.67	0.37	-0.65	0.29	-0.64	0.29	-0.65	0.31
9	$C_6H_4H_\beta(OH)(OCH_3)$**** + 2* ↔ $C_6H_4H_\beta(OH)(OCH_2)$**** + H*	-0.12	0.93	-0.27	0.81	-0.13	0.91	-0.12	0.92	-0.12	0.93
10	$C_6H_4H_\beta(OH)(OCH_3)$**** + * ↔ C_6H_5OH**** + CH_3O*	-1.05	0.72	-0.97	0.61	-1.13	0.66	-1.12	0.67	-1.10	0.68
11	$C_6H_4H_\alpha(OH)(OCH_3)$**** + * ↔ $C_6H_5(OCH_3)$**** + OH*	-0.91	0.57	-0.93	0.59	-0.81	0.70	-0.81	0.70	-0.81	0.68
12	$C_6H_4(OCH_3)$**** + H* ↔ $C_6H_5(OCH_3)$**** + *	-0.18	0.64	-0.40	0.58	-0.25	0.55	-0.25	0.55	-0.24	0.56
13	C_6H_4OH**** + H* ↔ C_6H_5OH**** + *	-0.16	0.62	-0.20	0.59	-0.22	0.61	-0.21	0.61	-0.21	0.60
14	$C_6H_4(OH)(OCH_2)$***** + * ↔ C_6H_4OH**** + CH_2O**	-0.25	1.23	-0.33	1.10	-0.19	1.34	-0.19	1.33	-0.18	1.32
15	$C_6H_4(OH)(OCH_2)$***** + * ↔ $C_6H_4(O)(OCH_2)$***** + H*	-0.73	0.28	-0.69	0.31	-0.58	0.32	-0.58	0.32	-0.59	0.31
16	$C_6H_4(OH)(OCH_2)$***** + * ↔ $C_6H_4(OH)(OCH)$***** + H*	-0.53	0.02	-0.52	0.00	-0.53	0.12	-0.53	0.12	-0.53	0.11
17	$C_6H_4(OH)(OCH_2)$***** ↔ $C_6H_4(OH)(O)$**** + CH_2*	-1.25	0.42	-1.30	0.43	-1.10	0.40	-1.10	0.40	-1.11	0.41

18	$C_6H_4(OH)(O)^{****} + H^* \leftrightarrow C_6H_4(OH)_2^{****} + *$	0.75	1.03	0.71	1.03	0.61	0.92	0.61	0.92	0.64	0.93
19	$C_6H_4(OH)(O)^{****} + H^* \leftrightarrow C_6H_4H_\alpha(OH)(O)^{****} + *$	0.89	1.40	0.87	1.47	0.86	1.37	0.86	1.37	0.85	1.38
20	$C_6H_4(OH)(O)^{****} + * \leftrightarrow C_6H_4O^{****} + OH^*$	0.51	1.15	0.72	1.11	0.41	1.14	0.42	1.14	0.45	1.15
21	$C_6H_4(O)(OCH_3)^{****} + * \leftrightarrow C_6H_4O^{****} + CH_3O^*$	0.21	1.08	0.32	1.04	0.16	1.15	0.17	1.16	0.19	1.16
22	$C_6H_4(O)(OCH_3)^{****} + 2^* \leftrightarrow C_6H_4(O)(OCH_2)^{*****} + H^*$	-0.32	0.53	-0.27	0.47	-0.25	0.52	-0.25	0.51	-0.26	0.51
23	$C_6H_4H_\beta(OH)(OCH_2)^{****} * \leftrightarrow C_6H_4H_\beta(OH)(O)^{****} + CH_2^*$	-0.84	0.39	-0.65	0.55	-0.81	0.39	-0.80	0.40	-0.79	0.41
24	$C_6H_5(OCH_3)^{****} + * \leftrightarrow C_6H_5(OCH_2)^{****} + H^*$	-0.32	0.51	-0.20	0.52	-0.22	0.55	-0.21	0.56	-0.21	0.57
25	$C_6H_4(OH)(OCH)^{*****} + * \leftrightarrow C_6H_4OH^{****} + CHO^{**}$	-0.26	1.00	-0.27	0.99	-0.20	0.95	-0.20	0.95	-0.20	0.95
26	$C_6H_4(OH)(OCH)^{*****} \leftrightarrow C_6H_4(OH)(O)^{****} + CH^*$	-1.29	0.31	-1.38	0.31	-1.12	0.32	-1.12	0.33	-1.13	0.34
27	$C_6H_4(OH)_2^{****} + * \leftrightarrow C_6H_4OH^{****} + OH^*$	-0.16	1.16	-0.09	1.09	-0.13	1.16	-0.13	1.16	-0.13	1.15
28	$C_6H_4(OH)_2^{****} + H^* \leftrightarrow C_6H_5(OH)_2^{****} + *$	0.55	1.15	0.59	1.25	0.65	1.19	0.65	1.19	0.62	1.17
29	$C_6H_4H_\alpha(OH)(O)^{****} + * \leftrightarrow C_6H_5O^{****} + OH^*$	-1.29	0.76	-1.20	0.74	-1.37	0.73	-1.36	0.73	-1.31	0.74
30	$C_6H_4O^{****} + H^* \leftrightarrow C_6H_5O^{****} + *$	-0.92	0.52	-1.04	0.43	-0.92	0.44	-0.91	0.45	-0.91	0.46
31	$C_6H_4(O)(OCH_2)^{*****} + * \leftrightarrow C_6H_4O^{****} + CH_2O^{**}$	0.40	1.03	0.46	1.01	0.32	1.02	0.32	1.02	0.34	1.01
32	$C_6H_4(O)(OCH_2)^{*****} + * \leftrightarrow C_6H_4O_2^{*****} + CH_2^*$	-0.95	0.52	-1.05	0.50	-1.02	0.51	-1.02	0.51	-1.01	0.50
33	$C_6H_4(O)(OCH_2)^{*****} + * \leftrightarrow C_6H_4(O)(OCH)^{*****} + H^*$	-0.52	0.02	-0.52	0.02	-0.57	0.00	-0.57	0.00	-0.58	0.00
34	$C_6H_4(O)(OCH)^{*****} + * \leftrightarrow C_6H_4O_2^{*****} + CH^*$	-1.00	0.50	-1.13	0.52	-1.02	0.51	-1.01	0.53	-0.98	0.54
35	$C_6H_4(O)(OCH)^{*****} + * \leftrightarrow C_6H_4(O)(OC)^{*****} + H^*$	-0.34	0.40	-0.39	0.41	-0.31	0.45	-0.30	0.46	-0.29	0.47
36	$C_6H_4H_\beta(OH)(O)^{****} + H^* \leftrightarrow C_6H_5(OH)_2^{****} + *$	0.25	0.91	0.26	0.94	0.29	0.92	0.28	0.92	0.27	0.92
37	$C_6H_5(OCH_2)^{****} + * \leftrightarrow C_6H_5O^{****} + CH_2^*$	-1.30	0.18	-1.24	0.16	-1.32	0.24	-1.32	0.23	-1.31	0.23
38	$C_6H_5O^{****} + H^* \leftrightarrow C_6H_5OH^{****} + *$	0.84	1.03	0.73	1.00	0.77	1.04	0.76	1.04	0.77	1.03
39	$C_6H_5OH^{****} + * \leftrightarrow C_6H_5^{****} + OH^*$	-0.10	1.17	-0.01	1.09	-0.07	1.21	-0.06	1.21	-0.05	1.20
40	$C_6H_5OH^{****} + H^* \leftrightarrow C_6H_6OH^{****} + *$	0.59	1.25	0.53	1.21	0.67	1.34	0.67	1.34	0.67	1.33
41	$C_6H_5(OH)_2^{****} + * \leftrightarrow C_6H_5OH^{****} + OH^*$	-0.87	0.56	-0.89	0.57	-0.99	0.41	-0.99	0.41	-0.95	0.45
42	$C_6H_4O_2^{*****} + H^* \leftrightarrow C_6H_4(OH)(O)^{****} + 2^*$	0.43	0.95	0.44	0.97	0.50	0.95	0.51	0.95	0.50	0.95

43	$C_6H_4(O)(OC)^{*****} \leftrightarrow C_6H_4O^{****} + CO^*$	-0.49	0.66	-0.28	0.70	-0.57	0.69	-0.57	0.70	-0.55	0.69
44	$C_6H_5^{****} + H^* \leftrightarrow C_6H_6^{***} + 2^*$	-0.20	0.54	-0.21	0.56	-0.15	0.53	-0.15	0.54	-0.17	0.55
45	$C_6H_6OH^{****} \leftrightarrow C_6H_6^{***} + OH^*$	-0.89	0.53	-0.74	0.59	-0.88	0.55	-0.89	0.54	-0.88	0.54
46	$CH^* + H^* \leftrightarrow CH_2^* + *$	0.57	0.61	0.60	0.60	0.56	0.18	0.56	0.21	0.56	0.35
47	$CH_2^* + H^* \leftrightarrow CH_3^* + *$	0.27	0.62	0.31	0.61	0.26	0.31	0.26	0.33	0.26	0.39
48	$CH_3^* + H^* \leftrightarrow CH_4^* + *$	0.43	1.03	0.32	1.08	0.40	0.62	0.39	0.65	0.40	0.75
49	$OH^* + H^* \leftrightarrow H_2O^* + *$	0.48	1.13	0.41	1.04	0.39	1.11	0.40	1.11	0.42	1.12
50	$CHO^{**} + H^* \leftrightarrow CH_2O^{**} + *$	0.54	0.51	0.46	0.48	0.54	0.50	0.55	0.50	0.54	0.50
51	$CH_2O^{**} + H^* \leftrightarrow CH_3O^* + 2^*$	0.13	0.69	0.21	0.71	0.08	0.68	0.08	0.67	0.08	0.67
52	$CH_3O^* + H^* \leftrightarrow CH_3OH^* + *$	0.71	1.21	0.69	1.16	0.67	1.23	0.67	1.23	0.69	1.23

Table 4.4: Computed overall turnover frequencies at various reaction temperatures and 15 bar partial pressure of hydrogen for HDO of guaiacol over Ru(0001) surface. Microkinetic models have been simulated for 1% conversion of guaiacol using 0.5 g guaiacol in 10 g of different solvent medium.

TOF (s^{-1})	Temperature			
	423 K	473 K	523 K	573 K
Vapor phase	6.46×10^{-7}	1.95×10^{-4}	4.31×10^{-2}	2.35
Water	1.54×10^{-7}	6.70×10^{-5}	3.25×10^{-2}	4.82×10^{-1}
1-Butanol	4.64×10^{-6}	4.66×10^{-4}	1.76×10^{-2}	3.08×10^{-1}
Diethyl ether	4.07×10^{-6}	4.33×10^{-4}	1.80×10^{-2}	2.98×10^{-1}
n-Hexane	4.94×10^{-6}	5.17×10^{-4}	2.34×10^{-2}	4.14×10^{-1}

Table 4.5: Coverages (%) of most abundant surface intermediates in various reaction environments for HDO of guaiacol at 473K temperature.

Surface Intermediates	Vapor phase	Water	1-Butanol	Diethyl ether	n-Hexane
θ^*	0.13	0.10	0.39	0.41	0.35
θ^*_H	7.04	11.73	11.42	11.49	11.03
θ^*_{CO}	28.17	25.78	29.96	30.09	29.65
θ^*_{CH}	62.75	60.20	0.03	0.05	0.34
θ^*_{C6H4O2}	0.65	0.10	46.7	48.45	51.20
$\theta^*_{Phenoxy}$	0.76	1.84	9.72	8.24	5.68

Table 4.6: Kinetic parameters computed at 473 K for HDO of guaiacol over Ru(0001) model surface at low conversion conditions under various reaction environments.

Properties	Partial pressure (bar)	Vapor phase	Water	1-Butanol	Diethyl ether	n-Hexane
Apparent Activation Energy(eV)	-	2.12	2.15	1.55	1.57	1.58
Guaiacol order	0.20 - 10.0	0.17	0.20	0.12	0.12	0.12
Carbon monoxide order	1.0×10^{-5}- 1.0×10^{-1}	-0.51	-0.65	-0.18	-0.18	-0.18
Hydrogen order	0.20 – 0.40	-1.18	-4.02	0.68	0.59	0.42
	0.60-20.0	1.74	1.62	0.46	0.46	0.08

Table 4.7: Thermodynamic and kinetic sensitivity analysis at 473 K for HDO of guaiacol over Ru(0001) model surface.

Degree of thermodynamic rate control					
Species	Vapor	Water	1-Butanol	Diethyl ether	n-Hexane
H*	-0.94	-0.35	-0.60	-0.66	-0.55
CO*	-0.63	-0.79	-0.18	-0.20	-0.21
CH*	-0.90	-0.86	0.00	0.00	0.00
$C_6H_4O_2$*****	-0.01	0.00	-0.80	-0.82	-0.82
Degree of kinetic rate control					
$C_6H_4(OH)(OCH_3)$ (gas) + 4* ↔ $C_6H_4(OH)(OCH_3)$****	0.15	0.20	0.16	0.16	0.16
$C_6H_4(OH)(O)$**** + * ↔ C_6H_4O**** + OH*	-0.01	0.01	0.77	0.80	0.82
$C_6H_4(O)(OCH)$***** + * ↔ $C_6H_4O_2$***** + CH*	-0.72	-0.75	-0.60	-0.61	-0.64
$C_6H_4(O)(OCH)$***** + * ↔ $C_6H_4(O)(OC)$***** + H*	0.74	0.73	0.57	0.58	0.61
CH_3* + H* ↔ CH_4* + *	0.84	0.86	0.00	0.00	0.01

Table 4.8: Energetics of important elementary surface reaction steps (in eV) in the limit of zero coverage at 473 K temperature in the presence of liquid water, 1-butanol, diethyl ether, and n-hexane solvents for phenol hydrogenation to cyclohexanol.

ID	Reaction	Vapor phase		Water		1-Burtanol		Diethyl ether		n-Hexane	
		ΔG_{rxn}	$\Delta G^{\ddagger}$	ΔG_{rxn}	$\Delta G^{\ddagger}$	ΔG_{rxn}	$\Delta G^{\ddagger}$	ΔG_{rxn}	$\Delta G^{\ddagger}$	ΔG_{rxn}	$\Delta G^{\ddagger}$
1	Phenol**** + H* ↔ HC1-1**** + *	0.41	1.16	-	-	-	-	-	-	-	-
37	Phenol**** + H* ↔ HC2-1**** + *	0.58	1.11	-	-	-	-	-	-	-	-
52	Phenol**** + H* ↔ HC3-1**** + *	0.51	1.05	-	-	-	-	-	-	-	-
77	Phenol**** + H* ↔ HC4-1**** + *	0.71	1.15	-	-	-	-	-	-	-	-
80	Phenol**** + * ↔ KET-1**** + H*	-0.76	0.31	-0.77	0.34	-0.75	0.32	-0.75	0.32	-0.75	0.31
92	KET-4b**** + H* ↔ KET-5c**** + *	0.17	1.07	0.12	0.90	0.10	0.97	0.10	0.98	0.10	0.99
96	KET-5c**** + H* ↔ KET-6**** + *	0.32	1.21	0.23	1.04	0.24	1.15	0.24	1.17	0.24	1.18
98	KET-6**** + H* ↔ KET-7a**** + *	0.60	1.22	0.57	1.17	0.59	1.24	0.59	1.25	0.59	1.26
100	KET-7a**** + H* ↔ HC-6**** + *	-0.11	1.17	-0.13	1.09	-0.14	1.10	-0.13	1.11	-0.13	1.11
102	KET-1**** + H* ↔ KET-2b**** + *	0.94	1.14	0.90	1.21	0.90	1.14	0.90	1.13	0.90	1.12
105	KET-2b**** + H* ↔ KET-3g**** + *	0.27	0.84	0.24	0.86	0.23	0.81	0.23	0.80	0.23	0.80
109	KET-3g**** + H* ↔ KET-4d**** (=KET-4b****) + *	0.42	1.06	0.44	0.93	0.44	0.95	0.44	0.96	0.43	1.02

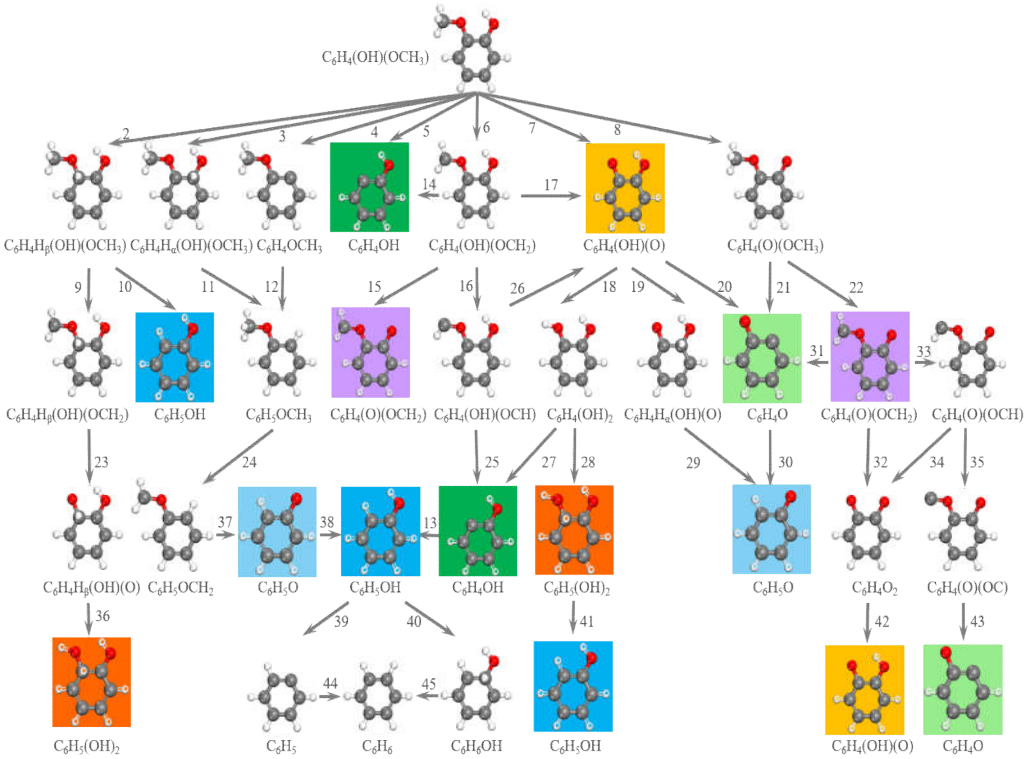

Figure 4.1: Reaction network investigated for the hydrodeoxygenation of guaiacol over Ru(0001) model surface. Duplicate structures are highlighted by identical background colors.

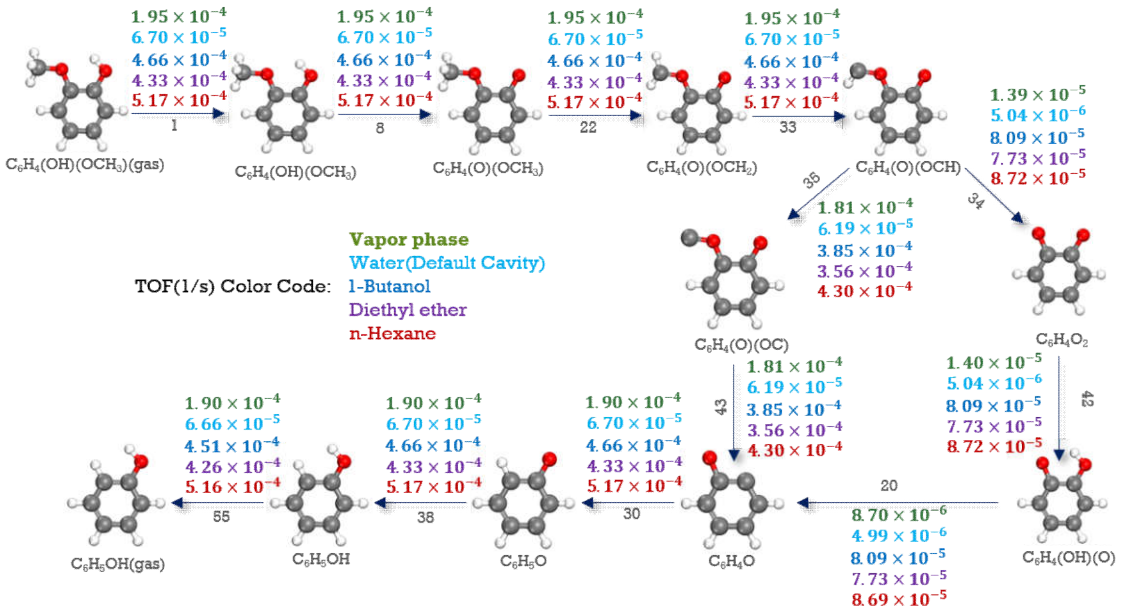

Figure 4.2: Turnover frequencies (1/s) along the dominant reaction pathway for HDO of guaiacol to unsaturated aromatic products over Ru(0001) surface computed in different reaction environments.

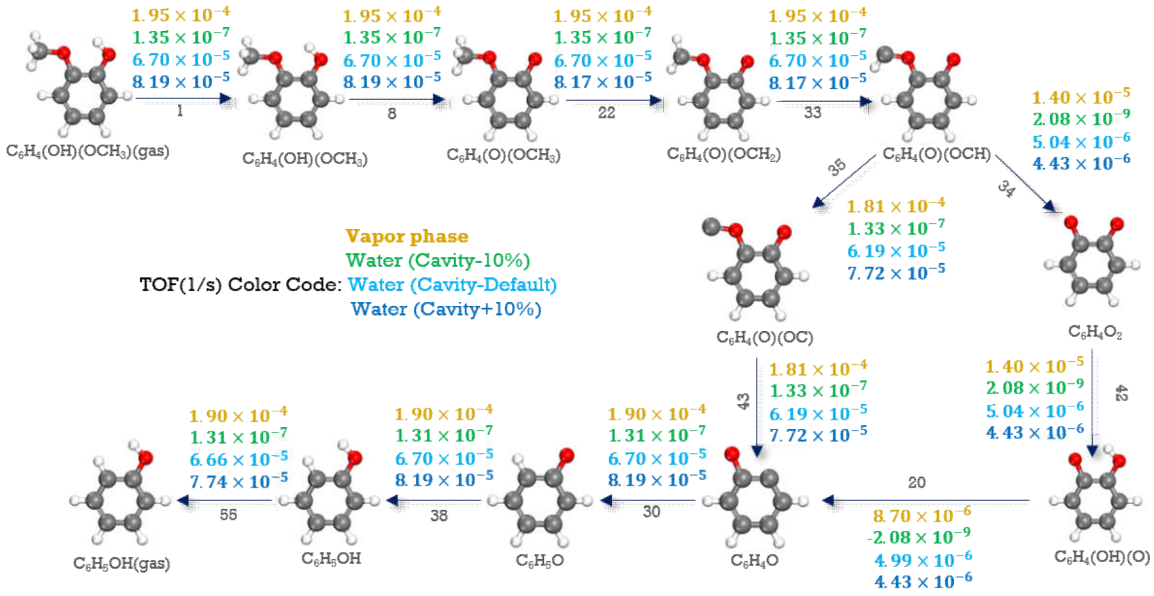

Figure 4.3: Turnover frequencies (1/s) along the dominant reaction pathway for HDO of guaiacol to unsaturated aromatic products over Ru(0001) surface in vapor and aqueous phases. Aqueous phase calculations have been performed using three different cavity radius of Ru atoms.

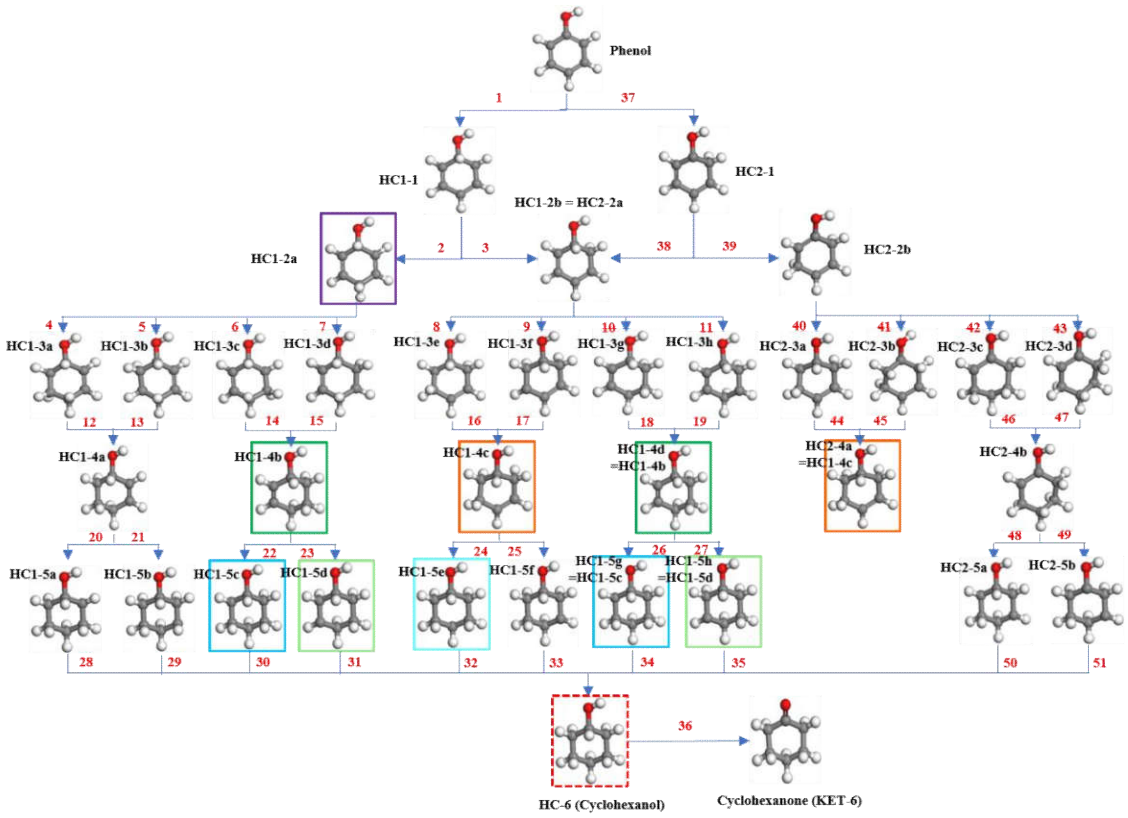

Figure 4.4: Reaction network investigated along the C_1 and C_2 hydrogenation pathway of phenol over Ru(0001) model surface. Duplicate structures have been highlighted by identical border colors.

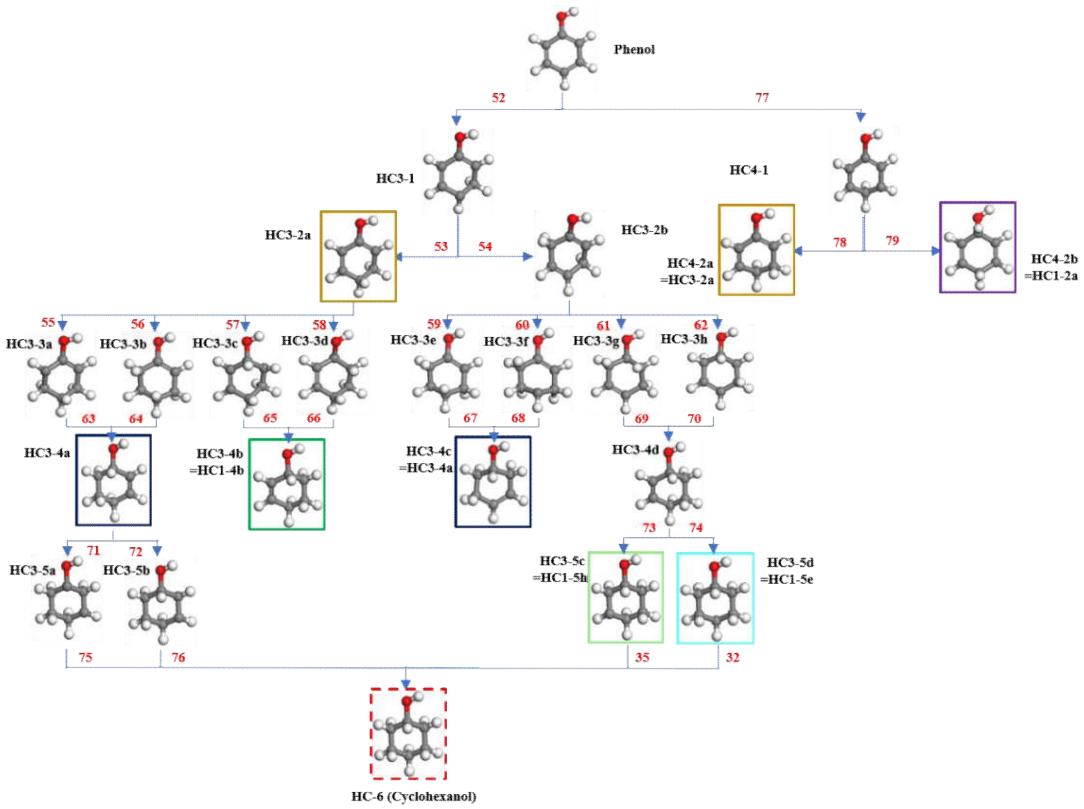

Figure 4.5: Reaction network investigated along the C_3 and C_4 hydrogenation pathway of phenol over Ru(0001) model surface. Duplicate structures have been highlighted by identical border colors.

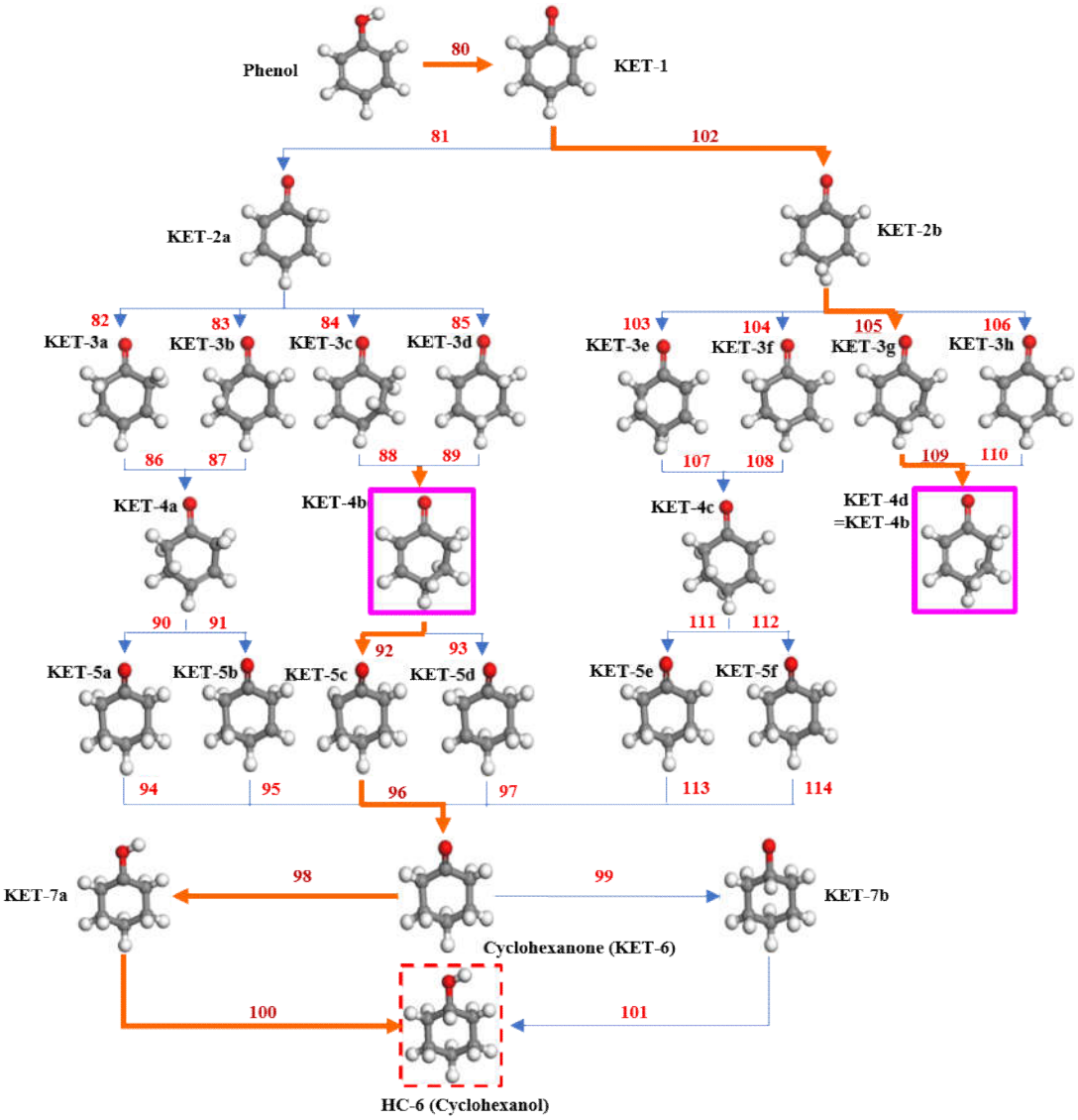

Figure 4.6: Reaction network investigated along the keto-enol tautomerization pathway of phenol over Ru(0001) model surface. Duplicate structures have been highlighted by identical border colors. Proposed reaction mechanism and the reaction steps involved for cycloalkane production from phenol have also been highlighted.

4.9 Bibliography

1. Li, Z.; Han, C.; Gu, T. Economics of biomass gasification: A review of the current status. *Energy Sources, Part B: Economics, Planning, and Policy* **2018,** *13*, 137-140.

2. Popp, J.; Lakner, Z.; Harangi-Rakos, M.; Fari, M. The effect of bioenergy expansion: Food, energy, and environment. *Renew Sust Energ Rev* **2014,** *32*, 559-578.

3. Carriquiry, M. A.; Du, X. D.; Timilsina, G. R. Second generation biofuels: Economics and policies. *Energ Policy* **2011,** *39*, 4222-4234.

4. Chheda, J. N.; Huber, G. W.; Dumesic, J. A. Liquid-phase catalytic processing of biomass-derived oxygenated hydrocarbons to fuels and chemicals. *Angewandte Chemie-International Edition* **2007,** *46*, 7164-7183.

5. Alonso, D. M.; Bond, J. Q.; Dumesic, J. A. Catalytic conversion of biomass to biofuels. *Green Chem* **2010,** *12*, 1493-1513.

6. Serrano-Ruiz, J. C.; Dumesic, J. A. Catalytic routes for the conversion of biomass into liquid hydrocarbon transportation fuels. *Energ Environ Sci* **2011,** *4*, 83-99.

7. Xiu, S. N.; Shahbazi, A. Bio-oil production and upgrading research: A review. *Renew Sust Energ Rev* **2012,** *16*, 4406-4414.

8. Furimsky, E. Catalytic hydrodeoxygenation. *Appl Catal a-Gen* **2000,** *199*, 147-190.

9. Honkela, M. L.; Viljava, T.-R.; Gutierrez, A.; Krause, A. O. I. In *Rsc Energy Environ S*, The Royal Society of Chemistry: 2010; pp 288-306.

10. Elliott, D. C.; Hart, T. R. Catalytic Hydroprocessing of Chemical Models for Bio-oil. *Energ Fuel* **2009,** *23*, 631-637.

11. Popov, A.; Kondratieva, E.; Mariey, L.; Goupil, J. M.; El Fallah, J.; Gilson, J. P.; Travert, A.; Mauge, F. Bio-oil hydrodeoxygenation: Adsorption of phenolic compounds on sulfided (Co)Mo catalysts. *J Catal* **2013,** *297*, 176-186.

12. Zhang, S. P.; Yan, Y. J.; Li, T. C.; Ren, Z. W. Upgrading of liquid fuel from the pyrolysis of biomass. *Bioresource Technol* **2005,** *96*, 545-550.

13. Wildschut, J.; Mahfud, F. H.; Venderbosch, R. H.; Heeres, H. J. Hydrotreatment of Fast Pyrolysis Oil Using Heterogeneous Noble-Metal Catalysts. *Ind Eng Chem Res* **2009,** *48*, 10324-10334.

14. Viljava, T. R.; Komulainen, S.; Selvam, T.; Krause, A. O. I. Stability of CoMo/Al2O3 catalysts: Effect of HDO cycles on HDS. *Stud Surf Sci Catal* **1999,** *127*, 145-152.

15. Viljava, T. R.; Komulainen, R. S.; Krause, A. O. I. Effect of H2S on the stability of CoMo/Al2O3 catalysts during hydrodeoxygenation. *Catal Today* **2000,** *60*, 83-92.

16. Gutierrez, A.; Kaila, R. K.; Honkela, M. L.; Slioor, R.; Krause, A. O. I. Hydrodeoxygenation of guaiacol on noble metal catalysts. *Catal Today* **2009,** *147*, 239-246.

17. Furimsky, E.; Massoth, F. Deactivation of hydroprocessing catalysts. *Catalysis Today* **1999,** *52*, 381-495.

18. Laurent, E.; Centeno, A.; Delmon, B. Coke Formation during the Hydrotreating of Biomass Pyrolysis Oils - Influence of Guaiacol Type Compounds. *Catalyst Deactivation 1994* **1994,** *88*, 573-578.

19. Laurent, E.; Delmon, B. Influence of Water in the Deactivation of a Sulfided Nimo Gamma-Al2o3 Catalyst during Hydrodeoxygenation. *J Catal* **1994,** *146*, 281-291.

20. Lin, Y. C.; Li, C. L.; Wan, H. P.; Lee, H. T.; Liu, C. F. Catalytic Hydrodeoxygenation of Guaiacol on Rh-Based and Sulfided CoMo and NiMo Catalysts. *Energ Fuel* **2011,** *25*, 890-896.

21. Mortensen, P. M.; Grunwaldt, J. D.; Jensen, P. A.; Knudsen, K. G.; Jensen, A. D. A review of catalytic upgrading of bio-oil to engine fuels. *Appl Catal a-Gen* **2011,** *407*, 1-19.

22. Holladay, J. E.; White, J. F.; Bozell, J. J.; Johnson, D. In *Top Value Added Chemicals from Biomass - Volume II, Results of Screening for Potential Candidates from Biorefinery Lignin*, ; Pacific Northwest National Lab. (PNNL), Richland, WA (United States); National Renewable Energy Lab. (NREL), Golden, CO (United States): 2007; p Medium: ED; Size: 87.

23. Zakzeski, J.; Jongerius, A. L.; Bruijnincx, P. C. A.; Weckhuysen, B. M. Catalytic Lignin Valorization Process for the Production of Aromatic Chemicals and Hydrogen. *Chemsuschem* **2012,** *5*, 1602-1609.

24. Gonzalez-Borja, M. A.; Resasco, D. E. Anisole and Guaiacol Hydrodeoxygenation over Monolithic Pt-Sn Catalysts. *Energ Fuel* **2011,** *25*, 4155-4162.

25. Nimmanwudipong, T.; Runnebaum, R. C.; Block, D. E.; Gates, B. C. Catalytic Conversion of Guaiacol Catalyzed by Platinum Supported on Alumina: Reaction Network Including Hydrodeoxygenation Reactions. *Energ Fuel* **2011,** *25*, 3417-3427.

26. Lee, C. R.; Yoon, J. S.; Suh, Y. W.; Choi, J. W.; Ha, J. M.; Suh, D. J.; Park, Y. K. Catalytic roles of metals and supports on hydrodeoxygenation of lignin monomer guaiacol. *Catal Commun* **2012,** *17*, 54-58.

27. Nimmanwudipong, T.; Aydin, C.; Lu, J.; Runnebaum, R. C.; Brodwater, K. C.; Browning, N. D.; Block, D. E.; Gates, B. C. Selective Hydrodeoxygenation of Guaiacol Catalyzed by Platinum Supported on Magnesium Oxide. *Catal Lett* **2012,** *142*, 1190-1196.

28. Sun, J. M.; Karim, A. M.; Zhang, H.; Kovarik, L.; Li, X. H. S.; Hensley, A. J.; McEwen, J. S.; Wang, Y. Carbon-supported bimetallic Pd-Fe catalysts for vapor-phase hydrodeoxygenation of guaiacol. *J Catal* **2013,** *306*, 47-57.

29. He, Z.; Wang, X. Q. Highly selective catalytic hydrodeoxygenation of guaiacol to cyclohexane over Pt/TiO2 and NiMo/Al2O3 catalysts. *Front Chem Sci Eng* **2014,** *8*, 369-377.

30. Gao, D.; Schweitzer, C.; Hwang, H. T.; Varma, A. Conversion of Guaiacol on Noble Metal Catalysts: Reaction Performance and Deactivation Studies. *Ind Eng Chem Res* **2014,** *53*, 18658-18667.

31. Gao, D. N.; Xiao, Y.; Varma, A. Guaiacol Hydrodeoxygenation over Platinum Catalyst: Reaction Pathways and Kinetics. *Ind Eng Chem Res* **2015,** *54*, 10638-10644.

32. Lin, Y.-C.; Li, C.-L.; Wan, H.-P.; Lee, H.-T.; Liu, C.-F. Catalytic Hydrodeoxygenation of Guaiacol on Rh-Based and Sulfided CoMo and NiMo Catalysts. *Energy & Fuels* **2011,** *25*, 890-896.

33. Chang, J.; Danuthai, T.; Dewiyanti, S.; Wang, C.; Borgna, A. Hydrodeoxygenation of Guaiacol over Carbon-Supported Metal Catalysts. *Chemcatchem* **2013,** *5*, 3041-3049.

34. Hong, Y. K.; Lee, D. W.; Eom, H. J.; Lee, K. Y. The catalytic activity of Pd/WOx/gamma-Al2O3 for hydrodeoxygenation of guaiacol. *Appl Catal B-Environ* **2014,** *150*, 438-445.

35. Boonyasuwat, S.; Omotoso, T.; Resasco, D. E.; Crossley, S. P. Conversion of Guaiacol over Supported Ru Catalysts. *Catal Lett* **2013,** *143*, 783-791.

36. Nakagawa, Y.; Ishikawa, M.; Tamura, M.; Tomishige, K. Selective production of cyclohexanol and methanol from guaiacol over Ru catalyst combined with MgO. *Green Chem* **2014,** *16*, 2197-2203.

37. Olcese, R. N.; Bettahar, M.; Petitjean, D.; Malaman, B.; Giovanella, F.; Dufour, A. Gas-phase hydrodeoxygenation of guaiacol over Fe/SiO2 catalyst. *Applied Catalysis B: Environmental* **2012,** *115-116*, 63-73.

38. Bykova, M. V.; Ermakov, D. Y.; Kaichev, V. V.; Bulavchenko, O. A.; Saraev, A. A.; Lebedev, M. Y.; Yakovlev, V. A. Ni-based sol-gel catalysts as promising systems for crude bio-oil upgrading: Guaiacol hydrodeoxygenation study. *Appl Catal B-Environ* **2012,** *113*, 296-307.

39. Honkela, M. L.; Viljava, T. R.; Gutierrez, A.; Krause, A. O. I. Hydrotreating for Bio-Oil Upgrading. *Rsc Energy Environ S* **2010**, 288-306.

40. Schimming, S. M.; LaMont, O. D.; Konig, M.; Rogers, A. K.; D'Amico, A. D.; Yung, M. M.; Sievers, C. Hydrodeoxygenation of Guaiacol over Ceria-Zirconia Catalysts. *Chemsuschem* **2015,** *8*, 2073-2083.

41. Wildschut, J.; Mahfud, F.; Venderbosch, R.; Heeres, H. Hydrotreatment of Fast Pyrolysis Oil Using Heterogeneous Noble-Metal Catalysts. *Industrial & Engineering Chemistry Research* **2009,** *48*, 10324-10334.

42. Lu, J. M.; Heyden, A. Theoretical investigation of the reaction mechanism of the hydrodeoxygenation of guaiacol over a Ru(0001) model surface. *J Catal* **2015,** *321*, 39-50.

43. Narayan, S.; Muldoon, J.; Finn, M.; Fokin, V.; Kolb, H.; Sharpless, K. "On water": Unique reactivity of organic compounds in aqueous suspension. *Angewandte Chemie-International Edition* **2005,** *44*, 3275-3279.

44. Hellinger, M.; de Carvalho, H. W. P.; Baier, S.; Gharnati, L.; Grunwaldt, J. D. Solvent Influence on the Hydrodeoxygenation of Guaiacol over Pt/SiO2 and Pt/H-MFI90 Catalysts. *Chem-Ing-Tech* **2015,** *87*, 1771-1780.

45. Hellinger, M.; Baier, S.; Mortensen, P. M.; Kleist, W.; Jensen, A. D.; Grunwaldt, J. D. Continuous Catalytic Hydrodeoxygenation of Guaiacol over Pt/SiO2 and Pt/H-MFI-90. *Catalysts* **2015,** *5*, 1152-1166.

46. Ishikawa, M.; Tamura, M.; Nakagawa, Y.; Tomishige, K. Demethoxylation of guaiacol and methoxybenzenes over carbon-supported Ru-Mn catalyst. *Appl Catal B-Environ* **2016,** *182*, 193-203.

47. Reichardt, C.; Welton, T. In *Solvents and Solvent Effects in Organic Chemistry*, Reichardt, C.; Welton, T., Eds.; Wiley-VCH: Weinheim, Germany, 2011; pp 425-508.

48. Faheem, M.; Suthirakun, S.; Heyden, A. New Implicit Solvation Scheme for Solid Surfaces. *J Phys Chem C* **2012,** *116*, 22458-22462.

49. Yoon, J. S.; Choi, J. W.; Suh, D. J.; Lee, K.; Lee, H.; Ha, J. M. Water-Assisted Selective Hydrodeoxygenation of Lignin-Derived Guaiacol to Monooxygenates. *Chemcatchem* **2015,** *7*, 2669-2674.

50. Saleheen, M.; Heyden, A. Liquid-Phase Modeling in Heterogeneous Catalysis. *Acs Catal* **2018,** *8*, 2188-2194.

51. Behtash, S.; Lu, J. M.; Faheem, M.; Heyden, A. Solvent effects on the hydrodeoxygenation of propanoic acid over Pd(111) model surfaces (vol 16, pg 605, 2014). *Green Chem* **2014,** *16*, 4427-4428.

52. Behtash, S.; Lu, J. M.; Walker, E.; Mamun, O.; Heyden, A. Solvent effects in the liquid phase hydrodeoxygenation of methyl propionate over a Pd(111) catalyst model. *J Catal* **2016,** *333*, 171-183.

53. Behtash, S.; Lu, J. M.; Mamun, O.; Williams, C. T.; Monnier, J. R.; Heyden, A. Solvation Effects in the Hydrodeoxygenation of Propanoic Acid over a Model Pd(211) Catalyst. *J Phys Chem C* **2016,** *120*, 2724-2736.

54. Mamun, O.; Saleheen, M.; Bond, J. Q.; Heyden, A. Importance of Angelica Lactone Formation in the Hydrodeoxygenation of Levulinic Acid to gamma-Valerolactone over a Ru(0001) Model Surface. *J Phys Chem C* **2017,** *121*, 18746-18761.

55. Klamt, A. Conductor-Like Screening Model for Real Solvents - a New Approach to the Quantitative Calculation of Solvation Phenomena. *J Phys Chem-Us* **1995,** *99*, 2224-2235.

56. Klamt, A. In *COSMO-RS: From Quantum Chemistry to Fluid Phase Thermodynamics and Drug Design*, 1st ed.; Elsevier Science Ltd.: Amsterdam, Netherlands, 2005.

57. Wellendorff, J.; Lundgaard, K. T.; Møgelhøj, A.; Petzold, V.; Landis, D. D.; Nørskov, J. K.; Bligaard, T.; Jacobsen, K. W. Density functionals for surface science: Exchange-correlation model development with Bayesian error estimation. *Phys Rev B* **2012,** *85*, 235149.

58. Wellendorff, J.; Silbaugh, T. L.; Garcia-Pintos, D.; Norskov, J. K.; Bligaard, T.; Studt, F.; Campbell, C. T. A benchmark database for adsorption bond energies to transition metal surfaces and comparison to selected DFT functionals. *Surf Sci* **2015,** *640*, 36-44.

59. Liu, W.; Tkatchenko, A.; Scheffler, M. Modeling Adsorption and Reactions of Organic Molecules at Metal Surfaces. *Accounts of Chemical Research* **2014,** *47*, 3369-3377.

60. Studt, F.; Abild-Pedersen, F.; Varley, J. B.; Norskov, J. K. CO and CO2 Hydrogenation to Methanol Calculated Using the BEEF-vdW Functional. *Catal Lett* **2013,** *143*, 71-73.

61. Studt, F.; Behrens, M.; Kunkes, E. L.; Thomas, N.; Zander, S.; Tarasov, A.; Schumann, J.; Frei, E.; Varley, J. B.; Abild-Pedersen, F.; Norskov, J. K.; Schlogl, R. The Mechanism of CO and CO2 Hydrogenation to Methanol over Cu-Based Catalysts. *Chemcatchem* **2015,** *7*, 1105-1111.

62. Perdew, J. P.; Burke, K.; Ernzerhof, M. Generalized gradient approximation made simple. *Phys Rev Lett* **1996,** *77*, 3865-3868.

63. Grimme, S.; Antony, J.; Ehrlich, S.; Krieg, H. A consistent and accurate ab initio parametrization of density functional dispersion correction (DFT-D) for the 94 elements H-Pu. *J Chem Phys* **2010,** *132*.

64. Ahlrichs, R.; Bar, M.; Haser, M.; Horn, H.; Kolmel, C. Electronic-Structure Calculations on Workstation Computers - the Program System Turbomole. *Chem Phys Lett* **1989,** *162*, 165-169.

65. Von Arnim, M.; Ahlrichs, R. Performance of parallel TURBOMOLE for density functional calculations. *J Comput Chem* **1998,** *19*, 1746-1757.

66. Weigend, F.; Ahlrichs, R. Balanced basis sets of split valence, triple zeta valence and quadruple zeta valence quality for H to Rn: Design and assessment of accuracy. *Phys Chem Chem Phys* **2005,** *7*, 3297-3305.

67. Russo, T. V.; Martin, R. L.; Hay, P. J. Effective Core Potentials for Dft Calculations. *J Phys Chem-Us* **1995,** *99*, 17085-17087.

68. Becke, A. D. Density-Functional Exchange-Energy Approximation with Correct Asymptotic-Behavior. *Phys Rev A* **1988,** *38*, 3098-3100.

69. Perdew, J. P. Density-Functional Approximation for the Correlation-Energy of the Inhomogeneous Electron-Gas. *Phys Rev B* **1986,** *33*, 8822-8824.

70. Eichkorn, K.; Treutler, O.; Ohm, H.; Haser, M.; Ahlrichs, R. Auxiliary Basis-Sets to Approximate Coulomb Potentials. *Chem Phys Lett* **1995,** *240*, 283-289.

71. Weigend, F. Accurate Coulomb-fitting basis sets for H to Rn. *Phys Chem Chem Phys* **2006,** *8*, 1057-1065.

72. Eichkorn, K.; Weigend, F.; Treutler, O.; Ahlrichs, R. Auxiliary basis sets for main row atoms and transition metals and their use to approximate Coulomb potentials. *Theor Chem Acc* **1997,** *97*, 119-124.

73. Klamt, A.; Schuurmann, G. Cosmo - a New Approach to Dielectric Screening in Solvents with Explicit Expressions for the Screening Energy and Its Gradient. *J Chem Soc, Perkin Trans 2* **1993**, 799-805.

74. Schafer, A.; Klamt, A.; Sattel, D.; Lohrenz, J. C. W.; Eckert, F. COSMO Implementation in TURBOMOLE: Extension of an efficient quantum chemical code towards liquid systems. *Phys Chem Chem Phys* **2000,** *2*, 2187-2193.

75. Faheem, M.; Saleheen, M.; Lu, J. M.; Heyden, A. Ethylene glycol reforming on Pt(111): first-principles microkinetic modeling in vapor and aqueous phases. *Catal Sci Technol* **2016,** *6*, 8242-8256. **A new transition state for primary C-H cleavage of ethylene glycol was later found which has 0.10 eV lower energy than reported herein.*

76. Chen, W.; Luo, Z. Y.; Yu, C. J.; Yang, Y.; Li, G. X.; Zhang, J. X. Catalytic conversion of guaiacol in ethanol for bio-oil upgrading to stable oxygenated organics. *Fuel Process Technol* **2014,** *126*, 420-428.

77. Lu, M. H.; Du, H.; Wei, B.; Zhu, J.; Li, M. S.; Shan, Y. H.; Shen, J. Y.; Song, C. S. Hydrodeoxygenation of Guaiacol on Ru Catalysts: Influence of TiO2-ZrO2 Composite Oxide Supports. *Ind Eng Chem Res* **2017,** *56*, 12070-12079.

78. Zhao, C.; He, J. Y.; Lemonidou, A. A.; Li, X. B.; Lercher, J. A. Aqueous-phase hydrodeoxygenation of bio-derived phenols to cycloalkanes. *J Catal* **2011,** *280*, 8-16.

79. Kamlet, M. J.; Taft, R. W. Solvatochromic Comparison Method .1. Beta-Scale of Solvent Hydrogen-Bond Acceptor (Hba) Basicities. *J Am Chem Soc* **1976,** *98*, 377-383.

80. Yokoyama, T.; Taft, R. W.; Kamlet, M. J. Solvatochromic Comparison Method .3. Hydrogen-Bonding by Some 2-Nitroaniline Derivatives. *J Am Chem Soc* **1976,** *98*, 3233-3237.

81. Taft, R. W.; Kamlet, M. J. Solvatochromic Comparison Method .2. Alpha-Scale of Solvent Hydrogen-Bond Donor (Hbd) Acidities. *J Am Chem Soc* **1976,** *98*, 2886-2894.

82. Mcquarrie, D. A. Statistical Mechanics. *Phys Today* **1965,** *18*, 74-+.

83. Pechukas, P. Transition-State Theory. *Annu Rev Phys Chem* **1981,** *32*, 159-177.

84. Kandoi, S.; Greeley, J.; Sanchez-Castillo, M. A.; Evans, S. T.; Gokhale, A. A.; Dumesic, J. A.; Mavrikakis, M. Prediction of experimental methanol decomposition rates on platinum from first principles. *Top Catal* **2006,** *37*, 17-28.

85. Mamun, O.; Walker, E.; Faheem, M.; Bond, J. Q.; Heyden, A. Theoretical Investigation of the Hydrodeoxygenation of Levulinic Acid to gamma-Valerolactone over Ru(0001). *Acs Catal* **2017,** *7*, 215-228.

86. Getman, R. B.; Schneider, W. F. Investigation of NO oxidation catalysis on Pt(111) with regard to reaction conditions. *Abstr Pap Am Chem S* **2007,** *233*.

87. Getman, R. B.; Schneider, W. F. DFT-based characterization of the multiple adsorption modes of nitrogen oxides on Pt(111). *J Phys Chem C* **2007,** *111*, 389-397.

88. Grabow, L. C.; Hvolbaek, B.; Norskov, J. K. Understanding Trends in Catalytic Activity: The Effect of Adsorbate-Adsorbate Interactions for CO Oxidation Over Transition Metals. *Top Catal* **2010,** *53*, 298-310.

89. Wang, Y.; Yao, J.; Li, H. R.; Su, D. S.; Antonietti, M. Highly Selective Hydrogenation of Phenol and Derivatives over a Pd@Carbon Nitride Catalyst in Aqueous Media. *J Am Chem Soc* **2011,** *133*, 2362-2365.

90. He, J.; Lu, X. H.; Shen, Y.; Jing, R.; Nie, R. F.; Zhou, D.; Xia, Q. H. Highly selective hydrogenation of phenol to cyclohexanol over nano silica supported Ni catalysts in aqueous medium. *Mol Catal* **2017,** *440*, 87-95.

91. Giraldo, L.; Bastidas-Barranco, M.; Moreno-Pirajan, J. C. Vapour Phase Hydrogenation of Phenol over Rhodium on SBA-15 and SBA-16. *Molecules* **2014,** *19*, 20594-20612.

92. Liu, H. Z.; Jiang, T.; Han, B. X.; Liang, S. G.; Zhou, Y. X. Selective Phenol Hydrogenation to Cyclohexanone Over a Dual Supported Pd-Lewis Acid Catalyst. *Science* **2009,** *326*, 1250-1252.

93. He, J. Y.; Zhao, C.; Lercher, J. A. Impact of solvent for individual steps of phenol hydrodeoxygenation with Pd/C and HZSM-5 as catalysts. *J Catal* **2014,** *309*, 362-375.

94. Campbell, C. T. Micro- and macro-kinetics: their relationship in heterogeneous catalysis. *Top Catal* **1994,** *1*, 353-366.

95. Campbell, C. T. Finding the rate-determining step in a mechanism - Comparing DeDonder relations with the "degree of rate control". *J Catal* **2001,** *204*, 520-524.

96. Stegelmann, C.; Andreasen, A.; Campbell, C. T. Degree of Rate Control: How Much the Energies of Intermediates and Transition States Control Rates. *J Am Chem Soc* **2009,** *131*, 8077-8082.

97. Evans, M. G.; Polanyi, M. Further considerations on the thermodynamics of chemical equilibria and reaction rates. *T Faraday Soc* **1936,** *32*, 1333-1359.

98. Zhong, J. W.; Chen, J. Z.; Chen, L. M. Selective hydrogenation of phenol and related derivatives. *Catalysis Science & Technology* **2014,** *4*, 3555-3569.

APPENDIX A:

SUPPORTING INFORMATION FOR LIQUID PHASE MODELING IN HETEROGENEOUS CATALYSIS

Saleheen, M.; Heyden, A. *ACS Catalysis,*

2018, 8 (3), 2188-2194.

A.1 Computational Details

A.1.1 Planewave periodic DFT calculations

All vapor phase DFT calculations presented in this contribution were carried out using the Vienna Ab Initio Simulation Package (VASP 5.3)[1-4] under periodic boundary conditions. The ion-core electronic states were described by the projector-augmented wave (PAW)[5] method while the electron exchange and correlation effects were accounted for using the Perdew-Burke-Erznzerhof (PBE)[6-7] functional within the semilocal Generalized Gradient Approximation (GGA).[8] The electronic wavefunctions were expanded using a plane-wave basis set with a kinetic energy cutoff of 400 eV and the k-point sampling in the Brillouin zone was performed by employing the Monkhorst-Pack[9] scheme. Entropic contributions arising from the fractional occupancies of bands were accounted for using a first order cold smearing method (Methfessel-Paxton[10]) with 0.10 eV smearing window. All self-consistent field (SCF) calculations for the valence electrons were converged up to 1.0×10^{-7} eV. The Pt(111) model surface was mimicked using a 4×4 unit cell with 4 layers of Pt atoms (top two layers relaxed) and a 15 Å vacuum was introduced on top of the surface to minimize the interaction between periodic images along the surface normal. A modified version of Makov-Payne method[11] was employed to account for the dipole and quadrupole corrections (parallel to the surface plane) to the energy. Transition state searches were carried out using a combination of climbing-image nudged elastic band[12-13] and dimer[14-15] methods. Finally, dynamical matrix calculations were performed to ascertain the location of minima and transition state structures.

A.1.2 Implicit Solvation (iSMS)

A hexagonal Pt(111) cluster model with 2 layers of Pt atoms (51 atoms) was used to calculate the free energies of solvation with the implicit solvation scheme, iSMS. Nonperiodic cluster model calculations were performed for multiple spin states in search for the lowest-energy spin state with the TURBOMOLE 6.5[16-18] program package. Adsorbate atoms were represented using all electron basis sets of triple-ζ quality (TZVP),[19-20] while relativistic effective core potentials (ECPs) combined with triple-ζ quality basis sets for valence electrons were employed for describing the metal (Pt) atoms.[21-22] The PBE functional[6-7] was utilized for describing the electron exchange and correlation effects and coulomb potentials were approximated with the RI-J approximation using auxiliary basis sets.[23-24] A 1.0×10^{-7} Hartree SCF energy convergence criterion was established with an m4 spherical grid. Finally, implicit solvation calculations for the lowest energy spin state were performed using the COSMO[25-26] and COSMO-RS[27-28] procedures. Due to the specification of the COSMO-RS parameterization, these calculations were performed by employing the BP-86 functional.[29] A detailed description of our iSMS methodology can be found elsewhere.[30]

A.1.3 Hybrid QM/MM methodology and free energy estimator

An augmented 16×20 unit cell with 4 layers of Pt atoms resulting in a 45.0 Å × 48.7 Å × 49.0 Å simulation box comprising 1280 Pt atoms was employed for our QM/MM methodology (eSMS) and the MD simulations, performed using the DL_POLY 4.03 program package.[31] The experimental density of saturated liquid water at 500 K was used in our simulations by packing the simulation box with 2200 water molecules. The geometry of the water molecules was constrained to that of the TIP3P[32] water model with the SHAKE[33] algorithm. The Spohr-Heinzinger potential[34] was used for describing the interaction between the metal atoms (Pt) and the water molecules while the OPLS force field parameters[35-36] were used for adsorbate (ethylene glycol) and water interaction (partial charges for all QM atoms are obtained from natural population analysis - NPA[37]). Simulations were carried out in a canonical (NVT) ensemble along with the Berendsen thermostat[38] to maintain the simulation temperature. A 12 Å cutoff value was used for all van-der-Waals interactions and for splitting the long-range electrostatic interactions into short- and long-range interactions. A reformulated particle mesh Ewald method (Smooth Particle Mesh Ewald, SPME)[39] with B-spline interpolation was used to account for the long-range electrostatic interactions.

Utilizing ultrafast spectroscopy, it has been reported that in liquid water, the correlation time within the hydrogen bonded network of water molecules is ~50 fs[40] and hence, the total QM/MM energy has been computed in a fixed-size ensemble of MM conformations (1000) recorded every 50 fs from an MD simulation consisting of a 250 ps equilibration period and a 50 ps sampling period. A detailed description of our QM/MM methodology can be found elsewhere.[41]

An accurate estimation of free energies at solid-liquid interfaces requires the generation of statistically uncorrelated water conformations and the use of a free energy estimator that reduces the statistical bias and variance of the calculated free energy difference.[42-45] We used the Bennett acceptance ratio[46] (BAR) as the free energy estimator which makes use of both forward and reverse exponential averaging and which has been shown to lower the bias and variance of the free energy difference between two non-physical states relative to exponential averaging (EXP) and thermodynamic integration (TI).[44] For each model reaction, the whole calculation procedure was repeated ten times to establish 95% confidence intervals for the calculation of the free energy of reaction and activation, assuming a normal distribution.[47] Overall, the computational expense of our eSMS method is only two orders of magnitude higher than the expense for conventional gas-phase computations.

A.1.4 Solvent accessible surface (SAS) and surface charge density (SCD)

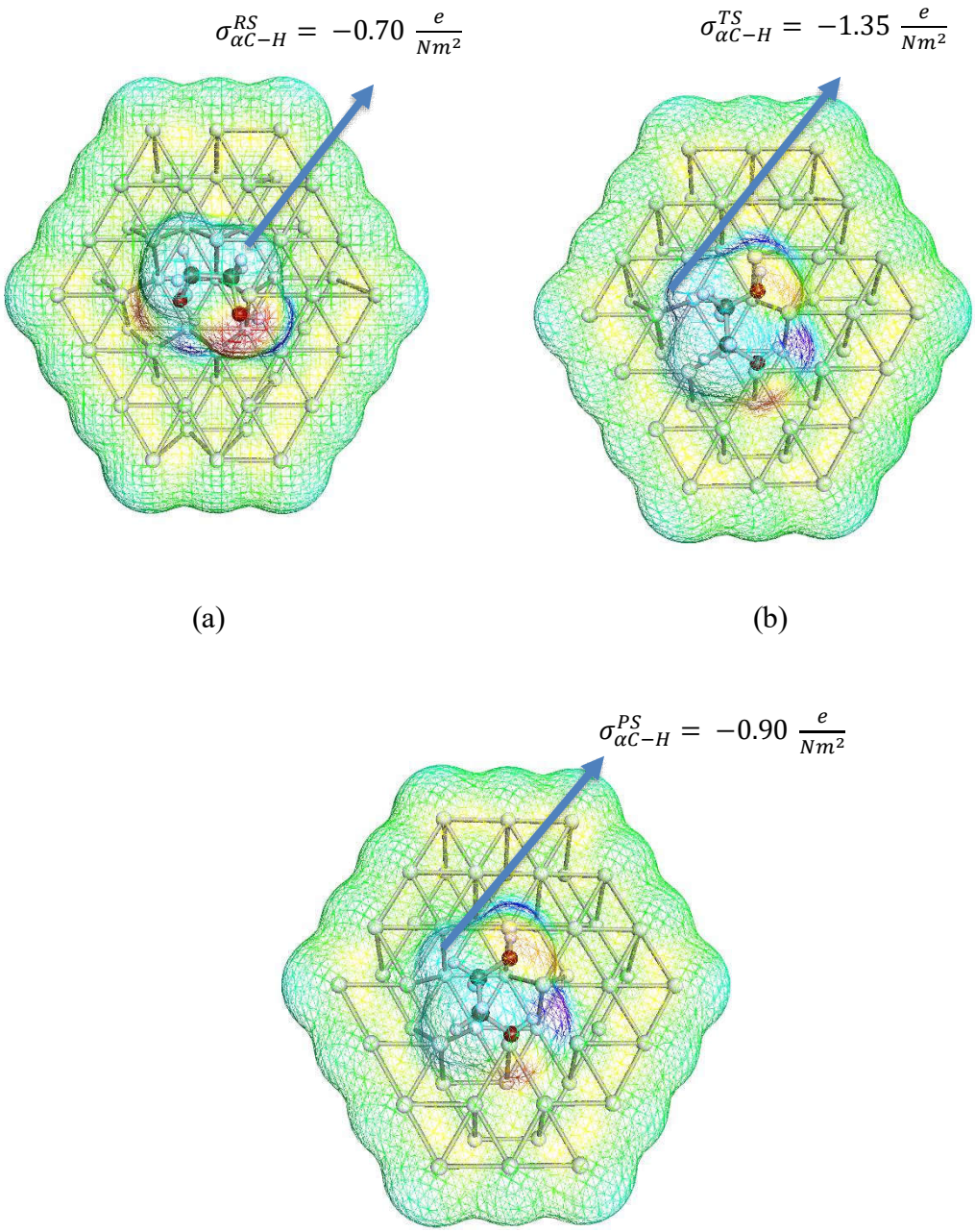

Figure A.1.4: Maximum surface charge densities (SCDs) of the reacting hydrogen atom during C-H bond cleavage of ethylene glycol over Pt(111): (a) Reactant, (b) transition, and (c) product states.

A.2. Bibliography

1. Kresse, G.; Hafner, J. *Phys Rev B* **1993,** *47*, 558-561.
2. Kresse, G.; Furthmuller, J. *Comp Mater Sci* **1996,** *6*, 15-50.
3. Kresse, G.; Furthmuller, J. *Phys Rev B* **1996,** *54*, 11169-11186.
4. Kresse, G.; Joubert, D. *Phys Rev B* **1999,** *59*, 1758-1775.
5. Blochl, P. E. *Phys Rev B* **1994,** *50*, 17953-17979.
6. Perdew, J. P.; Yue, W. *Phys Rev B* **1986,** *33*, 8800-8802.
7. Perdew, J. P.; Wang, Y. *Phys Rev B* **1992,** *45*, 13244-13249.
8. Perdew, J. P.; Burke, K.; Ernzerhof, M. *Phys Rev Lett* **1996,** *77*, 3865-3868.
9. Monkhorst, H. J.; Pack, J. D. *Phys Rev B* **1976,** *13*, 5188-5192.
10. Methfessel, M.; Paxton, A. T. *Phys Rev B* **1989,** *40*, 3616-3621.
11. Makov, G.; Payne, M. C. *Phys Rev B* **1995,** *51*, 4014-4022.
12. Henkelman, G.; Uberuaga, B. P.; Jonsson, H. *J Chem Phys* **2000,** *113*, 9901-9904.
13. Henkelman, G.; Jonsson, H. *J Chem Phys* **2000,** *113*, 9978-9985.
14. Henkelman, G.; Jonsson, H. *J Chem Phys* **1999,** *111*, 7010-7022.
15. Heyden, A.; Bell, A. T.; Keil, F. J. *J Chem Phys* **2005,** *123*, 224101:1-14.
16. Ahlrichs, R.; Bar, M.; Haser, M.; Horn, H.; Kolmel, C. *Chem Phys Lett* **1989,** *162*, 165-169.
17. Treutler, O.; Ahlrichs, R. *J Chem Phys* **1995,** *102*, 346-354.
18. Von Arnim, M.; Ahlrichs, R. *J Comput Chem* **1998,** *19*, 1746-1757.
19. Schafer, A.; Horn, H.; Ahlrichs, R. *J Chem Phys* **1992,** *97*, 2571-2577.
20. Schafer, A.; Huber, C.; Ahlrichs, R. *J Chem Phys* **1994,** *100*, 5829-5835.
21. Eichkorn, K.; Weigend, F.; Treutler, O.; Ahlrichs, R. *Theor Chem Acc* **1997,** *97*, 119-124.
22. Weigend, F.; Ahlrichs, R. *Phys Chem Chem Phys* **2005,** *7*, 3297-3305.
23. Eichkorn, K.; Treutler, O.; Ohm, H.; Haser, M.; Ahlrichs, R. *Chem Phys Lett* **1995,** *240*, 283-289.
24. Weigend, F. *Phys Chem Chem Phys* **2006,** *8*, 1057-1065.
25. Klamt, A.; Schuurmann, G. *J Chem Soc Perk T 2* **1993**, 799-805.
26. Schafer, A.; Klamt, A.; Sattel, D.; Lohrenz, J. C. W.; Eckert, F. *Phys Chem Chem Phys* **2000,** *2*, 2187-2193.
27. Klamt, A. *J Phys Chem-Us* **1995,** *99*, 2224-2235.
28. Klamt, A. In *COSMO-RS: From Quantum Chemistry to Fluid Phase Thermodynamics and Drug Design*, 1st ed.; Elsevier Science Ltd.: Amsterdam, Netherlands, 2005.
29. Becke, A. D. *Phys Rev A* **1988,** *38*, 3098-3100.
30. Faheem, M.; Suthirakun, S.; Heyden, A. *J Phys Chem C* **2012,** *116*, 22458-22462.
31. Todorov, I. T.; Smith, W.; Trachenko, K.; Dove, M. T. *J Mater Chem* **2006,** *16*, 1911-1918.
32. Jorgensen, W. L.; Chandrasekhar, J.; Madura, J. D.; Impey, R. W.; Klein, M. L. *J Chem Phys* **1983,** *79*, 926-935.
33. Smith, W.; Forester, T. R. *Comput Phys Commun* **1994,** *79*, 63-77.
34. Spohr, E. *J Phys Chem-Us* **1989,** *93*, 6171-6180.
35. Jorgensen, W. L. *J Phys Chem-Us* **1986,** *90*, 1276-1284.
36. Geerke, D. P.; Van Gunsteren, W. F. *Mol Phys* **2007,** *105*, 1861-1881.

37. Reed, A. E.; Weinstock, R. B.; Weinhold, F. *J Chem Phys* **1985,** *83*, 735-746.
38. Berendsen, H. J. C.; Postma, J. P. M.; Vangunsteren, W. F.; Dinola, A.; Haak, J. R. *J Chem Phys* **1984,** *81*, 3684-3690.
39. Essmann, U.; Perera, L.; Berkowitz, M. L.; Darden, T.; Lee, H.; Pedersen, L. G. *J Chem Phys* **1995,** *103*, 8577-8593.
40. Cowan, M. L.; Bruner, B. D.; Huse, N.; Dwyer, J. R.; Chugh, B.; Nibbering, E. T. J.; Elsaesser, T.; Miller, R. J. D. *Nature* **2005,** *434*, 199-202.
41. Faheem, M.; Heyden, A. *J Chem Theory Comput* **2014,** *10*, 3354-3368.
42. Klimovich, P. V.; Shirts, M. R.; Mobley, D. L. *J Comput Aid Mol Des* **2015,** *29*, 397-411.
43. Shirts, M. R.; Mobley, D. L. In *Biomolecular Simulations: Methods and Protocols*, 2013th ed.; Monticelli, L.; Salonen, E., Eds.; Humana Press: Totowa, NJ, 2013.
44. Shirts, M. R.; Pande, V. S. *J Chem Phys* **2005,** *122*, 144107:1-16.
45. Shirts, M. R.; Pande, V. S. *J Chem Phys* **2005,** *122*, 134508:1-13.
46. Bennett, C. *Journal of Computational Physics* **1976,** *22*, 245-268.
47. Kreyszig, E. In *Advanced Engineering Mathematics*, 9th ed.; John Wiley & Sons, Inc.: New York, 2006.

APPENDIX B:

SUPPORTING INFORMATION FOR COMPUTATIONAL INVESTIGATION OF AQUEOUS-PHASE EFFECTS ON THE DEHYDROGENATION AND DEHYDROXYLATION OF POLYOLS OVER Pt(111)

Saleheen, M.; Zare, M.; Faheem, M.; Heyden, A.

Submitted to *The Journal of Physical Chemistry C*

Table B.1: Effect of equilibration time on the free energy of reaction and the free energy of activation for the O-H bond cleavage of ethylene glycol over a Pt(111) model surface under aqueous phase processing conditions.

Reaction environment	Equilibration time (ps)	ΔG_{rxn} (eV)	$\Delta G^{\dagger}$ (eV)
Vapor phase	-	0.45	0.70
Aqueous phase	50	-0.09±0.03	0.11±0.01
	100	-0.11±0.04	0.10±0.02
	250	-0.09±0.06	0.11±0.04

Table B.2: Aqueous phase effects on the free energy of reaction and the free energy of activation for the O-H bond cleavage of ethylene glycol over a Pt(111) model surface at 500 K, ensemble averages computed by sampling different amounts of phase space.

Reaction environment	Number of water conformations	ΔG_{rxn} (eV)	$\Delta G^{\dagger}$ (eV)
Vapor phase	-	0.45	0.70
Aqueous phase	100	-0.11±0.09	0.12±0.05
	500	-0.10±0.01	0.12±0.01
	1000	-0.09±0.06	0.11±0.04

Table B.3: Aqueous phase effects on the free energy of reaction and the free energy of activation for the O-H bond cleavage of ethylene glycol over a Pt(111) model surface at 500 K, solvated using different number of water molecules.

Reaction environment	Number of water molecules	ΔG_{rxn} (eV)	$\Delta G^{\dagger}$ (eV)
Vapor phase	-	0.45	0.70
Aqueous phase	990	-0.09±0.05	0.10±0.02
	1320	-0.08±0.04	0.11±0.03
	1760	-0.10±0.03	0.11±0.01
	2200	-0.09±0.06	0.11±0.04

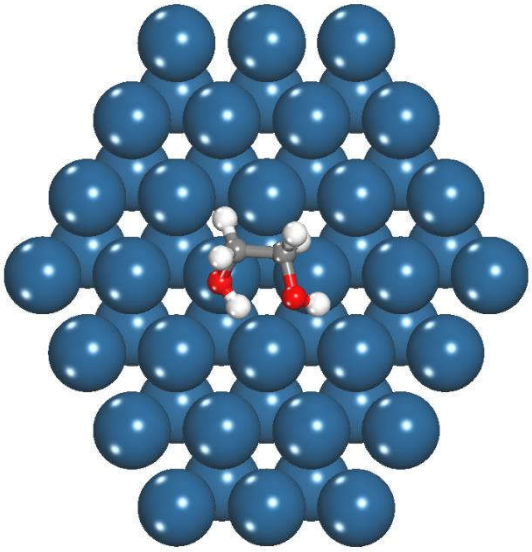

(a)

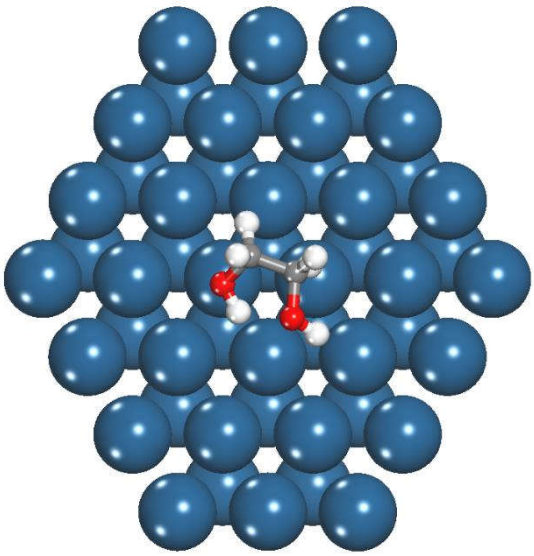

(b)

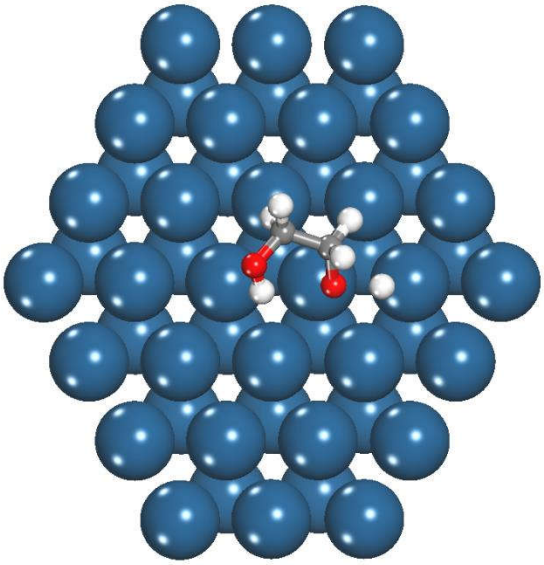

(c)

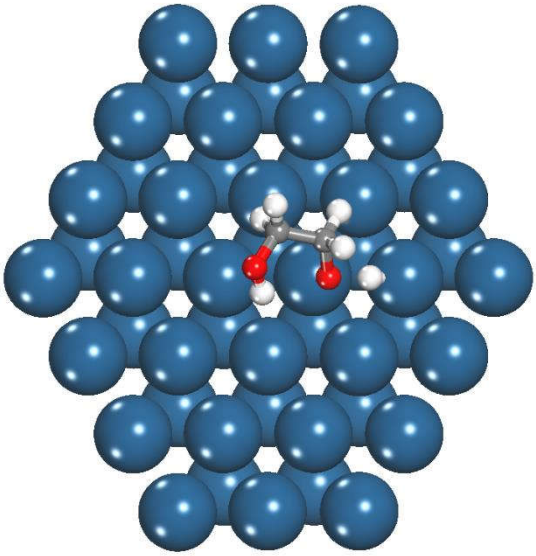

(d)

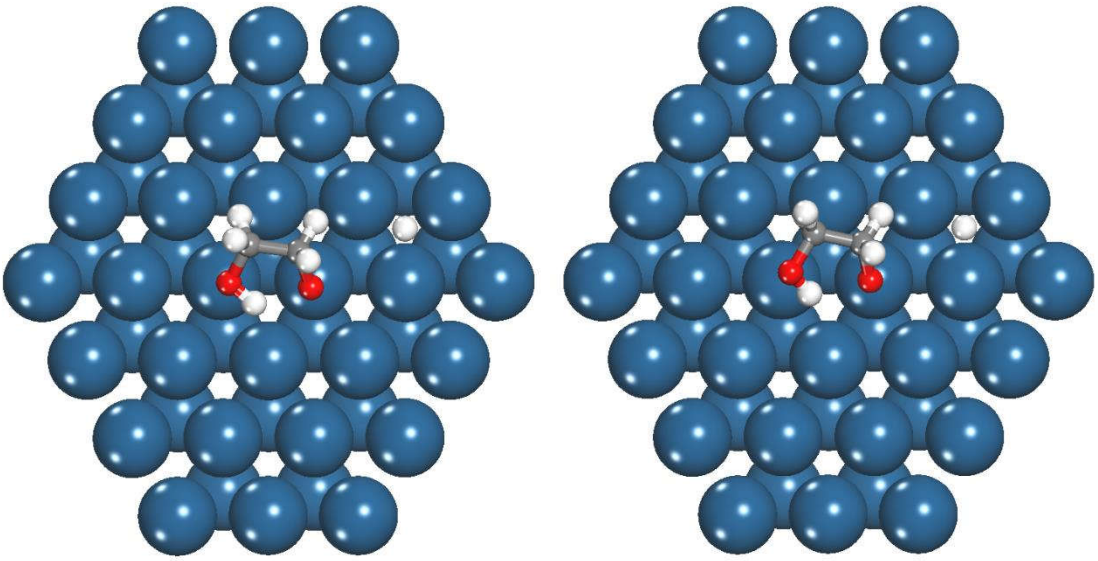

(e) (f)

Figure B.1: Optimized geometries of the reactant state [(a) and (b)], transition state [(c) and (d)], and product state [(e) and (f)] for the O-H bond scission of ethylene glycol over a Pt(111) surface at 500 K. Figures (a), (c), and (e) represent the optimized geometries in vapor phase while (b), (d), and (f) represent the optimized geometries in aqueous phase.

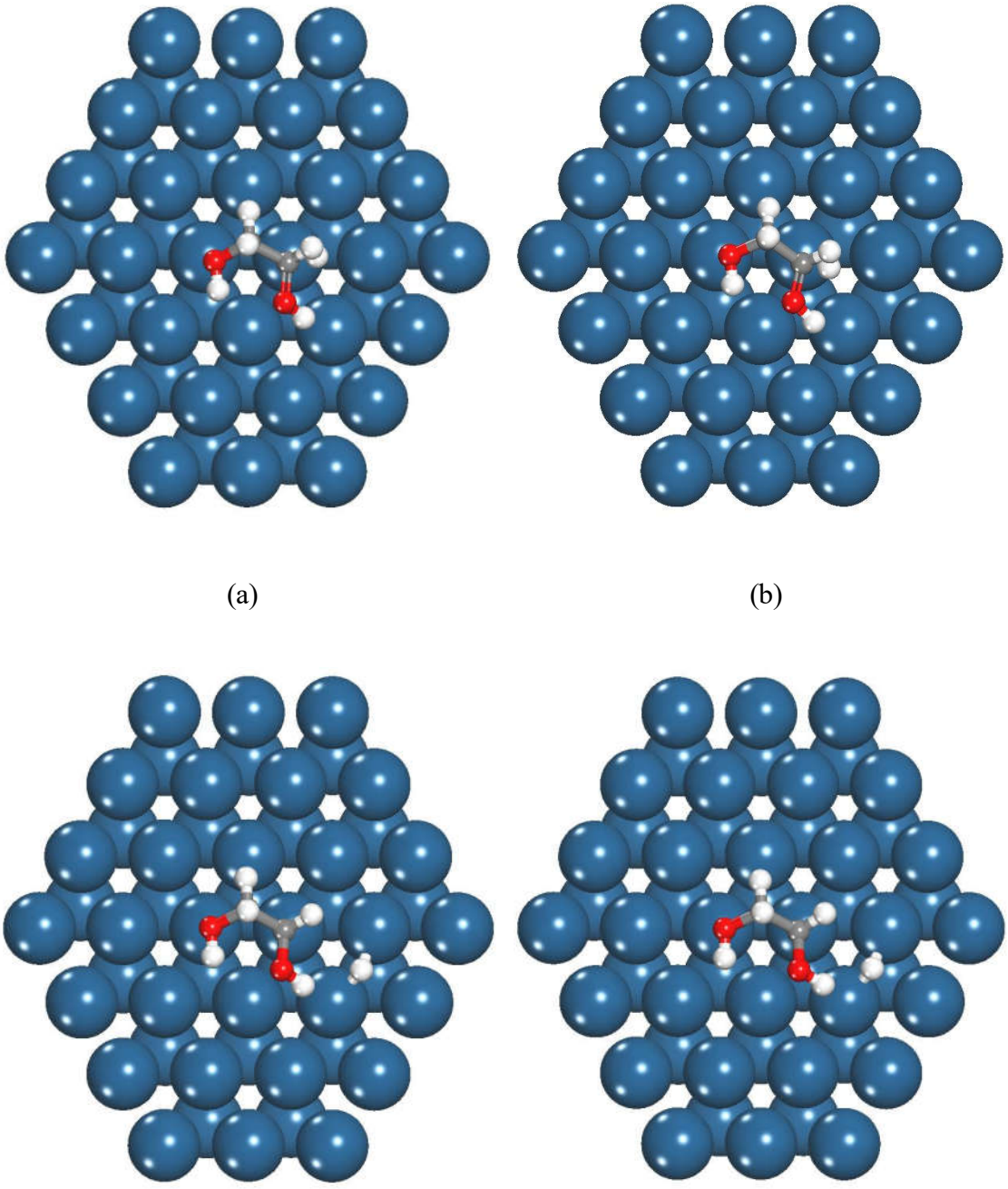

Figure B.2: Optimized geometries of the transition state [(a) and (b)] and product state [(c) and (d)] for the C-H bond scission of ethylene glycol over a Pt(111) surface at 500 K. Figures (a) and (c) represent the optimized geometries in vapor phase while (b) and (d) represent the optimized geometries in aqueous phase.

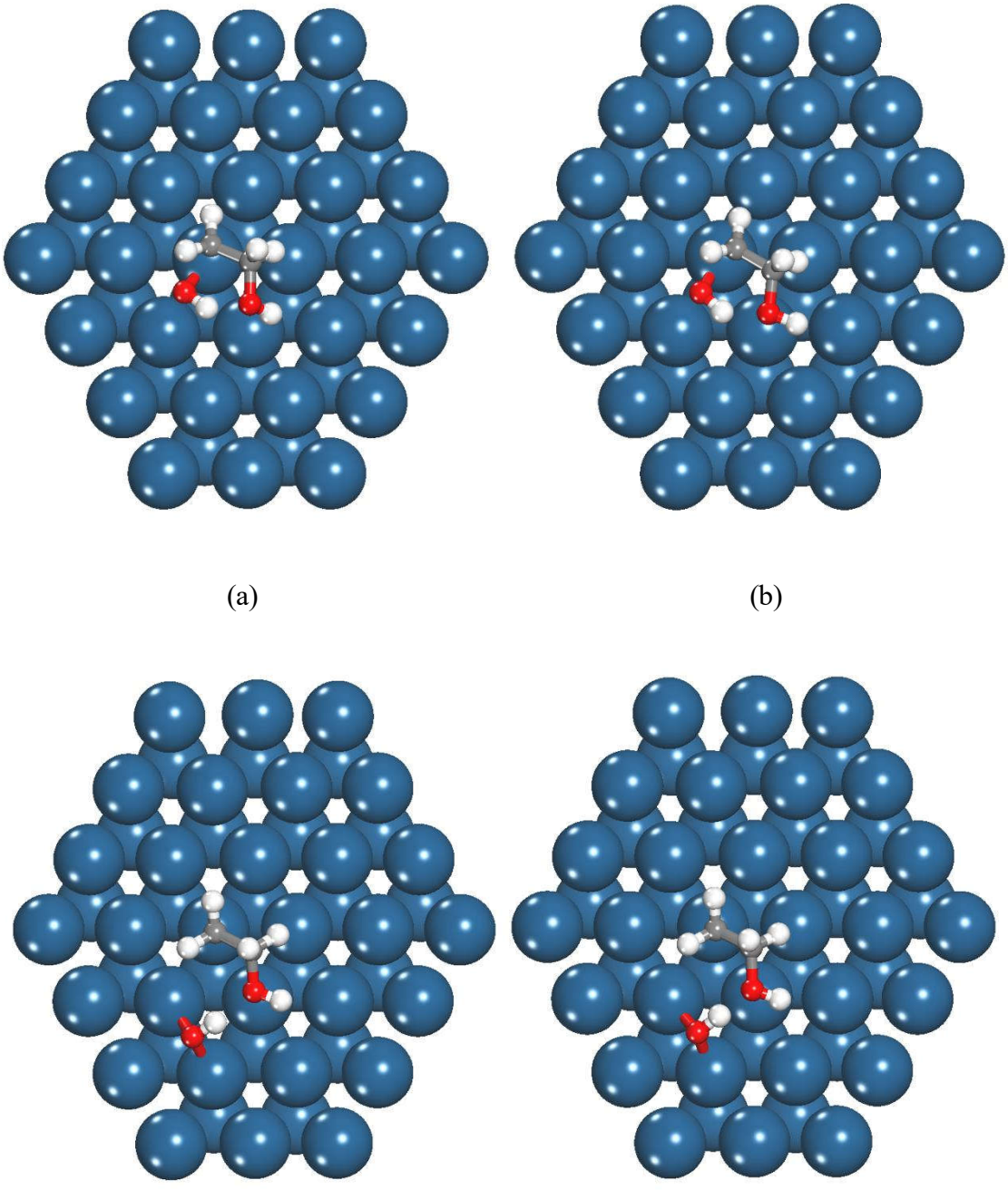

(a) (b)

(c) (d)

Figure B.3: Optimized geometries of the transition state [(a) and (b)] and product state [(c) and (d)] for the C-OH bond scission of ethylene glycol over a Pt(111) surface at 500 K. Figures (a) and (c) represent the optimized geometries in vapor phase while (b) and (d) represent the optimized geometries in aqueous phase.

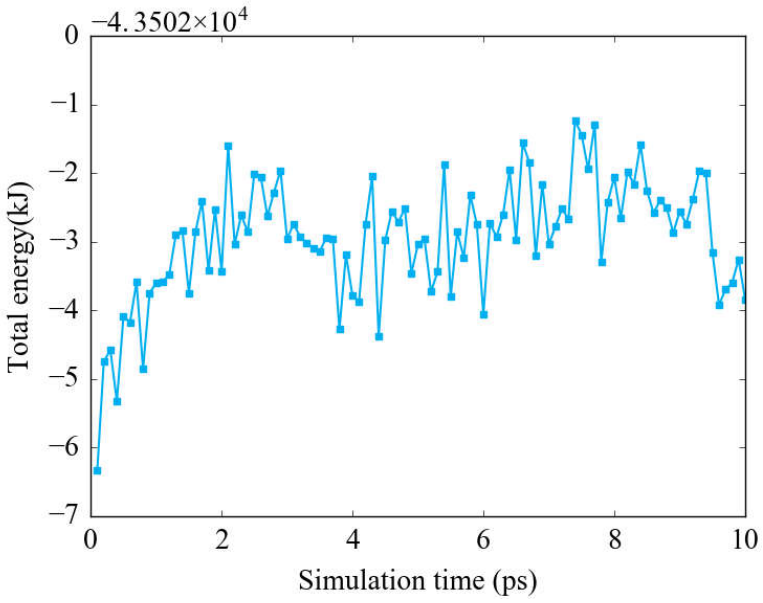

(a)

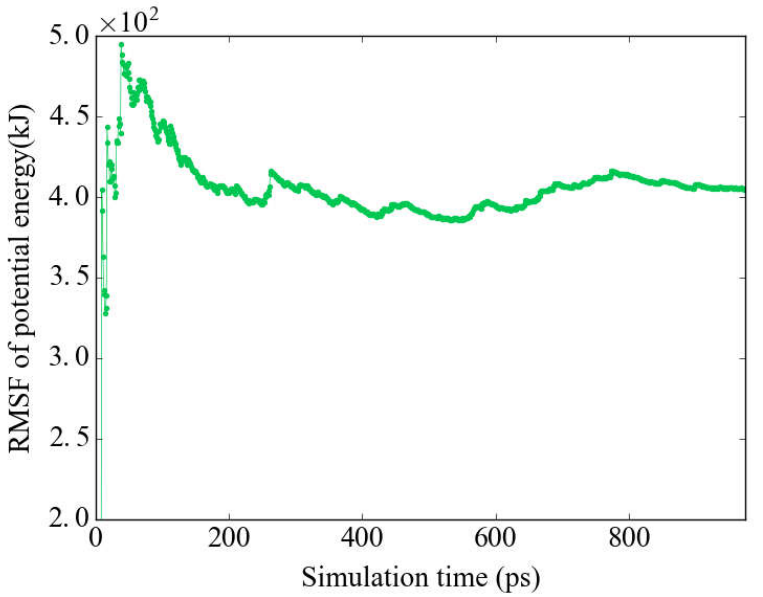

(b)

Figure B.4: Time dependence of (a) total energy and (b) root mean square fluctuations (RMSF) of potential energy for a 975 ps molecular dynamics simulation of ethylene glycol adsorbed on a Pt(111) surface solvated using 2200 water molecules. The time dependent total energy is only displayed for the initial 10 ps.

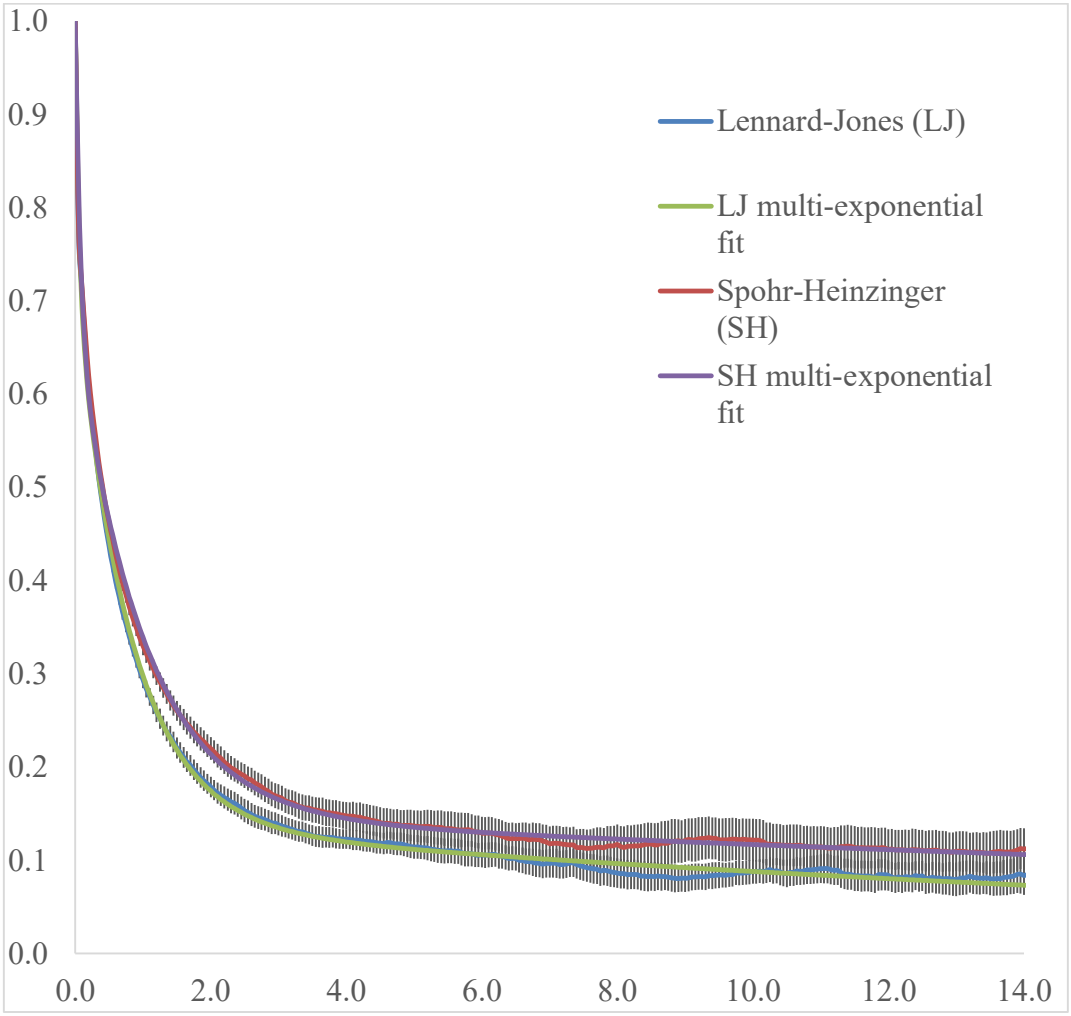

Figure B.5: Rotational time correlation function of liquid water molecules residing in a 5 Å radius of adsorbed ethylene glycol ($C_2H_5OH^*$) species on Pt(111), for the Lennard-Jones (LJ) and Spohr-Heinzinger (SH) potential. Both LJ and SH potential predicted correlation functions have been fitted with three exponential functions to calculate average rotational correlation times of ~20 ps (LJ) and ~40 ps (SH).

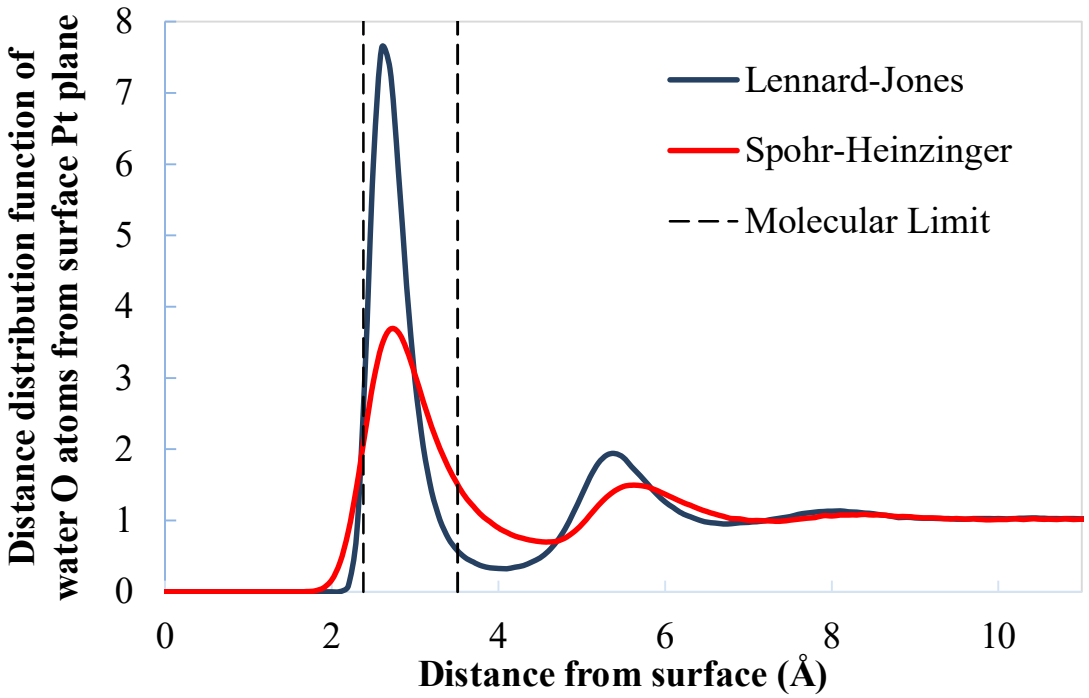

Figure B.6: Distance distribution function of water O atoms over a Pt(111) surface for 2 different metal-water interaction potentials. The two vertical dotted lines enclose the distance range from the surface within which the adsorbed ethylene glycol C- and O-atoms reside.

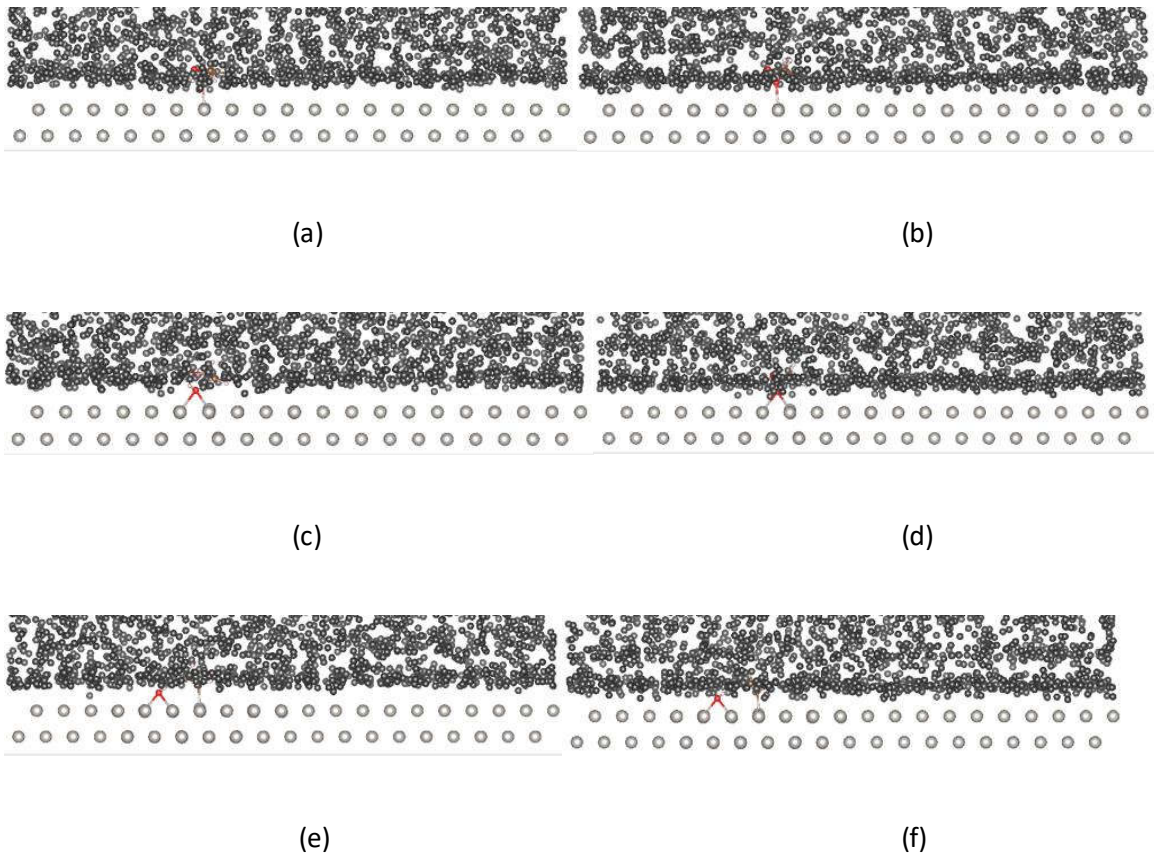

Figure B.7: Snapshot of water molecules on top of Pt(111) for the reactant state ((a) and (b)), transition state ((c) and (d)), and product state ((e) and (f)) of C-OH bond cleavage of ethylene glycol. Figures (a), (c), and (e) illustrate the geometries where the metal-water interaction has been described using the Spohr-Heinzinger potential while figures (b), (d), and (f) portray that of the Lennard-Jones potential. The black balls represent the oxygen and hydrogen atoms of the water molecules.

APPENDIX C:

SUPPORTING INFORMATION FOR INVESTIGATION OF SOLVENT EFFECTS ON THE HYDRODEOXYGENATION OF GUAIACOL OVER Ru CATALYST

Saleheen, M.; Verma, A. M.; Mamun, O; Lu, J.; Heyden, A.

To be submitted

Table C.1: Kamlet and Taft's solvatochromic parameters; polarizability (π^*), hydrogen-bond donor (α)and acceptor (β), and normalized polarity (E_T^N); derived from the solvatochromism of pyridinium N-phenolate betaine for solvents employed in the HDO of guaiacol over Ru(0001) model surface.

Solvents	π^*	α	β	E_T^N
Water	1.09	1.17	0.47	1.000
1-Butanol	0.47	0.84	0.84	0.586
Diethyl ether	0.24	0.00	0.47	0.117
n-Hexane	-0.11	0.00	0.00	0.009

Table C.2: Lateral interaction parameters employed in the microkinetic model for HDO of guaiacol over Ru(0001) model surface.

Adsorbate pairs	Lateral interaction (eV)
H-H	$0.150(\theta_H - 0.100)$
CO-CO	$1.686(\theta_{CO} - 0.092)$
H-CO	$(0.229+2.140\sqrt{\theta_{CO}\theta_H})\,\theta_{CO}$
H-Phenoxy	$(-1.124+16.565\sqrt{\theta_{Phenoxy}\theta_H})\,\theta_{Phenoxy}$
CO-Phenoxy	$(0.851+11.255\sqrt{\theta_{Phenoxy}\theta_{CO}})\,\theta_{Phenoxy}$

Table C.3: Free energies of reaction (in eV) in the limit of zero coverage at 473 K temperature under different reaction environments for phenol hydrogenation over Ru(0001) surface.

ID	Reaction	Vapor phase, ΔG_{rxn}		
		423 K	473 K	523 K
1	Phenol**** + H* ↔ HC1-1**** + *	0.40	0.41	0.41
2	HC1-1**** + H* ↔ HC1-2a**** + *	0.85	0.85	0.85
3	HC1-1**** + H* ↔ HC1-2b**** + *	0.80	0.80	0.80
4	HC1-2a**** + H* ↔ HC1-3a**** + *	0.50	0.50	0.50
5	HC1-2a**** + H* ↔ HC1-3b**** + *	0.57	0.57	0.57
6	HC1-2a**** + H* ↔ HC1-3c**** + *	0.49	0.49	0.49
7	HC1-2a**** + H* ↔ HC1-3d**** + *	0.58	0.58	0.59
8	HC1-2b**** + H* ↔ HC1-3e**** + *	0.63	0.63	0.63
9	HC1-2b**** + H* ↔ HC1-3f**** + *	0.48	0.47	0.46
10	HC1-2b**** + H* ↔ HC1-3g**** + *	0.16	0.16	0.15
11	HC1-2b**** + H* ↔ HC1-3h**** + *	0.64	0.64	0.64
12	HC1-3a**** + H* ↔ HC1-4a**** + *	0.00	-0.01	-0.02
13	HC1-3b**** + H* ↔ HC1-4a**** + *	-0.07	-0.08	-0.08
14	HC1-3c**** + H* ↔ HC1-4b**** + *	0.01	0.01	0.00
15	HC1-3d**** + H* ↔ HC1-4b**** + *	-0.08	-0.09	-0.10
16	HC1-3e**** + H* ↔ HC1-4c**** + *	0.09	0.08	0.08
17	HC1-3f**** + H* ↔ HC1-4c**** + *	0.24	0.25	0.25
18	HC1-3g**** + H* ↔ HC1-4d**** + *	0.40	0.39	0.39
19	HC1-3h**** + H* ↔ HC1-4d**** + *	-0.08	-0.09	-0.10
20	HC1-4a**** + H* ↔ HC1-5a**** + *	0.26	0.26	0.26
21	HC1-4a**** + H* ↔ HC1-5b**** + *	0.67	0.67	0.67
22	HC1-4b**** + H* ↔ HC1-5c**** + *	0.27	0.27	0.27
23	HC1-4b**** + H* ↔ HC1-5d**** + *	0.65	0.64	0.64
24	HC1-4c**** + H* ↔ HC1-5e**** + *	0.44	0.43	0.43
25	HC1-4c**** + H* ↔ HC1-5f**** + *	0.47	0.47	0.47
26	HC1-4d**** + H* ↔ HC1-5g**** + *	0.27	0.27	0.27
27	HC1-4d**** + H* ↔ HC1-5h**** + *	0.64	0.64	0.64
28	HC1-5a**** + H* ↔ HC-6**** + *	-0.16	-0.17	-0.17
29	HC1-5b**** + H* ↔ HC-6**** + *	-0.57	-0.58	-0.59
30	HC1-5c**** + H* ↔ HC-6**** + *	-0.17	-0.18	-0.18
31	HC1-5d**** + H* ↔ HC-6**** + *	-0.55	-0.56	-0.56
32	HC1-5e**** + H* ↔ HC-6**** + *	-0.51	-0.51	-0.51
33	HC1-5f**** + H* ↔ HC-6**** + *	-0.55	-0.55	-0.55
34	HC1-5g**** + H* ↔ HC-6**** + *	-0.17	-0.18	-0.18
35	HC1-5h**** + H* ↔ HC-6**** + *	-0.55	-0.55	-0.56
36	HC-6**** + 2* ↔ KET-6**** + 2H*	-0.50	-0.49	-0.49

37	Phenol**** + H* ↔ HC2-1**** + *	0.58	0.58	0.58
38	HC2-1**** + H* ↔ HC2-2a**** + *	0.62	0.62	0.63
39	HC2-1**** + H* ↔ HC2-2b**** + *	0.78	0.78	0.78
40	HC2-2b**** + H* ↔ HC2-3a**** + *	0.47	0.47	0.48
41	HC2-2b**** + H* ↔ HC2-3b**** + *	0.46	0.46	0.47
42	HC2-2b**** + H* ↔ HC2-3c**** + *	0.57	0.57	0.57
43	HC2-2b**** + H* ↔ HC2-3d**** + *	0.50	0.50	0.50
44	HC2-3a**** + H* ↔ HC2-4a**** + *	0.09	0.09	0.09
45	HC2-3b**** + H* ↔ HC2-4a**** + *	0.10	0.10	0.10
46	HC2-3c**** + H* ↔ HC2-4b**** + *	-0.21	-0.22	-0.22
47	HC2-3d**** + H* ↔ HC2-4b**** + *	-0.14	-0.14	-0.15
48	HC2-4b**** + H* ↔ HC2-5a**** + *	0.30	0.30	0.31
49	HC2-4b**** + H* ↔ HC2-5b**** + *	0.23	0.23	0.24
50	HC2-5a**** + H* ↔ HC-6**** + *	-0.17	-0.18	-0.18
51	HC2-5b**** + H* ↔ HC-6**** + *	-0.10	-0.11	-0.11
52	Phenol**** + H* ↔ HC3-1**** + *	0.51	0.51	0.51
53	HC3-1**** + H* ↔ HC3-2a**** + *	0.72	0.72	0.72
54	HC3-1**** + H* ↔ HC3-2b**** + *	0.74	0.74	0.74
55	HC3-2a**** + H* ↔ HC3-3a**** + *	0.12	0.11	0.11
56	HC3-2a**** + H* ↔ HC3-3b**** + *	0.57	0.57	0.57
57	HC3-2a**** + H* ↔ HC3-3c**** + *	0.52	0.52	0.53
58	HC3-2a**** + H* ↔ HC3-3d**** + *	0.09	0.09	0.09
59	HC3-2b**** + H* ↔ HC3-3e**** + *	0.55	0.55	0.56
60	HC3-2b**** + H* ↔ HC3-3f**** + *	0.59	0.59	0.60
61	HC3-2b**** + H* ↔ HC3-3g**** + *	0.48	0.49	0.49
62	HC3-2b**** + H* ↔ HC3-3h**** + *	0.58	0.58	0.59
63	HC3-3a**** + H* ↔ HC3-4a**** + *	0.39	0.39	0.39
64	HC3-3b**** + H* ↔ HC3-4a**** + *	-0.06	-0.06	-0.07
65	HC3-3c**** + H* ↔ HC3-4b**** + *	0.01	0.00	-0.01
66	HC3-3d**** + H* ↔ HC3-4b**** + *	0.43	0.43	0.43
67	HC3-3e**** + H* ↔ HC3-4c**** + *	-0.07	-0.07	-0.08
68	HC3-3f**** + H* ↔ HC3-4c**** + *	-0.11	-0.11	-0.11
69	HC3-3g**** + H* ↔ HC3-4d**** + *	0.20	0.19	0.19
70	HC3-3h**** + H* ↔ HC3-4d**** + *	0.10	0.10	0.09
71	HC3-4a**** + H* ↔ HC3-5a**** + *	0.22	0.22	0.22
72	HC3-4a**** + H* ↔ HC3-5b**** + *	0.27	0.28	0.28
73	HC3-4d**** + H* ↔ HC3-5c**** + *	0.46	0.46	0.46
74	HC3-4d**** + H* ↔ HC3-5d**** + *	0.43	0.42	0.42
75	HC3-5a**** + H* ↔ HC-6**** + *	-0.11	-0.11	-0.12
76	HC3-5b**** + H* ↔ HC-6**** + *	-0.16	-0.17	-0.18
77	Phenol**** + H* ↔ HC4-1**** + *	0.71	0.71	0.71
78	HC4-1**** + H* ↔ HC4-2a**** + *	0.52	0.52	0.52
79	HC4-1**** + H* ↔ HC4-2b**** + *	0.54	0.55	0.56

80	Phenol**** + * ↔ KET-1**** + H*	-0.77	-0.76	-0.76
81	KET-1**** + H* ↔ KET-2a**** + *	0.99	0.99	0.99
82	KET-2a**** + H* ↔ KET-3a**** + *	0.62	0.62	0.62
83	KET-2a**** + H* ↔ KET-3b**** + *	0.45	0.45	0.45
84	KET-2a**** + H* ↔ KET-3c**** + *	0.31	0.31	0.31
85	KET-2a**** + H* ↔ KET-3d**** + *	0.76	0.76	0.76
86	KET-3a**** + H* ↔ KET-4a**** + *	0.51	0.51	0.51
87	KET-3b**** + H* ↔ KET-4a**** + *	0.68	0.68	0.68
88	KET-3c**** + H* ↔ KET-4b**** + *	0.32	0.32	0.32
89	KET-3d**** + H* ↔ KET-4b**** + *	-0.12	-0.13	-0.13
90	KET-4a**** + H* ↔ KET-5a**** + *	0.45	0.44	0.44
91	KET-4a**** + H* ↔ KET-5b**** + *	0.35	0.35	0.35
92	KET-4b**** + H* ↔ KET-5c**** + *	0.17	0.17	0.16
93	KET-4b**** + H* ↔ KET-5d**** + *	0.81	0.82	0.82
94	KET-5a**** + H* ↔ KET-6**** + *	-0.45	-0.45	-0.45
95	KET-5b**** + H* ↔ KET-6**** + *	-0.35	-0.36	-0.36
96	KET-5c**** + H* ↔ KET-6**** + *	0.31	0.32	0.32
97	KET-5d**** + H* ↔ KET-6**** + *	-0.33	-0.33	-0.34
98	KET-6**** + H* ↔ KET-7a**** + *	0.61	0.60	0.60
99	KET-6**** + H* ↔ KET-7b**** + *	0.36	0.36	0.36
100	KET-7a**** + H* ↔ HC-6**** + *	-0.11	-0.11	-0.12
101	KET-7b**** + H* ↔ HC-6**** + *	0.13	0.13	0.12
102	KET-1**** + H* ↔ KET-2b**** + *	0.94	0.94	0.94
103	KET-2b**** + H* ↔ KET-3e**** + *	0.28	0.28	0.28
104	KET-2b**** + H* ↔ KET-3f**** + *	0.82	0.82	0.82
105	KET-2b**** + H* ↔ KET-3g**** + *	0.27	0.27	0.27
106	KET-2b**** + H* ↔ KET-3h**** + *	0.82	0.82	0.82
107	KET-3e**** + H* ↔ KET-4c**** + *	0.47	0.47	0.46
108	KET-3f**** + H* ↔ KET-4c**** + *	-0.06	-0.07	-0.08
109	KET-3g**** + H* ↔ KET-4d**** + *	0.42	0.42	0.42
110	KET-3h**** + H* ↔ KET-4d**** + *	-0.13	-0.13	-0.14
111	KET-4c**** + H* ↔ KET-5e**** + *	0.10	0.09	0.09
112	KET-4c**** + H* ↔ KET-5f**** + *	0.77	0.77	0.78
113	KET-5e**** + H* ↔ KET-6**** + *	0.33	0.33	0.34
114	KET-5f**** + H* ↔ KET-6**** + *	-0.34	-0.35	-0.35

APPENDIX D:

COPYRIGHT PERMISSIONS

Copyright Clearance Center RightsLink®

Home | Create Account | Help | LIVE CHAT

ACS Publications
Most Trusted. Most Cited. Most Read.

Title: Liquid-Phase Modeling in Heterogeneous Catalysis
Author: Mohammad Saleheen, Andreas Heyden
Publication: ACS Catalysis
Publisher: American Chemical Society
Date: Mar 1, 2018
Copyright © 2018, American Chemical Society

LOGIN

If you're a copyright.com user, you can login to RightsLink using your copyright.com credentials.

Already a RightsLink user or want to learn more?

PERMISSION/LICENSE IS GRANTED FOR YOUR ORDER AT NO CHARGE

This type of permission/license, instead of the standard Terms & Conditions, is sent to you because no fee is being charged for your order. Please note the following:

- Permission is granted for your request in both print and electronic formats, and translations.
- If figures and/or tables were requested, they may be adapted or used in part.
- Please print this page for your records and send a copy of it to your publisher/graduate school.
- Appropriate credit for the requested material should be given as follows: "Reprinted (adapted) with permission from (COMPLETE REFERENCE CITATION). Copyright (YEAR) American Chemical Society." Insert appropriate information in place of the capitalized words.
- One-time permission is granted only for the use specified in your request. No additional uses are granted (such as derivative works or other editions). For any other uses, please submit a new request.